Impact of Breakup Coupling in Nuclear Reactions on Light Elements

Thesis submitted to

University of Calicut in partial fulfilment

for award of the Degree of

Doctor of Philosophy

in

Physics

By

MIDHUN C.V

Reg. No : PHY PHD-5-2018

under the guidance of

Dr. M. M. Musthafa

Professor, Department of Physics

UNIVERSITY OF CALICUT

SEPTEMBER - 2023

DECLARATION

This is to certify that the thesis entitled **'Impact of Breakup Coupling in Nuclear Reactions on Light Elements'** is a bonafide record of research work carried out by me at Department of Physics, University of Calicut, Kerala - India, under the supervision of Prof.(Dr.) M.M. Musthafa. This thesis has not been submitted by me elsewhere for the award of any degree/diploma at this or any other University/ Institution.

Midhun C.V
Department of Physics
University of Calicut
Kerala - 673638

Calicut University

Date: 03.06.2024

UNIVERSITY OF CALICUT

Dr. M.M.MUSTHAFA
Senior Professor & Former Head
Department of Physics
Email: mmm@uoc.ac.in, mm_musthafa@rediffmail.com

Calicut University P.O.
Kerala INDIA 673 63
Ph: 0494-2407415 (O)
09745509190(m)

Ref. No. Res/students 30.03.2024

DECLARATION

This is to certify that the thesis entitled '**Impact of Breakup Coupling in Nuclear Reactions on Light Elements**' submitted to the Department of Physics, University of Calicut, Kerala - India, by **Midhun C.V** in partial fulfillment for the award of the degree of Doctor of Philosophy is a bonafide record of research work carried out by him under my guidance and supervision at the Department of Physics, University of Calicut. The contents of the thesis have been checked for plagiarism using the software 'DrillBit' and the similarity index falls under permissible limit. The suggestions/ comments by the referees after evaluation have been incorporated into the present version of the thesis. This thesis has not been submitted by him elsewhere for the award of any degree/diploma at this or any other University/ Institution.

Prof. (Dr.) M.M Musthafa

Prof.(Dr.) M.M. MUSTHAFA
Senior Professor
Department of Physics
University of Calicut
Kerala-673635, India

DEPARTMENT OF PHYSICS UNIVERSITY OF CALICUT 673635

Dedicated to My Beloved

Parents and Family

Acknowledgements

I would like to seize this moment to convey my heartfelt gratitude to everyone who contributed to the realization of my dream - this thesis.

I express my sincere and wholehearted appreciation to my esteemed research supervisor, **Prof. (Dr). M. M. Musthafa**, Professor, Department of Physics, University of Calicut. His decision to allow me to work under his guidance provided me with a valuable opportunity. His profound understanding, guidance, encouragement, patience, and personal involvement proved invaluable in helping me navigate the uncertainties that emerged during this period. I am greatly indebted to his unwavering perseverance, which enabled me to present this work in the most accurate and meaningful manner.

My sincere gratitude goes out to several individuals who have significantly contributed to my research. I extend my thanks to **Prof. Muhammed Shahin T**, the Head of the Department. I am grateful to **Prof. C.D Ravikumar**, **Prof. A.M Vindokumar**, **Prof. P. P. Pradyumnan** and **Prof. Antony Joseph**, former Heads of the Department for their support and provision of essential facilities. I would also like to express my appreciation to the entire faculty members, as well as the diligent library and office staff of the department.

I wish to express my deep gratitude to my collaborators who have played a crucial role in my research endeavors. My heartfelt thanks go to **Dr. S.V Suryanarayana**, **Dr. P. C Rout**, and **Dr. S Santra** from the Nuclear Physics Division at BARC Mumbai. Their support in planning and the successful

execution of experiments at the BARC-TIFR PLF Facility. Furthermore, I am profoundly thankful to **Dr. S Ganesan**, a Raja Ramanna Fellow of the DAE, BARC-Mumbai. His substantial support and insightful discussions have greatly enriched my understanding of the thesis problem.

Its my pleasure to acknowledge the BARC-TIFR Pelletron Linac Group and Late Mr. Rajendra Kujur for their support in setting up the instrumentation and providing the stable beam.

I would like to express my special thanks to the **DAE-BRNS-INDIA**, for the financial support through **Project Fellowship**.

I am genuinely thankful to my research group members: **Dr. Hajara K**, **Ms. Shaima Akbar**, **Dr. Mohamed Shan**, **Ms. Vafiya T.**, **Ms. Swapna Balakrishnan**, **Mr. Rijin N.T**, and **Mr. Gokul Das**. Their encouragement and meaningful discussions throughout this period have been invaluable. I fondly recall the time spent with fellow research scholars, especially **Dr. Salma Ibrahim**, **Arjun K.**, **Dr. Jisha**, **Rasmi.K. Bharatan**, as well as M.Sc students **Farhana Thesni M.P**, **Arun P.V**, **Gouri V. Raja**, **Meera S. Nair**, **Athira V**, and **Sreena M**. Engaging in both academic and non-academic discussions with them has been an enriching experience.

I am profoundly grateful to my **Father**, **Mother**, **All Family Members**, **Teachers**, and **Friends**. Their unwavering love has provided me with substantial spiritual support in my journey.

Above all, I extend my thanks to **Lord Dakshinamoorthy**, the god of knowledge, for creating the suitable circumstances that have led to this achievement. Finally, I would like to express my appreciation to each and every individual who has been a source of support, encouragement, and guidance, helping me to reach my goal and successfully complete my thesis work.

Midhun C.V

Contents

Preface **xv**

List of Acronyms **xxii**

List of Publications **xxiii**

1 Introduction **1**

1.1 Time line of Developments Nuclear Physics 1

1.2 Evolution of Universe through Nucleosynthesis 4

1.3 Nuclear reactions 6

1.3.1 Breakup Reactions 7

1.3.2 The ^{7}Li(p,n) Reaction 10

1.3.3 Radiative Capture in Li isotopes 12

2 Coupled Channel Formalism for Direct Reactions **20**

2.1 Introduction 20

2.2 Coupled Reaction Channel Formalism 22

2.3 Born Approximation Method 29

2.4 Continuum Discretized Coupled Channel 32

3 Impact of ^{7}Be breakup on ^{7}Li(p,n) Reaction **36**

3.1 Introduction 36

3.2 Materials and Methods 40

3.2.1 Target Preparation 40
3.2.2 Experimental Setup 41
3.3 Data Analysis 44
3.3.1 Event Reconstruction and Data Analysis 44
3.3.2 FRESCO Calculations 48
3.4 Results and Discussion : Events and Double Differential Cross Sections 53
3.4.1 Impact of Couplings in Ejectile Neutron Spectrum 55
3.5 Summary 61

4 Resonant and Breakup Couplings in Direct Capture Reactions 65
4.1 Introduction 65
4.2 Materials and Methods 68
4.2.1 Measurement of ^{6}Li(n,γ) Cross Sections 68
4.2.2 Measurement of ^{7}Li(n,γ) 76
4.3 Theoretical Calculations 79
4.4 Results and Discussion 81
4.4.1 ^{6}Li(n,γ) 81
4.4.2 ^{7}Li(n,γ) 83
4.5 Summary 89

5 Conclusion and Future Outlook 96
5.1 Introduction 96
5.2 The ^{7}Li(p,n) reactions 97
5.3 Impact of breakup coupling in radiative capture 98
5.4 Summary 101
5.5 Future Outlook 102

6 Recommendations 105

List of Figures

1.1 The ^{7}Li(p,n)^{7}Be excitation function from EXFOR-Compiled datasets. 11

1.2 The Experimental ^{7}Li(p,n) neutron spectrums corresponding to 16, 20 and 30 MeVs by McNaughton et al. 12

1.3 ^{7}Li(p,n) neutron spectrum at 20 MeV and GNASH calculations . 13

1.4 ^{6}Li(n,γ) excitation functions by ENDF/B-VIII.0, JEEF-3 evaluations and the measurement by T. Oshaki et al. 14

2.1 The Jacobi Coordinate representation of the breakup fragment interaction with target 33

3.1 The experimental excitation function for ^{7}Li(p,n)^{7}Be reaction with TENDL-2019 evaluations 37

3.2 Experimental Setup 41

3.3 Schematics of the Electronics Setup 42

3.4 $\Delta E - E$ correlation spectra measured by -55° telescope 44

3.5 The ^{3}He-α Coincidences with K_{nn} window based on 3 body kinematics 45

3.6 An example energy correlation plot of the Energy measured in -55° versus energy of resolved ^{3}He in +55°, for the coincidence events, used for reconstruction of αs below the discrimination threshold. Red circle indicates the constant radius (Δ) window about kinematically defined query point 45

3.7 Representation of the coupling of neutron wave function to the ^{3}He - α breakup continuum 48

3.8 Representation of the coupling of neutron wave function to the ^{3}He - α breakup continuum 49

3.9 Representation of the $^3\mathrm{He} - \alpha$ breakup continuum discretized based on the relative angular momentum 51

3.10 Representation of the $^3\mathrm{He} - \alpha$ breakup levels including the resonant states 52

3.11 Representation of the breakup continuum, resonant states and the spectroscopic overlaps 53

3.12 The true coincidence and reconstructed events comparison with three body kinematics, projected to the fragments at +55° and −55° 54

3.13 The measured double differential cross sections for ^{7}Li(p,n)^{7}Be$^* \rightarrow n$+^{3}He+α, and CDCC-CRC calculated continuum and resonant stare cross sections(for the laboratory folding angle of 110°) . . . 54

3.14 Fixed Radius K_{nn} based identification of the neutrons in coincidence with ^{3}He 57

3.15 Neutron Energy - Efficiency plot for EJ301 Liquid Scintillator . . 57

3.16 The simulated 0° breakup neutron spectrum at 21 MeV, having continuum and resonance contributions 58

3.17 The comparison of ^{3}He gated neutron spectra with theoretical spectra 58

3.18 Comparison of evaluated neutron spectrum with the spectrum reported by McNaughton et. al. for 20 MeV 59

4.1 Direct Neutron Capture mechanism in ^{6}Li(n,γ) reaction 67

4.2 Illustration of experimental setup in top and lateral views 71

4.3 The typical $E - \Delta E$ Correlation plot recorded in the telescope . . 72

4.4 The obtained E_γ-E_x correlation 73

4.5 Geant4 simulated response matrix for $LaBr_3$ scintillation detector 74

4.6 The unfolded E_γ-E_x correlation matrix with the gate defined for 12.375 MeV excitation 74

4.7 Projection of the gate defined for 12.375 MeV excitation showing the γ spectrum from the 12.375 MeV initial capture state 75

4.8 Schematic of the Neutron Time of Flight setup 75

4.9 The correlation plot between neutron Time of flight and E_γ recorded in the CZT detector 78

4.10 Resolution Function for current Time of Flight setup 78

4.11 Resonant and Continuum Discretized levels of ^{7}Li 80

4.12 Measured ^{6}Li(n, γ) cross sections compared with Direct Capture Model Calculations in FRESCO, Talys-1.95, and the evaluations by ENDF/B-VIII.0, JEEF-3.3 and JENDL-5 libraries 81

4.13 Measured γ spectrum at 11.5 MeV excitation energy along with the calculated spectrum 82

4.14 Discrete and Continuum components of direct capture and the Hauser-Feshbach- + pre-equilibrium component (HF+Preeq) with the the total cross section compared with the experimental data . 84

4.15 Contribution of E_1, E_2 and M_1 modes of electromagnetic transition to the total capture cross section. 84

4.16 The ^{7}Li$(n,\gamma)^8Li$ cross sections compared with Talys-1.9 Direct Capture Model code predictions with resonances from default Talys library, R-Matrix fitting provided by SAMMY and the ENDF/B-VIII.0 Predictions 86

4.17 The ^{7}Li$(n,\gamma)^8Li$ cross sections compared with potential model calculations 87

4.18 ^{6}Li(n,γ) Excitation function with marking for energies corresponding resonant state of ^{7}Li 89

List of Tables

3.1 Optical Model Potential Parameters for $p +^7$ Li, taken from [18, 19, 20, 21, 22] 49

3.2 Optical Model Potential Parameters for $n+^7$Be, taken from model by Koning & Delaroche 50

3.3 Optical Model Potential Parameters for ^{3}He $+^4$ He, taken from model by Koning & Delaroche 50

3.4 Optical Model Potential Parameters for $n +^4$ He 50

3.5 Optical Model Potential Parameters for $n +^3$ He 50

Preface

Studying behavior of nuclear reaction mechanisms is crucial for understanding properties of the nucleus and behavior of nuclear force between nucleons as well as shedding light on nuclear structure. The journey in nuclear physics commenced with discovery of radioactivity Henry Becquerel in 1896. Rutherford's observation of the first nuclear reaction in 1919 marked the beginning of nuclear reaction history. In these reactions, a projectile nucleus interacts with a target nucleus, emitting particles and leaving a residual nucleus. According to the nuclear reaction systematics, the nuclear reactions can be categorized as Compound Nuclear Reactions, Direct Reactions and Preequilibrium reactions.

Direct nuclear reactions involve the interaction of an incident particle with a target nucleus, resulting in particle emission without the formation of a compound nucleus. The direct reactions predominantly occur at lower incident energies for light elements and higher energies for the targets having mass number above 16. Theoretical aspects of direct reactions involve the use of the distorted wave Born approximation (DWBA) or coupled channel methods to describe the scattering of the incident particle by the target nucleus. In the DWBA, the scattering process is broken down into successive steps: **1:** the interaction between the incident particle and the target nucleus, **2:** the propagation of the outgoing particle wave **3:** the interaction between the outgoing particle and the residual nucleus. This approach takes into account the distortion of the incoming and outgoing waves due to the nuclear potential, which provides a framework to calculate cross-sections and angular distributions.

Coupled channel methods are used when the incident particle-target nucleus

interaction involves multiple degrees of freedom, such as vibrational or rotational excitations in the heavy systems and couplings like spin transfer, single particle excitation, electromagnetic, charge exchange etc, in the light systems. These methods consider the coupling between different channels to accurately describe the scattering process and the resulting particle emission. The direct reactions are vital for studying the nuclear structure of both the projectile and the target, as well as for determining reaction mechanisms. They are particularly important for understanding the properties of exotic nuclei and astrophysical processes.

Direct capture nuclear reactions occur at low energies, often encountered in nuclear astrophysics scenarios. These reactions entail the capture of an incident particle, typically a neutron or a proton, by a target nucleus. This capture process leads to the creation of a compound nucleus. Unlike compound reactions that undergo excitation and equilibration, direct capture reactions immediately establish a bound state within the compound nucleus. These reactions are important for understanding nucleosynthesis in stars and also for studying nuclear structure. One intriguing aspect of direct capture reactions is the formation of resonances. Resonances are specific energy levels in the compound nucleus that enhance the probability of capture at particular incident energies. These resonances arise due to the quantum-mechanical interference between the incoming wave and the wave reflected off the potential barrier of the nucleus.The energy at which a resonant state occurs is determined by the energy spacing of the discrete levels in the compound nucleus. When the incident particle energy matches the energy of a resonance state, the probability of capture is greatly enhanced, resulting in a sharp peak in the cross-section. Resonance energies and strengths provide valuable information about the excited states and level structure of the compound nucleus. Direct capture reactions and the formation of resonances are studied experimentally through measurements of cross-sections as a function of incident particle energy. The Breit-Wigner formula is often used to describe resonance cross-sections mathematically, allowing us to extract resonance parameters like energy, width, and spin.

The present elemental abundance in the universe is produced through the big-bang and stellar nucleosynthesis, driven by diffrent nuclear reactions. Tracking the evolution stages of the universe and aging of the stars are mainly performed by the back calculation with the nuclear reactions. Among the elemental abundances in the universe, the light elements are being produced through big bang nucleosynthesis process, and they are more or less reproduced using the nuclear reaction rate calculations. However the big bang nucleosynthesis exhibits a significant level of depression in the observed value than the theoretically predicted value for the formation of Li,Be and B elements, and renowned as cosmological lithium-beryllium-boron problem.

The cosmological lithium-beryllium-boron problem in nuclear astrophysics refers to the puzzling discrepancies between the predicted and observed abundances of light elements such as lithium beryllium and boron in the universe. These elements are believed to have been formed in the early stages of the universe and are crucial for understanding the processes of primordial nucleosynthesis and the evolution of cosmic structures.

The predicted abundances of ^{7}Li based on the theory of Big Bang nucleosynthesis are higher than the observed abundances in some metal-poor stars and quasar absorption systems. This discrepancy suggests the possibility of missing or poorly understood physical processes that affected the production or destruction of ^{7}Li shortly after the Big Bang

The abundance of Be and B also present challenges. These elements are thought to be produced through interactions of cosmic rays with background particles, such as hydrogen and helium, over cosmic timescales. However, the observed abundances of ^{9}Be and ^{11}B in some astrophysical environments, such as halo stars, are significantly lower than the predictions based on the expected cosmic ray interactions. This could indicate complex interactions between cosmic rays and the interstellar medium that are not fully understood.

Deeper comprehension of nuclear reactions, cosmic ray interactions, and astrophysical processes in both the early universe and later cosmic epochs be-

comes imperative for resolving these cosmological lithium-beryllium-boron problems. This effort involves refining nucleosynthesis models, investigating the consequences of stellar mixing and other astrophysical conditions, and delving into potential new physics that transcends our current understanding. Understanding the production and destruction mechanisms of lithium, beryllium, and boron isotopes underpins the solution to these challenges. Direct capture reactions and charge exchange channels play a role in the production channel, while additional isotopic destruction involves residual breakup, inelastic, and transfer-induced reactions. Resonance couplings enhance reaction rates, but the overlap of residual breakup states further contributes to isotopic destruction. Isotopes such as ^{6}Li, ^{7}Li, ^{7}Be, ^{8}B, and ^{9}B in the big bang nucleosynthesis network exhibit resonant or breakup coupling. Analyzing the impact of these resonant and breakup couplings in light element nuclear reactions is vital for interpreting the underlying physics.

In the present thesis, particular emphasis have been placed on examining residue breakup couplings in specific reactions. For example, the charge exchange reaction ^{7}Li(p,n) has undergone intense experimental scrutiny, revealing intricate details of this process. Additionally, direct capture reactions involving ^{6}Li(n,γ) have been meticulously explored. These experimental measurements have been complemented by theoretical calculations utilizing the Continuum Discretized Coupled-Channels (CDCC) approach, in conjunction with the Coupled-Reaction-Channels (CRC) framework.

The continuum neutron spectra resulting from the ^{7}Li(p,n) reaction have been estimated by measuring the double differential cross sections for both continuum and resonant breakup of ^{7}Be through the ^{7}Li(p,n)^{7}Be* reaction at an incident proton energy of 21 MeV. The experiment has been performed at BARC-TIFR Pelletron Linac Facility. A 21 MeV proton beam has been fired on 20μg/cm^{2} Li target, sandwitched between 5μg/cm^{2} carbon and Al. The ^{3}He and α fragments from the breakup of ^{7}Be has been detected in coincidence using E-ΔE telescopes configured at $\pm 55°$s. The precise identification and localization of these events

have been facilitated by advanced machine learning algorithms, notably the K_{nn} algorithm. The excitatin energy of ^{7}Be has been reconstructed from the fragment energies based on the two body kinematics. The contributions from both the continuum and the specific $5/2^-$ and $7/2^-$ states of ^{7}Be to the breakup process has been distinguished. FRESCO CDCC-CRC calculations were performed to replicate the experimental cross sections.

The analysis of the ^{7}Li(p,n) reaction unveiled the formation of continuum neutron distributions, shedding light on the intricate processes at play. These continuum neutron distributions have been attributed to the coupling of the ^{7}Be $\rightarrow$ ^{3}He+α breakup levels with the final state of the reaction. This coupling mechanism, known as spin transfer coupling, facilitates the interaction of the neutron wave function with the ^{7}Be nucleus as it progresses toward the exit channel. This coupling mechanism plays a pivotal role in shaping the continuum neutron spectra generated by the ^{7}Li(p,n) reaction. These theoretical calculations have been validated through experimental measurements, particularly by comparing the results with the experimentally measured ^{3}He gated neutron spectra. Furthermore, The ^{7}Li(p,n) neutron spectrum at 20 MeV incident proton energy have been reproduced, originally measured by McNaughton et al., by adapting estimated model parameters for the reaction estimated by analyzing double differential cross sections for 3 body breakup.

To investigate the impact of breakup coupling on radiative captures in ^{6}Li(n,γ) reactions, a new experimental method based on the Direct Capture (DC) formalism have been implemented. This method allows to measure the ^{6}Li(n,γ)^{7}Li cross sections in the neutron energy range of 0.6 to 4 MeV. Through this method, the electromagnetic transition probabilities from ^{7}Li* are measured, by populating the J_i states analogous to the initial neutron capture states of ^{6}Li+n, through the ^{7}Li$(n,n')^7$Li* reaction. The experiment has been performed at BARC-TIFR pelletron linac facility by firing 21 MeV protons on a 1.5μg/cm^2 target. The inelasically scattered protons were detectected using silicon E-ΔE telecopes at $\pm$55°s. Emited γs were detected using a large $LaBr_3$ Scintillator

in coincidence with inelastically scattered protons. The γ branching has been measured experimentally and spin factor clculated from systematics. These measured cross sections were then reproduced through FRESCO and Talys-1.95 Direct Capture Calculations. Through this analysis, the impact of coupling of resonant states above the $\alpha + t$ breakup threshold of ^{7}Li in the neutron capture of ^{6}Li in the capture γ spectrum have been observed, and the same was reproduced using FRESCO calculations.

The analysis has been extended to measure ^{7}Li(n,γ)^{8}Li reaction cross sections in the neutron energy range of 10 keV to 1 MeV, employing time-of-flight tagged neutrons generated from an Am-Be source. This measurement identified both the non-resonant and 3^+ resonant contributions to the excitation function. We reproduced the non-resonant continuum and resonant component using FRESCO Direct Capture calculations, while the 3^+ resonant state was replicated through electromagnetic coupling and $n +^7$ Li overlap, based on spectroscopy factors for 1p shells.

To gain deeper insights into the influence of breakup coupling, the ^{6}Li(n,γ) and ^{7}Li(n,γ) reaction excitation functions were compared. Notably, the ^{7}Li(n,γ) reaction avoids residual breakup modes in the exit channel, allowing us to probe the effects of breakup coupling. This comparison unveiled a noteworthy observation: instead of the typical resonant enhancement, breakup coupling generated a distinctive resonant dip within the excitation function. To explore this further, the prompt γ spectrum resulting from ^{6}Li(n,γ) was replicated using FRESCO CDCC-CRC calculations followed by electromagnetic transition calculations. This demonstrated electromagnetic coupling from the entrance channel to the unbound resonant states $7/2^-, 5/2^-$, and $3/2^-$. However, we observed no branching from the unbound states to the bound states. From this, it has been concluded that the population of unbound resonant states leads to breakup rather than radiative capture.

This investigation unveiled that electromagnetic coupling, originating from entrance channel scattering states to exit channel scattering states, plays a cru-

cial role in populating the resonant states within the exit channel, regardless of whether these states are bound or unbound. Furthermore, we noted that unbound resonant states evolve into breakup states through a process known as spin transfer coupling. In summary, our findings confirm that residual breakups manifest in a sequential manner and are primarily formed through the mechanisms of spin transfer coupling.

The overall contents of the thesis are summarized as follows.

- **Chapter 1**, provides a basic introduction to the thesis problem by addressing the literature review and relevance of the study
- **Chapter 2** deals with the detailed description of Coupled Channel Formalism for Direct Nuclear Reactions.
- **Chapter 3**, provides the details of measurement of the three body breakup reaction, ^{7}Li(p,n)$\rightarrow n +^{3}$ He $+ \alpha$ and the CDCC-CRC analysis.
- **Chapter 4**, provides the details of measurement and analysis of the excitation functions for ^{6}Li(n,γ) and ^{7}Li(n,γ), and discusses about the impact of breakup coupling to the resonant states of residue.
- **Chapter 5** summarizes the findings of the thesis and discussion on the future prospects of this work.

List of Acronyms:

DWBA	Distorted Wave Born Approximation
CRC	Coupled Reaction Channel
CDCC	Continuum Discretized Coupled Channel
ADC	Analog to Digital Converter
PSD	Pulse Shape Discrimination
TDC	Time to Digital Converter
TOF	Time of Flight
CFD	Constant Fraction Discriminator
CI	Current Integrator
FC	Faraday Cup
DAQ	Data Acquisition System
NRV	Nuclear Reaction Video Project
$\mathbf{K}_{nn}$	Nearest Neighborhood Clustering
DC	Direct Capture

List of Publications

1. C.V Midhun, M.M. Musthafa, S.V. Suryanarayana et al., Impact of ^{7}Be Breakup on ^{7}Li(p,n) neutron spectrum, Physical Review C. 104 (2021). doi:10.1103/physrevc.104.054606.

2. C. V. Midhun, M. M. Musthafa, Shaima Akbar, Swapna Lilly Cyriac, S. Sajeev, Antony Joseph, K. C. Jagadeesan, S. V. Suryanarayana & S. Ganesan (2020) Spectroscopy of High-Intensity Bremsstrahlung Using Compton Recoiled Electrons, Nuclear Science and Engineering, 194:3, 207-212, DOI: 10.1080/00295639.2019.1681210

3. C.V Midhun, M.M. Musthafa, S.V. Suryanarayana et al., An Indirect Measurement of ^{6}Li(n,γ) Cross Sections, arXiv:2209.12165v1, https://doi.org/10.48550/arXiv.2209.12165. Communicated to Phys Rev. C, Under Review

4. C.V Midhun, M.M Musthafa, Shaima A. et al. ^{7}Li(n,γ)^{8}Li Cross Sections Using ToF Tagged Neutrons, Communicated to EPJ Plus, EPJA-107430., Under Review

Publications Co-authored

1. K. Hajara, M. M. Musthafa, C. V. Midhun et al.,Evaporation residue cross section measurements for the 30 Si+176 Yb reaction. Physical Review C. 105, 044619 (2022). https://doi.org/10.1103/PhysRevC.105.04

2. P.V. Arun, C.V Midhun, M.M. Musthafa, A. Silpa, Joseph Naiby, M. Sreena, M.P. Thesni Farhana, E.S. Keerthi, M.V. Deepthi, Joseph Antony,Spectroscopic analysis of photoneutrons in intense γ-ray background,Applied Radiation and Isotopes, 200.110944(2023), https://doi.org/10.1016/j.apradiso.2023.

3. T. T. Vafiya Thaslim, M. M. Musthafa, C.V Midhun, S. Ghugre, H. Gokul Das, B. Swapna,T. Najmunnisa, N. T. Rijin, S. Dasgupta and J. Datta, The total neutron production from the alpha induced reaction on natural zirconium, Eur. Phys. J. A (2023)59: 167,https://doi.org/10.1140/epja/s10050-023-01086-5

4. T. Najumunnisa, M.M. Musthafa, C. V. Midhun et al. 105Rh yield from the proton induced fission of uranium, Nucl. Phys. A. 1032.122611(2023) https://doi.org/10.1016/j.nuclphysa.2023.122611.

5. K. Hajara, M.M. Musthafa, S.R. Abhilash, C.V Midhun, D. Kabiraj,Development of ^{187}Re targets for heavy ion induced reactions, Applied Radiation and Isotopes, 190(2022)110467 DOI:https://doi.org/10.1016/j.apradiso.2022.110467.

6. Pachuau, R., Otuka, N., Midhun, C.V. et al. Fast-neutron induced reaction cross section measurement of tin with dual monitor foils and covariance analysis. Eur. Phys. J. A 57, 268(2021). https://doi.org/10.1140/epja/s10050-021-00578-6

7. Imran Pasha, Rudraswamy Basavanna, Santhi Sheela Yerranguntla, Saraswatula Venkata Suryanarayana, Rebecca Pachuau, Cherumukku Vallabhan Midhun, Haladhara Naik, Tarun Patel, Saroj Bishnoi & Laxman Singh Danu, Measurement of 14.54±0.24 MeV neutron activation reaction

cross sections of 93Nb, natMo with covariance analysis. J Radioanal Nucl Chem 325, 863-868 (2020). https://doi.org/10.1007/s10967-020-07261-y

8. R Vysakh, M M Musthafa, C V Midhun, P Niyas, P T Anjana, M P Arun Krishnan, C P Ranjith, M P Irfad and R Ganapathi Raman, Experimental determination of thermal neutron fluence around Elekta Versa HD linear accelerator for various photon energies, Biomed. Phys. Eng. Express 6 055018 (2020)

9. Cyriac, S.L., Bindhu, B., Midhun, C.V. et al. Effects of Epithermal Neutron Irradiation on the Characteristics of the Porous Silicon. Silicon (2022). https://doi.org/10.1007/s12633-021-01550-1

10. Cyriac, S.L., Bindhu, B., Midhun, C.V. et al. Emerging Trends in Nano Structured Silicon Detectors for Neutron Spectroscopy. Silicon 14, 1331-1337 (2022). https://doi.org/10.1007/s12633-021-00961-4

11. K.R Rajesh, M.M Musthafa, C.V Midhun, Ganapathi Raman, N. Joseph, A passive method for absolute dose evaluation of photoneutrons in radiotherapy, International Journal of Radiation Research, 18.1 (2020)

Conference Proceedings

1. C.V Midhun, M. M. Musthafa, S. V. Suryanarayana, H. Gokul Das, A. Shaima, K. Hajara, Joseph Antony, T. Santhosh, A. Baishya, A. Pal, P. C. Rout, S. Santra, P. T. M. Shan, B. V. John, K. C. Jagadeesan, S. Ganesan, On the estimation of ^{6}Li(n,γ) cross sections, 65th DAE-BRNS Symposium on nuclear physics B29, 401-402 (2022)

2. C.V Midhun, H. Gokul Das, P. V. Arun, N. T. Rijin, S. Shyamprasad, Christopher Varghese, M. Ramjith, V. Gouri, S. Meera, V. Athira, K. S.

Akshay, M. M. Musthafa A Hybrid ECR ion source for low energy applications, 65th DAE BRNS Symposium on nuclear physics G42,1158-1159 (2022)

3. Midhun C.V, M.M Musthafa, Gokul Das H.,Antony Joseph and S.V. Suryanarayana, Jagadeesan, K. C. and S. Ganesan, Measurement of 7 Li(n,γ) using AmBe neutron Time of Flight.64th DAE BRNS Symposium on nuclear physics (2021)

4. C.V Midhun, M.M Musthafa, Shaima Akbar, S.V Suryanarayana, K.C Jagadeesan, N.T Rijin, Monitor Controlled Single Projection Approach for Cross Section Unfolding, Proc. 63th DAE BRNS Symp. Nucl. Phys., (2019) pp 910-911

5. Midhun C.V,M.M Mushtafa,Antony Joseph,Jagadeesan K.C,S Ganesan,Extraction of Neutron Pulses from Coincidence Summed Events via Machine Learning - Like Algorithm,62rd International DAE BRNS Symposium on nuclear physics (2018), pp.1134-1135

6. V. Athira, V. Gouri, S. Meera, Midhun C.V, M. M. Musthafa, P. V. Arun, H. Gokul Das, N.T. Rijin, S. V. Suryanarayana, Discrimination of low energy neutrons with time differentiated signals, Proc. 65th DAE BRNS Symp. Nucl. Phys., G25, 1124-1125(2022)

7. S. Meera, V. Gouri, V. Athira, Midhun C.V, M. M. Musthafa, H. Gokul Das, N. T. Rijin, V. P. Jyothilakshmi, Identification of low energy charged particle with LiF-Si hybrid detectorsProc. 65th DAE BRNS Symp. Nucl. Phys.,G24, 1122-1123 (2022)

8. Gouri V., Athira V., Meera S., Midhun C.V et al., Validation of 7Li(p,n) Neutron Spectrum by Spectral Unfolding, Proc. 65th DAE BRNS Symp.

Nucl. Phys.,B145, 633-634 (2022)

9. Farhana Thesni. M. P, Midhun C.V, M. M. Musthafa, Arun P. V., Rijin N. T., S. V. Suryanarayana, Impact of nuclear reactions on proton therapy dose distribution, 65th DAE BRNS Symp. Nucl. Phys.,B145, 715-716 (2022)

10. Shaima Akbar, Jyoti Pandey, M.M Musthafa, Midhun C.V, Bhawna Pandey, S.V Suryanarayana, B.K Nayak, H.M Agrawal, S Santra, Determination of excitation function of 61Ni(n,xp) reaction using surrogate reaction method, 64th DAE BRNS Symposium on nuclear physics (2019) pp 337-338

11. A. T. Fathima Shirin Shana, M. M. Musthafa, A. K. Abdul, Gafoor, C. V. Midhun, Divya Arora, N. Saneesh, K. S. Golda, P. Sugathan, S. Ganesan, Gamma gated neutron spectrum from Am-Be source, 64th DAE BRNS Symposium on nuclear physics (2019) pp 427-428

12. Gokul Das, C V Midhun, Fathima Shalu, M. M. Musthafa, Production and Transport of Low Emittance Proton Beam,64th DAE BRNS Symposium on nuclear physics (2019), pp.910-911

13. Fathima Shirin Shana A.T.,Midhun C.V,M.M. Musthafa,Ganesan S., ANALYSIS OF NEUTRON ENERGY SPECTRUM FROM 241 Am-Be SOURCE, 63rd International DAE BRNS Symposium on nuclear physics (2018), pp.636-637

Chapter 1

Introduction

1.1 Time line of Developments Nuclear Physics

The investigation and exploration of the origin of the universe have been pursued since the existence of mankind. Early explanations were based on the four-element theory from ancient Greece and the five-element theory from ancient India. In the 6th to 4th century BC, scholars from the Vaisheshika school of Indian philosophy (later renowned as Kannadas) proposed the concept of the atom, which was also proposed by Greek philosophers around the same time. Atomism was scientifically validated by John Dalton in the 18th century, raising questions about the internal structure of atoms.

The discovery of electrons by J.J. Thomson in the cathode ray tube experiment revealed the internal composition of the atom, leading to the search for positively charged particles inside the atom[1]. The alpha scattering experiment by Geiger and Marsden on gold foil, along with Rutherford's theoretical explanation, confirmed the existence of a positively charged atomic center and led to the discovery of the nuclear force. [2, 3]

The Geiger–Nuttall law for alpha decay [4] provided an empirical relation between the half-life of alpha-emitting nuclides and the energy of the outgoing alpha particles. George Gamow later validated this relation through quantum mechanics, revealing the existence of a Coulomb barrier at the nucleus boundary

[5]. Heisenberg proposed a new model for the nucleus with protons and neutrons as constituents.

The demand for high-energy particles to study nuclear properties led to the development of Electrostatic, RF linear accelerators and cyclotrons [6]. Quantum mechanics provided theoretical support in explaining scattering cross-sections, and this led to experiments for analyzing nuclear interaction potentials using high-energy particles. As projectile energy increased, new reaction channels like (p,n), (p,α), (α,n), and (α,p) were observed, mainly through the production of radioactive reaction residue. The discovery of neutrons by James Chadwick in 1935 led to the study of neutron-induced reactions and radiative neutron capture reactions. Nuclear fission was discovered in 1938 and spontaneous fission in 1941.

Theoretical frameworks for nuclear reactions were developed, including George Gamow's quantum mechanical treatment of α decay and Bohr's compound nuclear hypothesis[7], experimentally verified by S.N. Ghoshal in 1950 [8]. Niels Bohr and John Archibald Wheeler improved the theory of nuclear fission mechanism[9]. However, for certain systems and energies, different reaction systematics were observed that could not be explained with compound nuclear approaches. These were identified as direct reactions impacting single nuclear levels. Direct reactions were observed in systems with fewer excitation levels, such as light elements or elements with shell closures. Nuclear structures were analyzed through various calculations, such as Hartree-Fock-Bogoliubov (HFB) calculations and shell model calculations. Compound nuclear reaction models were improved by accounting for proper level density models based on experimental results and phenomenological model calculations. The experimental excitation function, particle spectrum, double differential cross sections, and other data collectively provide insights into the precise physics of the system under specific conditions. This understanding is rooted in a theoretical framework that relies on the concept of an interaction picture. Given that this theory faithfully replicates the experimental results, it validates the theoretical assumptions about the underlying mechanisms representing the true physics. Therefore, to

delve further into the genuine physics of the system, more high quality experimental results are essential.

Other than the academic interest, nuclear physics is widely used in the allied fields such as energy applications, radiotherapy, material testing and characterization, radioisotope production etc [10]. These fields uses nuclear physics as a powerful tool for their specific needs. These fields are widely utilizing the nuclear reaction parameters, called the nuclear data, for the design and measurement process of the corresponding filed.

The applied nuclear programs are potentially using nuclear data sets for the design and safe operation of the reactors and other critical systems. This requires nuclear data as a continuous function. However, the experimental data are limited to a particular energy range, and having point values. Hence, based on the rigorous analysis, the theoretical predictions made fitted to the experimental data sets, with the help of statistical tools for accounting the uncertainties, and continuous lines of excitation functions have been made. This procedure is called nuclear data evaluations and which results the evaluated nuclear data sets. ENDF/B, JENDL, ROSFOUND etc are the typical examples of evaluated nuclear data libraries.

Among the applied nuclear program, the nuclear energy program is one of the most highlighted one. The research on the operation and safety of the nuclear energy systems require evaluated nuclear data sets, with a primary importance to the neutron induced reaction data, ranges from thermal to fast neutron energies. As the fission reactors are considered, the primary power production and criticality calculations are performed through the neutron induced fission data, which having cross sections, product yields, prompt fission neutron spectrum etc. Further, the fast neutron induced data on gas forming reactions are required, for the design of the structure and optimization of the reactor life time[10].

In the non-energy applications, the medical physics is taking direct benefit of nuclear physics. This domain covers isotope production in high purity and specific activity, radiation dosimetry etc. The isotope production requires the

reaction parameters to be well optimized to populate the residue of interest and other isotopes of same elements to a minimum[11]. This optimization require the strong support of the nuclear data physics. On other hand, the radiotherapy is using high intensity photons, protons and heavy ions for the treatment of cancer[12]. The energy deposition by these beams are primarily through the Coulomb effect. However, these beams are initiating significant amount of nuclear reactions, due to its higher energy[13]. There the most contribution of these is from the pre-equilibrium and direct reaction domain, where the residual breakups are significantly affecting on the reaction systematics. This demands evaluated nuclear reaction reaction data, in the form of double differential cross sections to estimate the nuclear reaction contributions.

1.2 Evolution of Universe through Nucleosynthesis

The explanation for origin elements and their abundances in the universe is a primary problem to explain the evolution of the universe. The synthesis of elements in the universe has been taken place through the nuclear reactions initiated after the big bang and in the stellar processes. In the first phase of the elemental synthesis, the protons in the hot plasma interacting together with the weak force produces deuteron. There, a part of the produced deuterons are getting destructed by the high energy photon environment. An equilibrium between production and destruction reaction will be achieved. The proton and photon spectrum available for these reactions are then considered as a function of the plasma temperature. These deuteron nuclei produced are also gaining a velocity corresponding to the plasma temperature and they also initiate nuclear reactions such as ^{2}H(d,n)^{3}He and ^{2}H(d,p)^{3}H. As a result of ^{2}H(d,n)^{3}He reaction, a neutron environment will be added along with the proton and photon environment. Further these neutrons also involve in the nucleosynthesis for producing higher elements. However this big bang phase of the nucleosynthesis ends at the ^{7}Be, as the ^{8}Be produced is not stable, which is immediately dissociates into 2 α particles.

However the ^{12}C is formed in this phase by fusing 3 αs together, corresponding to the 7.65 MeV (0^+) state. From this state, there is a well defined, however weak internal transition probability, in the form of $0^+ \rightarrow 2^+(4.44\text{MeV}) \rightarrow 0^+(ground)$ makes the production of the Carbon in the universe. The further elements beyond ^{12}C are produced through the continuous fusion network. However the fusion chain will be stopped at Iron group, as beyond this the fusion Q values are -ve. Hence the other processes like r, p, s, νp, i etc are producing the further elements in the table of isotopes.

The elemental abundances in the universe are experimentally observed through xray spectroscopy of stars, AMS results of comets etc. Nucleosynthesis network calculations were done to match elemental abundances and confirm the expected nucleosynthesis network. This was achieved by using nuclear reaction cross sections as input, converting them into Maxwellian averages based on the available particle spectrum for each nucleosynthesis process. However, when applied to the Big Bang nucleosynthesis (BBN), which involves fewer networks, the theoretical calculations resulted in an overestimation of the abundances of Li, Be, and B elements compared to what was observed. This issue renowned as Cosmological Lithium Problem, Cosmological Beryllium Problem and Cosmological Boron Problem. This is widely accepted due to the prominence of the destruction reactions, as the breakup thresholds for these isotopes are very low. Hence a global campaign is ongoing to study the destruction of these isotopes.

Among the destruction reactions, ^{6}Li(n,γ) and ^{7}Li(n,γ) is playing an important role in the fag end of the Big Bang Nucleosynthesis for the destruction of the Li isotopes. The ^{6}Li(n,γ) transmuting the ^{6}Li to the ^{7}Li and ^{7}Li(n,γ) is further transmuting the ^{7}Li to ^{8}Li. The produced ^{8}Li will be destructed by the β^- delayed α emission (the β^- decay of ^{8}Li populates ^{8}Be either in ground or resonant states which will be destructed by the breakup modes of ^{8}Be). Other than these the $p+^6$Li, $p+^7$Li etc are also producing sequential breakups such as $p+^6\text{Li} \rightarrow^7 \text{Be}^* \rightarrow^3 \text{He}+\alpha$ and as $p+^7\text{Li} \rightarrow^8 \text{Be}^* \rightarrow \alpha+\alpha$. These destruction reactions are prominent due to the overlapping of breakups in the reaction residue

states, or can be called as the residue breakup modes. This implies the role of breakup reactions in BBN Network calculations. However, due to the limited data availability, these reactions are not producing the satisfactory results in the BBN Network calculations.

1.3 Nuclear reactions

The nuclear reaction systematics can be described as a projectile nuclei approaches the target nuclei, it generates an initial capture state by the nuclear interaction between the projectile and target. From this state, the projectile separates, leading to elastic scattering. Initial capture states that do not decay into the initial projectile-target combination result in the formation of a final unbound state with an ejectile-residue combination and a relative energy of $E_{rel} + Q_{fus}$. The reaction formalism considers that the undecayed flux in the entrance channel couples to the exit channel. Additionally, inelastic channels produced through excitation of the target or residue in the exit channel, as well as the projectile or target in the exit channel, also contribute to the reaction systematics. Excited states can coexist with the same energy, referred to as spectroscopic overlaps. Both coupling and overlaps alter the final state wave function, impacting the reaction cross sections.

During inelastic coupling, the relative energy of the initial capture state excites the projectile or target, reducing their separation in the Jacobi coordinate system and making the state more bounded. This process can lead to the complete absorption of the projectile by the target, forming an intermediate nucleus known as the compound nucleus. As the system progresses towards the compound nucleus from the initial capture state, the total nucleons (in the projectile and target) select a shell model potential, resulting in a level scheme. The energy of the compound nucleus is represented as $E_{rel} + Q_{fus}$, with Q_{fus} as the fusion Q-value for the specific target-projectile combination. For positive fusion Q-values, the nucleons occupy higher energy levels due to their energy being above the ground state. This energy region contains overlapping, degenerate levels,

leading to a statistical emission-absorption process lasting up to approximately 10^{-16} seconds.

In cases with few overlapping levels, the nucleon can be separated from the present state within approximately 10^{-21} seconds, known as the direct reaction. In the direct reaction, either the same projectile or a different particle can be ejected, limited to a few levels only. During ejectile emission, a final unbound state, similar to the initial capture state, forms in the exit channel, with a relative energy of $E_{in} - Q_r$, where Q_r is the reaction Q-value. The ejectile and residue are then separated from this unbound state through a process equivalent to elastic scattering. The potential for the unbound state formation is the scattering potential for the ejectile-residue combination.

Depending upon the states of the residue produced in the nuclear reactions, the ejectile wavefunction will be modified by the coupling of these states. Generally the pion exchange, spin transfer, electromagnetic couplings and single particle excitation couplings and other zero-range and local energy approximated potential couplings are being considered. These couplings are generally between the states in the entrance channel to the exit channel. Other than the resonant states, the continuum states produced by the breakup of the target or residue can also induce couplings in nuclear reaction. This is considered as a continuum coupling and require continuum discretized coupled channel (CDCC) methods to employ this.

1.3.1 Breakup Reactions

Breakup nuclear reactions, are also known as nuclear disintegration reactions. This refer to the process in which a projectile interacts with a target nucleus resulting in the breakup or disintegration of the target nucleus into several fragments. These reactions play a crucial role in understanding the dynamics of nuclear reactions and have significant implications in fields such as nuclear physics, astrophysics, and radiotherapy. When considering breakup reactions on light elements, typically proton and α projectiles interacting with light target nuclei

such as ^{3}He, ^{6,7}Li, ^{9}Be, ^{12}C etc., several important aspects come into play.

The breakup reactions, $C \rightarrow a + b$ is generally observed in the light elements, as the C is exited with an energy beyond the a+b breakup threshold, the C will be disintegrated to $a + b$. The first human controlled nuclear reaction $^{7}Li(p, \alpha)^{4}He$, performed by H. J Cockroft and W. S Walton, was a breakup reaction. There the protons fired on ^{7}Li produces ^{8}Be, in unbounded state. The unbounded ^{8}Be is further disintegrated into 2 α particles. The breakup phenomena in the direct reaction is mainly exhibited in two modes, are direct breakup and sequential breakup. In the direct breakup, the breakup fragments are disintegrated from the ground state of the final state for the nuclear reaction. In the sequential breakup, also renowned as the resonant breakup, the fragments are disintegrated from the resonant states of the final residue, which having a Q-value higher than the direct breakup reactions.

The breakup fragments produce a relative motion between them before it is being disintegrated. This relative motion produces additional excitation energy states than the resonant states having excitation energy equal to the relative energy of the fragments and spin corresponding to the angular momentum between the fragments and the spin of the individual fragments. The concept of the relative energy and the breakup systematics has been introduced and explained by R. J de Meijer and R. Kamermans [14]. There the reconstructed relative energy of the fragments has been used as a tool for observing the breakup states. The relative energy has been measured by obtaining energy and angle of the breakup fragments disintegrated from a state, by making a coincidence detection. By establishing relative energy as a tool, the direct and resonant contributions has been experimentally resolved. Further, the Distorted Wave Born Approximation method has been used to reproduce differential and double differential cross sections for the breakup reactions [15].

D. Chattopadhyay et al. measured the direct and resonant breakup of ^{8}Be and ^{7}Be nuclei, populated through proton pickup reactions by ^{7}Li and ^{6}Li projectiles [16, 17]. The contributions from direct and resonant states of ^{8}Be and

^{7}Be has been identified by establishing Relative energy verses Q-value correlation corresponding to the events. The relative motion of breakup fragments producing a continuum having wide range of excitation states with a range of angular momentum and spin. Hence a direct DWBA calculation is complex to fairly reproduce the breakup angular distribution. Hence a continuum discretized coupled channel (CDCC) approach has been used by I. J Thomson et al [18] and introduced in FRESCO code for direct reactions. K Rusek et al. has been reproduced the experimental double differential cross section for the elastic scattering of ^{6}Li on ^{4}He using the CDCC approach, by binning the continuum states into discrete states based on the momentum [19]. This is required as the $^6\text{Li} \rightarrow \alpha + d$ breakup couples to the elastic scattering and $\alpha + d$ breakup produces the continuum states. In a similar approach N. C. Summers and F. M. Nunes has explained the breakup of ^{7}Be with CDCC approach [20]. Similarly A. Pakou et al. has also explained the breakup of $^7\text{Li} \rightarrow \alpha + t$ using the CDCC approach [21].

However, the reactions are exhibiting resonant (sequential) breakups along with the direct breakups. These resonant states are being populated by the coupling of the resonant states to the initial state. However due to the overlap of the breakup continuum on the resonant states, those states are being disintegrated through the breakup mode. D. Chattopadhyay et al. has been utilized the coupled reaction channel (CRC) to reproduce the breakup contributions from these resonant state. This is established by introducing coupling to the CRC states those are overlapped by the breakup continuum. Through these approach, the direct and resonant breakup from ^7Be and ^{8}Be has been well reproduced. This shows the CDCC-CRC method is the most appropriate approach of accounting the breakup couplings. However the number of works in the current ages are limited to a few only due to the complexity involved in the breakup reaction experiments and calculations.

1.3.2 The ^{7}Li(p,n) Reaction

The ^{7}Li(p,n) is the popular reaction producing quasi-monoenergetic neutrons for nuclear data measurements in the fast neutron region due to its tunability and higher neutron yield. This also having a potential importance in the enhancement of neutron flux in nuclear astrophysics sites as well as the destruction of both ^{7}Li and ^{7}Be. ^{7}Li(p,n)^{7}Be is acting as an neutron source in i and r process reactions in stellar nucleosynthesis. Considering the the neutron spectrum produced in this reaction, it is showing a qusi-monoenergetic behavior upto 2.3 MeV of proton energy, and beyond this the coupling of $1/2^-$ state (429 keV) of ^{7}Be residue is populating results an additional peak in the exit channel neutron spectrum [22]. However people are utilizing this neutrons for measuring neutron induced cross sections, with a correction to the low energy neutrons by spectral indexing [23].

The time reversal of ^{7}Li(p,n)^{7}Be reaction, ie. ^{7}Be(n,p)^{7}Li is also involved in the nuclear astrophysics, and anticipated that it is imparting a major role in the suppression of the anti-neutrino flux along with ^{7}Be(p,γ) reaction to district the ^{7}Be population. There are major attempts has been taken to study the ^{7}Be(n,p)^{7}Li reaction rates, based on n_ToF@CERN. However, due to the ambiguities in the entrance channels, such as the inelastic breakup couplings in the $n +^7$ Be system originated through resonant modes, these cross sections haven't been theoretically explained.

Beyond 3.4 MeV of proton energy, there exist the breakup of the ^{7}Be residue in ^{7}Li(p,n)^{7}Be reaction, resulting a breakup continuum coupling to the ejectile neutron wave function results a continuum neutron spectrum in the exit channel. McNaughton et al. measured these neutron spectrum using pulsed protons and showed that there is a significant level of continuum neutrons are present [24]. There is no further measurements existing currently in literatures. The continuum neutron distribution is being anticipated due to the coupling of residual ^{7}Be to the exit channel neutron spectrum which leads to a three body process. Due to the effect of residual breakup, the experimental residue cross sections for ^{7}Li(p,n)^{7}Be reported in EXFOR is also showing a similar fall beyond 5 MeV of

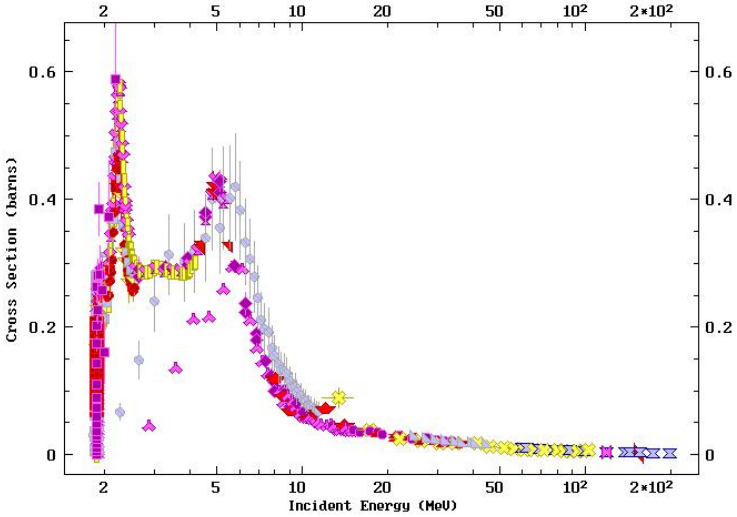

Figure 1.1: The ^{7}Li(p,n)^{7}Be excitation function from EXFOR-Compiled datasets.

proton energy. The experimental excitation function is shown in in Fig. 1.1. However, these are neither reproduced by the statistical calculations performed with statistical model codes. And there is not any reports existing about the impact of the breakup couplings in ^{7}Li(p,n) reaction and exit channel neutron spectrum.

Further a detailed evaluation has been performed by J. W Meadows and D. L Smith [25], however it failed towards the qualitative explanation for the continuum neutron colony based on empirical approaches. Further, S. G. Mashnik et al. attempted to reproduce the neutron continuum using GNASH calculations with considering ^{7}Li$(p, n\alpha)^{3}$He reaction via pre-equilibrium exciton approach [26]. However, this could also not accurately reproduce the neutron spectrum, due to the limitations in defining excitation states and addressing a different physics.

Due to the role of ^{7}Li(p,n)^{7}Be$^{*} \rightarrow n +^{3}$ He $+ \alpha$ reaction in the nuclear astrophysics and the nuclear data measurements, the knowledge on the breakup neutron distribution is required for the measurement of neutron induced reaction cross sections. Further the breakup coupled excitation function necessitates for the BBN Network calculations. However, for quantifying the breakups, the

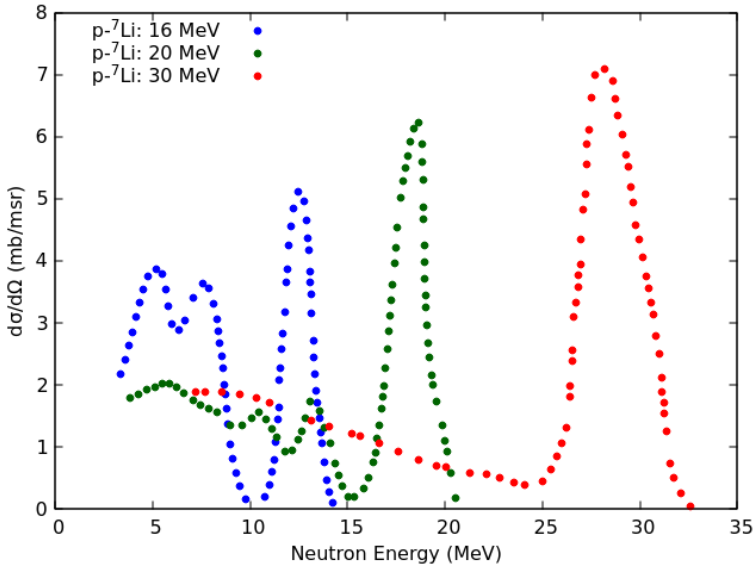

Figure 1.2: The Experimental ^{7}Li(p,n) neutron spectrums corresponding to 16, 20 and 30 MeVs by McNaughton et al.

breakup fragments from each continuum states has to be measured and have to be reproduced through CDCC˙CRC calculations.

1.3.3 Radiative Capture in Li isotopes

Neutron reactions on Li isotopes are having a renewed interest due to their involvement in nuclear astrophysics [27, 28, 29]. Though ^{6}Li(n,γ) reaction is having a significant importance, the reaction remains, thus for, unexplored. As the abundance ratio of ^{6}Li to ^{7}Li is used as an observable for estimating the time scale of stellar evolution, the reaction is having a major role in the Standard Big Bang Nucleosynthesis (SBBN) network calculations[27, 30, 31]. Further, ^{6}Li(n,t) and ^{6}Li(n,n′t) reaction contribute to the ^{3}H breading in fusion reactors [32]. The abundances of ^{6}Li and ^{7}Li are highly influenced by the ^{6}Li(n,γ) reaction rates.

It is well known that the impact of coupling of the resonant states of the residue to the entrance channel produces the resonance enhancements in the radiative capture. The excitation function for ^{7}Li(n,γ) measured by Imhof et al. is showing the resonance enhancement in the excitation function corresponding to the 3^{+} (2.25 MeV) state. However this resonance has been absent in the measurement by Iszak et al. [33, 34] by utilizing the Coulomb deposition

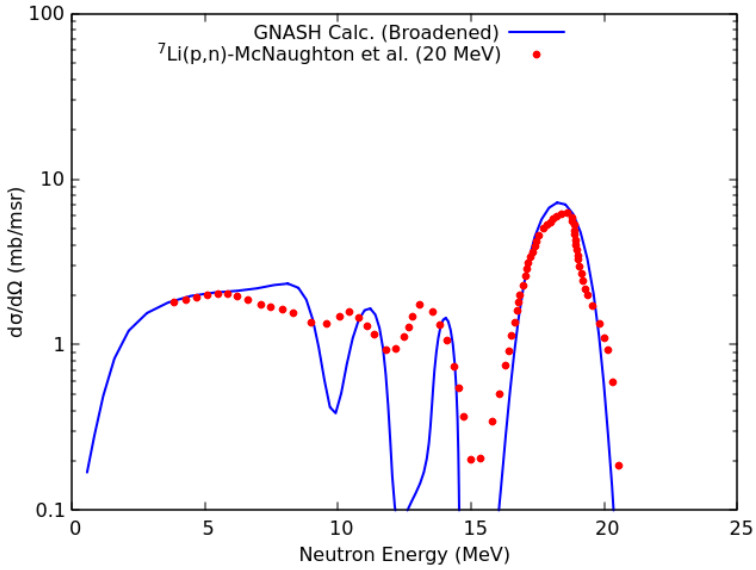

Figure 1.3: ^{7}Li(p,n) neutron spectrum at 20 MeV and GNASH calculations

method. The recent measurement of ^{7}Li(p,n) and ^{7}Li(α,n), measured through CERN n_TOF facility through time reversal of ^{7}Be(n,p) and ^{7}Be(n,α)is also not exhibiting the resonance enhancements even though the resonant states of ^{8}Be ^{11}B and ^{10}B are existing in this energy range [35, 36]. However there is not any theoretical explanations in wiping out of these resonances in the excitation functions of reactions. These wiping effects are anticipated due to the residual breakup couplings, and a detailed CDCC-CRC calculations are required to get a picture on the systematics of this effect.

Considering the ^{6}Li(n,γ), the neutron capture Q-Value, 7.2 MeV, is higher than ^{7}Li $\rightarrow \alpha + t$ breakup threshold of -2.46 MeV. Thus the final state produced is always above the breakup threshold of ^{7}Li. This results a electromagnetic coupling from initial capture states to final states, overlapped by the ^{7}Li $\rightarrow \alpha + t$ continuum. There is no experimental data existing with explanation for resonant and continuum coupling effects in the ^{6}Li(n,γ) cross sections. The ENDF/B-VIII.0 evaluated cross sections for ^{6}Li(n,γ), generated by fitting r-matrix formalism on ^{6}Li(n,α) shows an enhancement in the resonant coupled region, while incorporating the resonant states. However the JEEF-3 evaluations shows a decrease in cross sections as the resonant states are being coupled.

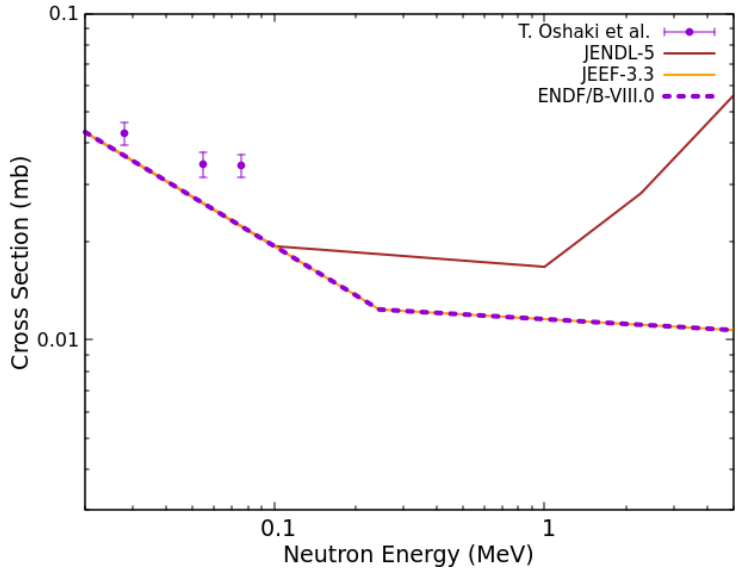

Figure 1.4: ^{6}Li(n,γ) excitation functions by ENDF/B-VIII.0, JEEF-3 evaluations and the measurement by T. Oshaki et al.

However, the exact information on the impact of coupling of unbound resonant states on radiative capture is unknown in the current scenario. The only a single measurement of ^{6}Li(n,γ) cross sections is existing by T. Oshaki et al., and is at excitation energies are below the unbound resonant states are being populated.

The photon induced breakups can produce cutting edge information on the breakup mechanism, especially the resonant breakups, produced in the radiative capture reactions. In radiative capture, the coupling of resonant states are initiated in electromagnetic mode. Hence the breakups initiated by the real photons on the residues of radiative capture will be an alternative to study the breakup coupling modes in the capture reactions, which provide the information on the vanishing of resonant components. Holding this motivation an experiment to study the inclusive α production in ^{7}Li$(\gamma,\alpha)^{3}$H , with bremsstrahlung photons, has been tried. For this the bremsstrahlung spectrum has been accurately measured in a novel approach [37]. However, the experiment has been failed due to the scattered photons induced pileup, which could not be managed by adjusting the CFD thresholds.

The ^{7}Li(p,n) charge exchange reaction shows anomalies in the resonant and

continuum neutron spectra, particularly in the region of unbound resonance coupled excitation function, raising questions about couplings and overlaps in the breakup continuum. To understand the nuclear reaction mechanism and resolve this anomaly, precise measurement and analysis of reaction cross sections for each component are essential, along with theoretical considerations.

To address this, the ^{7}Li(p,n)^{7}Be$^* \rightarrow n+^3$He$+\alpha$ reactions are studied, focusing on the couplings and overlap effects for ^{7}Be $\rightarrow^3$ He $+ \alpha$, ^{7}Li(n,γ) cross sections involving the coupling of 3^+ state of ^{8}Li, and ^{6}Li(n,γ) cross sections influenced by $5/2^-, 7/2^-$, and $3/2^-$ states overlapped by $^7\text{Li} \rightarrow \alpha + t$ breakup continuum. These measurements hold significant potential for understanding the reaction dynamics.

Bibliography

[1] Isobel Falconer. J j thomson and the discovery of the electron. *Physics Education*, 32(4):226, jul 1997.

[2] Gegier H. and Marsden Ernest. On a diffuse reflection of the α-particles. *Proc. R. Soc. Lond.*, A82:495–500, jul 1909.

[3] Professor E. Rutherford F.R.S. Lxxix. the scattering of α and β particles by matter and the structure of the atom. *The London, Edinburgh, and Dublin Philosophical Magazine and Journal of Science*, 21(125):669–688, 1911.

[4] H. Geiger Ph.D. and J.M. Nuttall B.Sc. Lvii. the ranges of the α particles from various radioactive substances and a relation between range and period of transformation. *The London, Edinburgh, and Dublin Philosophical Magazine and Journal of Science*, 22(130):613–621, 1911.

[5] G. Gamow. Zur Quantentheorie des Atomkernes. *Zeitschrift fur Physik*, 51(3-4):204–212, March 1928.

[6] Cockcroft John Douglas and Walton E. T. S. Experiments with high velocity

positive ions. II. -The disintegration of elements by high velocity protons. *Proc. R. Soc. Lond. A*, 137:229–242, 1932.

[7] Niels Bohr. Neutron Capture and Nuclear Constitution. *Nature*, 137:1476–4687, 1936.

[8] S. N. Ghoshal. An experimental verification of the theory of compound nucleus. *Phys. Rev.*, 80:939–942, Dec 1950.

[9] Niels Bohr and John Archibald Wheeler. The mechanism of nuclear fission. *Phys. Rev.*, 56:426–450, Sep 1939.

[10] Uttiyoarnab Saha, K. Devan, and S. Ganesan. A study to compute integrated dpa for neutron and ion irradiation environments using srim-2013. *Journal of Nuclear Materials*, 503:30–41, 2018.

[11] Alan L Nichols, F Meiring Nortier, and R Capote Noy. Summary report of the third research coordination meeting on nuclear data for charged-particle monitor reactions and medical isotope production. Technical report, International Atomic Energy Agency, 2017.

[12] Mark B Chadwick, Paul M DeLuca Jr, and Robert C Haight. Nuclear data needs for radiation protection and therapy dosimetry. Technical report, Los Alamos National Lab.(LANL), Los Alamos, NM (United States), 1995.

[13] Wayne D Newhauser and Rui Zhang. The physics of proton therapy. *Physics in Medicine & Biology*, 60(8):R155, mar 2015.

[14] R. J. de Meijer and R. Kamermans. Breakup phenomena in nuclear collision processes with he projectiles. *Rev. Mod. Phys.*, 57:147–209, Jan 1985.

[15] T. Tamura, W.R. Coker, and F. Rybicki. Distorted wave born approximation for nuclear reactions. *Computer Physics Communications*, 2(2):94–106, 1971.

[16] D. Chattopadhyay, S. Santra, A. Pal, A. Kundu, K. Ramachandran, R. Tripathi, T. N. Nag, and S. Kailas. Direct and resonant breakup of radioactive ^{7}Be nuclei produced in the ^{112}Sn(^{6}Li,^{7}Be) reaction. *Phys. Rev. C*, 102:021601, Aug 2020.

[17] D. Chattopadhyay, S. Santra, A. Pal, A. Kundu, K. Ramachandran, R. Tripathi, B. J. Roy, Y. Sawant, B. K. Nayak, A. Saxena, and S. Kailas. Resonant breakup of ^{8}Be in ^{112}Sn(^{7}Li,^{8}Be $\rightarrow$ 2α) reaction. *Phys. Rev. C*, 98:014609, Jul 2018.

[18] Ian J. Thompson. Coupled reaction channels calculations in nuclear physics. *Computer Physics Reports*, 7(4):167–212, 1988.

[19] K. Rusek, P. V. Green, P. L. Kerr, and K. W. Kemper. Continuum-discretized coupled-channels analysis of $^{6}\vec{\text{li}}$ +^{4}He scattering at $E_{\text{c.m.}}$ = 11.1MeV. *Phys. Rev. C*, 56:1895–1901, Oct 1997.

[20] N. C. Summers and F. M. Nunes. ^{7}Be breakup on heavy and light targets. *Phys. Rev. C*, 70:011602, Jul 2004.

[21] A. Pakou, O. Sgouros, V. Soukeras, F. Cappuzzello, N. Keeley, L. Acosta, C. Agodi, X. Aslanoglou, S. Calabrese, D. Carbone, M. Cavallaro, A. Foti, G. Marquínez-Durán, I. Martel, M. Mazzocco, C. Parascandolo, D. Pierroutsakou, K. Rusek, E. Strano, V. A. B. Zagatto, and K. Zerva. Exclusive breakup of ^{7}Li incident on a proton target at 5.44a mev. *Phys. Rev. C*, 95:044615, Apr 2017.

[22] Rebecca Pachuau, B. Lalremruata, N. Otuka, L. R. Hlondo, L. R. M. Punte, and H. H. Thanga. Thick and thin target 7li(p,n)7be neutron spectra below the three-body breakup reaction threshold. *Nuclear Science and Engineering*, 187(1):70–80, 2017.

[23] Smith D.L., Plompen, and Semkova A.J.M. Corrections for low energy neutrons by spectral indexing. *OECD NEA/WPEC-19*, 19, 2005.

[24] M.W. McNaughton, N.S.P. King, F.P. Brady, J.L. Romero, and T.S. Subramanian. Measurements of 7li(p,n) and 9be(p,n) cross sections at 15, 20 and 30 mev. *Nuclear Instruments and Methods*, 130(2):555–557, 1975.

[25] J.W Meadows and D.L Smith. Protons from neutron bombardment of natural lithium. Technical Report ANL-7938, Argone National Laboratory, 1972.

[26] S. G. Mashnik, M. B. Chadwick, P. G. Young, R. E. MacFarlane, and L. S. Waters. ^{7}Li(p,n) nuclear data library for incident proton energies to 150 mev. Technical Report LA-UR-00-1067, Los Alamos National Laboratory, 2000.

[27] Su Jun, Li Zhi-Hong, Guo Bing, Bai Xi-Xiang, Li Zhi-Chang, Liu Jian-Cheng, Wang You-Bao, Lian Gang, Zeng Sheng, Wang Bao-Xiang, Yan Sheng-Quan, Li Yun-Ju, Li Er-Tao, Fan Qi-Wen, and Liu Wei-Ping. Neutron spectroscopic factors of ^{7}li and astrophysical ^{6}li(n,γ)^{7}li reaction rates. *Chinese Physics Letters*, 27(5):052101, may 2010.

[28] Claudia Aguilera-Gómez, Julio Chanamé, and Marc H. Pinsonneault. On lithium-6 as a diagnostic of the lithium-enrichment mechanism in red giants. *The Astrophysical Journal*, 897(1):L20, jul 2020.

[29] Emilio Casuso and John E. Beckman. On the Origin of the Dispersion in the 7Li/6Li Ratio in the ISM. *Publications of the Astronomical Society of Japan*, 55(1):247–255, 02 2003.

[30] Robert A. Malaney and William A. Fowler. On Nuclear Reactions and 9Be Production in Inhomogeneous Cosmologies. *apjl*, 345:L5, October 1989.

[31] Kenneth M. Nollett, Martin Lemoine, and David N. Schramm. Nuclear reaction rates and primordial ^{6}li. *Phys. Rev. C*, 56:1144–1151, Aug 1997.

[32] T. Giegerich, K. Battes, J.C. Schwenzer, and C. Day. Development of a

viable route for lithium-6 supply of demo and future fusion power plants. *Fusion Engineering and Design*, 149:111339, 2019.

[33] W. L. Imhof, R. G. Johnson, F. J. Vaughn, and M. Walt. Cross sections for the $\mathrm{li}^7(n,\gamma)\mathrm{li}^8$ reaction. *Phys. Rev.*, 114:1037–1039, May 1959.

[34] R. Izsák et al. Determining the ^{7}li(n,γ) cross section via coulomb dissociation of ^{8}li. *Phys. Rev. C*, 88:065808, Dec 2013.

[35] L. M. Damone et al. $^7\mathrm{Be}(n,p)^7\mathrm{Li}$ reaction and the cosmological lithium problem: Measurement of the cross section in a wide energy range at n_tof at cern.

[36] M. Barbagallo et al. $^7\mathrm{Be}(n,\alpha)^4\mathrm{He}$ reaction and the cosmological lithium problem: Measurement of the cross section in a wide energy range at n_tof at cern.

[37] C. V. Midhun, M. M. Musthafa, Shaima Akbar, Swapna Lilly Cyriac, S. Sajeev, Antony Joseph, K. C. Jagadeesan, S. V. Suryanarayana, and S. Ganesan. Spectroscopy of high-intensity bremsstrahlung using compton recoiled electrons. *Nuclear Science and Engineering*, 194(3):207–212, 2020.

Chapter 2

Coupled Channel Formalism for Direct Reactions

2.1 Introduction

When a nucleus is approaching a target nucleus, with an impact parameter lesser than the range of nuclear force, it produces an initial capture state for a short instance of time, say $\approx 10^{-22}$s. The force responsible for the initial capture state is the interaction potential between projectile and target. The initial capture state is a totally unbounded state, having an angular momentum $\frac{\sqrt{2\mu E_{rel}}}{\hbar}$, with a relative energy E_{rel}. All other reactions are assumed to be initiated from this initial capture state. The decay of this initial capture state into the initial target-projectile combination is referred as the elastic scattering. Further, if the relative energy of the initial capture state is used for the excitation of the target, it is referred as the inelastic process.

During the inelastic coupling, the relative energy of the initial capture state will be utilized to excite either the projectile or target, thereby the separation between projectile and target (in the Jacobi coordinate) is getting reduced. This reduction in separation results the state is more bounded under the nuclear potential by the action of the imaginary part of nuclear potential. In this mech-

anism, the projectile will be completely absorbed by the target, and an intermediate nucleus is formed. This intermediate nucleus is called the compound nucleus.

While progressing towards the compound nucleus from the initial capture state the system opts for a shell model potential encompassing all nucleons both from the projectile and the target, which then generates a comprehensive level scheme. As the compound nucleus takes form, the state bears an energy of $E_{rel} + Q_{fus}$, where Q_{fus} stands for the fusion Q-value pertinent to the specific target-projectile pairing. Given that this energy surpasses the ground state, in systems with a positive fusion Q-value, nucleons find themselves occupying higher energy levels. Within this energy range, numerous degenerate levels coexist, overlapping one another. Consequently, particles emitted from one level become absorbed by another overlapping level. This intricate emission-absorption interplay persists for a statistically significant period, until a nucleon is eventually expelled from the nucleus. This intricate process endures over an extended time frame, typically up to around $\approx 10^{-16}$ seconds.

If there is not any much of overlapping levels, the nucleon will be separated from the present state itself, within a time scale of $\approx 10^{21}$s. This is referred to the direct reaction. In the direct reaction, the same projectile or a different particle can be ejected out. However, the interaction is limited to a few levels only. During the emission of the ejectile, a final unbound state, analogues to the initial capture state is being formed in the exit channel for a short interval of time, having a relative energy of $\mathrm{E}_{in} - Q_r$, where Q_r is the reaction Q-value. The ejectile and residue are separated from this final unbound state through the process equivalent to the elastic scattering. The potential for the formation of the unbound state is the scattering potential for the ejectile-residue combination.

Based on this picture, the nuclear reaction systematics can be considered in a time dependent scenario. As the projectile approaches the target, it produces an initial capture state. From this state, the projectile will be separated, which leads to the elastic scattering. The initial capture states, which are not decayed out to

initial projectile target combination, leads to the formation of a final unbound state, with a ejectile-residue combination and relative energy of $E_{rel} + Q_{fus}$. The reaction formalism considers that the undecayed flux in the entrance channel is coupled to the exit channel. Further, the inelastic channels produced through excitation of target or residue in the exit channel, projectile or target in the exit channel also couples to the reaction systematics. For the excited states, different states in the same energy can be co-existed. This is referred as the spectroscopic overlaps. Both coupling and overlaps alters the final state wave function and thereby the reaction cross sections also. This picture has been implemented quantum mechanically through Schrödinger equations to get information about the direct reactions. However, the Schrödinger equation can't be solved for each channel, as the other channels are having effect in the desired channel. Hence the formalism has been implemented through the coupled channel method via Distorted Wave Born Approximation method. This is discussed in the following sections.

2.2 Coupled Reaction Channel Formalism

There are numerous channels are being opened up during the nuclear interactions between a target and projectile. Each nuclear reactions are being represented on the basis of their basic states, $|\psi\rangle$ on the Hilbert space. Hence the total wave function for the collision can be represented as the superposition of wave functions associated to the states,

$$|\Psi_{tot}\rangle = \sum_{i=1}^{N} a_i \, |\psi_i\rangle \tag{2.1}$$

Here, the total space of the complete wave function $|\Psi_{tot}\rangle$ is considered as the sum of direct and compound nuclear reaction space. As the present interest on the direct reaction domain, it has to be projected out from the total wave

function with a projection operator $\hat{P}$.

$$|\Psi\rangle = \hat{P}\,|\Psi_{tot}\rangle = \sum_{i=1}^{N} a_i\,|\phi_i(\zeta)\chi_i(\overrightarrow{R})\rangle \tag{2.2}$$

Where, $|\phi_i(\zeta)\rangle = |\phi_{ip}\phi_{it}\rangle$, ϕ_{ip} and ϕ_{it} representing the bound and continuum states of projectile and target respectively for the ith channel. The $\chi_i(\overrightarrow{R})$is the wave function corresponding to the relative separation between projectile and target, of the ith channel. ζ is representing the relative energy between them.

Let $\overline{H}$ be the total Hamiltonian for the system and thereby the Schrödinger equation for the system is expressed as $\left[\overline{H} - E\right]|\Psi_{tot}\rangle$. Since, the wave function is projected to $|\Psi\rangle$, the Hamiltonian has to be projected accordingly to H [1]. That is,

$$H = P\overline{H}P - P\overline{H}Q\frac{1}{Q\overline{H}Q - E - i\epsilon}Q\overline{H}P \tag{2.3}$$

Where,Q = (1-P) and ϵ is a positive infinitesimal quantity. It assumes that a time retarded operator, (1-P) which alters $\overline{H}$ to H, by removing the scattered flux due to other channels from the model space. The $\frac{1}{Q\overline{H}Q-E-i\epsilon}Q\overline{H}P$ represents the perturbation effects produced by all other channels, which are excluded. Thus the total Hamiltonian for the system, in modal space, can be expressed as $\hat{H} = \hat{T}_R + \hat{U}(R)$. The $\hat{U}(R)$ is the optical model potential, represents the effective projectile-target interaction. The $U(R)$ is taken as the sum of the Coulomb potential and the nuclear potential, as a function of R. The nuclear potential is represented as $V(R) + iW(R)$, were

$$V(R) = -\frac{Vo}{1 - exp(\frac{R-R_0}{a_0})} \tag{2.4}$$

$$iW(R) = -i\frac{Wo}{1 - exp(\frac{R-R_i}{a_i})} \tag{2.5}$$

The $V(R)$ represents the real part of the potential, corresponding to the elastic scattering and $iW(R)$ represents the imaginary potential corresponding to all the non-elastic channels. By applying this into the Schr$\ddot{o}$dinger equation,

$$\left[\hat{H} - E\right] |\Psi(\overrightarrow{R})\rangle = 0 \tag{2.6}$$

The wave function can be estimated as the superposition of the incoming and scattered waves, as

$$\begin{aligned} |\Psi(\overrightarrow{R})\rangle &= e^{i\overrightarrow{K}.\overrightarrow{R}} + \Psi^{+}(\overrightarrow{R}) \\ &= e^{i\overrightarrow{K}.\overrightarrow{R}} + A(\theta)\frac{e^{i\overrightarrow{K}.\overrightarrow{R}}}{\overrightarrow{R}} \end{aligned} \tag{2.7}$$

Here the scattering amplitude can be mapped into the differential cross section as,

$$\frac{d\sigma}{d\Omega} = |A(\theta)|^2 \tag{2.8}$$

This shows the deduction of scattering amplitude, for the estimation of the cross section. For that the wave function has to be decomposed to radial and spherical components,

$$|\Psi(\overrightarrow{R})\rangle = \sum_{lm} C_{lm}\frac{f^l(R)}{R}Y_l^m(R,\theta,\phi) \tag{2.9}$$

Here $f^l(R)$ is the radial part of the wave function, obtained by solving the radial part of the Schr$\ddot{o}$dinger equation,

$$\left[-\frac{\hbar^2}{2\mu}\frac{d^2}{dR^2} + \frac{l(l+1)\hbar^2}{2\mu R^2} + U(R) - E\right] f^l(R) = 0 \tag{2.10}$$

The analytical solution for $f^l(R)$ is very tedious, with the optical potential forms. Hence generally uses the numerical solutions of the equation. In order to obtain the complete solution, the integration has to perform upto infinity, which

is not feasible. Hence some boundary conditions has been selected for limiting the integration, based on the consideration that nuclear force is short ranged. The Coulomb field is proportional to $1/R$. Hence an R_m, called matching radius) has been selected as the integration limit, as at R_m, the field is weak enough, which cannot alter the wave function further [2]. Further, it has been taken as, the wave function should be finite at $R \to 0$, hence

$$\lim_{R\to 0} f^l(R) = 0$$

, and

$$f^l(R)|_{R=Rm} \to I_l(R) - S_l O_l(R)$$

Where S_l is the scattering matrix. I_l and O_l are the incoming and outgoing wave functions respectively.

Based on the boundary conditions, $I_l(R)$ and $O_l(R)$ can be solved to

$$I_l(R) = \frac{1}{\sqrt{v}}(KR)h_l^*(KR) \ \propto \ e^{-i(KR-\eta log2KR)} \tag{2.11}$$

$$O_l(R) = \frac{1}{\sqrt{v}}(KR)h_l(KR) \ \propto \ e^{i(KR-\eta log2KR)} \tag{2.12}$$

S_l is the coefficient of scattering matrix, emerging as a function of phase shift, δ_l, and can be expressed as $S_l = e^{2i\delta_l}$. Since the potential, $U(R) = 0$, Ψ_{in} is equal to the Ψ_{in}, so that $\delta_l = 0$. Hence S_l will be equal to the unity. For a real potential, in the absence of inelastic components, δ_l will be real so that $|S_l|= 1$. In the inelastic channels, $U(R)$ will be complex, so that δ_l will be complex. Hence $|S_l|< 1$. For the very larger values of angular momentum, l, the S_l again tends to the unity.

Applying these solutions on equation 2.7, we can write,

$$|\Psi(\overrightarrow{R})\rangle = \sum_{lm} C_{lm} \frac{[I_l(R) - S_l O_l(R)]}{R} Y_l^m(R, \theta, \phi) \tag{2.13}$$

With considering the asymptotic boundary conditions in the presence of Coulomb potential, converging by $\frac{1}{R}$, the scattering amplitude $A(\theta)$ can be expressed as,

$$A(\theta) = \frac{1}{2ik} \sum_{l=0}^{\infty} (2l+1)[e^{2i\eta_l} - 1] P_l(cos\theta) \tag{2.14}$$

Where, η_l is the sum of phase shifts produced by Coulomb and nuclear potentials as $\sigma_l + \delta_l$.Based on the knowledge on the total phase shift, the $A(\theta)$ is expanded by splitting the scattering amplitude due to Coulomb and nuclear. The scattering amplitude is then expressed as,

$$A(\theta) = \frac{1}{2ik} \sum_{l=0}^{\infty} (2l+1)[e^{2i\sigma_l} - 1] P_l(cos\theta) + \frac{1}{2ik} \sum_{l=0}^{\infty} (2l+1) e^{2i\sigma_l} [e^{2i\eta_l} - 1] P_l(cos\theta) \tag{2.15}$$

Substituting this scattering amplitude is then used to obtain the differential cross sections.

Suppose, if two channels are opened in the reaction and projected in the model space, say α and $\alpha\prime$. Then the corresponding Hamiltonian can be expressed based on inter-nucleon separation $(\overrightarrow{R})$ and ζ as,

$$H = -\frac{\hbar^2}{2\mu} \nabla^2 + h(\zeta) + V(\overrightarrow{R}, \zeta) \tag{2.16}$$

And the internal wave function is obtained by solving Schrödinger equation, with internal Hamiltonian $h(\zeta)$ and internal energy ϵ_α as,

$$h(\zeta) \, |\phi_\alpha(\zeta)\rangle = \epsilon_\alpha \, |\phi_\alpha(\zeta)\rangle \tag{2.17}$$

Thus the model wave function can be written as,

$$\Psi(\overrightarrow{R},\zeta) = \phi_\alpha(\zeta)\chi_\alpha(\overrightarrow{R}) + \phi_{\alpha'}(\zeta)\chi_{\alpha'}(\overrightarrow{R}) \tag{2.18}$$

Based on the total wave function, the Schrödinger equation for the total system can be addressed as,

$$H\Psi(\overrightarrow{R},\zeta) = E\Psi(\overrightarrow{R},\zeta) \tag{2.19}$$

Incorporating the total Hamiltonian mentioned in Equation 2.14 and the total wave function in the model wave function given in equation 2.16 in the Schrödinger equation (2.17) has been split into two coupled equations by the rigorous mathematical treatment as,

$$\left[\nabla^2 - U_{\alpha\alpha} + k_\alpha^2\right] |\chi_\alpha(\overrightarrow{R})\rangle = U_{\alpha\alpha'} |\chi_{\alpha'}(\overrightarrow{R})\rangle \tag{2.20}$$

and,

$$\left[\nabla^2 - U_{\alpha'\alpha'} + k_\alpha^2\right] |\chi_{\alpha'}(\overrightarrow{R})\rangle = U_{\alpha'\alpha} |\chi_\alpha(\overrightarrow{R})\rangle \tag{2.21}$$

Where, the $U_{ij} = \frac{2\mu V_{ij}}{\hbar^2}$ and $k_i = \sqrt{\frac{2\mu(E_i - \epsilon_i)}{\hbar^2}}$

Converting the Equation 2.18 into the steady state form, by rearranging,

$$\left[\nabla^2 - (U_{\alpha\alpha} + U_{\alpha\alpha'}\frac{|\chi_{\alpha'}(\overrightarrow{R})\rangle}{|\chi_\alpha(\overrightarrow{R})\rangle}) + k_\alpha^2\right] |\chi_\alpha(\overrightarrow{R})\rangle = 0 \tag{2.22}$$

Here, $U_{\alpha\alpha'}\frac{|\chi_{\alpha'}(\overrightarrow{R})\rangle}{|\chi_\alpha(\overrightarrow{R})\rangle}$ term is modifying the interaction potential $U_{\alpha\alpha}$. It implies that the inclusion of other channels alters the interaction potential for the desired channel. Hence the above term is called the dynamic polarization potential. Hence the effective potential, U_{eff} can be attributed as the sum of bare and

dynamical polarization potential as,

$$U_{eff} = U_{\alpha\alpha} + U_{\alpha\alpha'} \frac{|\chi_{\alpha'}(\overrightarrow{R})\rangle}{|\chi_{\alpha}(\overrightarrow{R})\rangle} \tag{2.23}$$

From this, the Equation 2.18 can be rewritten as

$$\left[\nabla^2 - U_{eff} + k_\alpha^2\right] |\chi_\alpha(\overrightarrow{R})\rangle = 0 \tag{2.24}$$

Since the effective interaction is directly depending on the effective interaction potential, it is necessary to find out the U_{eff}. This require an complete solution of $|\chi_\alpha(\overrightarrow{R})\rangle$ and $|\chi_{\alpha'}(\overrightarrow{R})\rangle$. Generally the iterative methods are employed for obtaining $|\chi_\alpha(\overrightarrow{R})\rangle$ and $|\chi_{\alpha'}(\overrightarrow{R})\rangle$.

The iterative solution is attempted by by setting $|\chi_{\alpha'}(\overrightarrow{R})\rangle = 0$ in the Equation 2.18. This results the solution for $|\chi_\alpha(\overrightarrow{R})\rangle$. This solution is then substituted in Equation 2.19, for estimating the solution for $|\chi_{\alpha'}(\overrightarrow{R})\rangle$ coupled by $|\chi_\alpha(\overrightarrow{R})\rangle$. This will be continued until the convergence of the wave functions.

However, in practical cases, the model space may consists of the channels more than 2 such as α, α', α'' ,α''' etc. Then the coupled channel equation has to be written as,

$$\left[\nabla^2 - U_{\alpha\alpha} + k_\alpha^2\right] |\chi_\alpha(\overrightarrow{R})\rangle = \sum_{\alpha' \neq \alpha} U_{\alpha'\alpha} |\chi_{\alpha'}(\overrightarrow{R})\rangle \tag{2.25}$$

This can only be solved based on the knowledge of all the matrix elements in $U_{\alpha'\alpha}$. Due to the involvement of infinite number of reaction channels, it is practically impossible to solve the coupled channel equation in its own form. Hence an approximation has been introduced to reduce the infinite number of channels to a few strongly coupled channels. The rest of the channels will be neglected, and the negligible effect of them are accounted by the complex optical model potential. This approximation is renowned as the strong coupling approximation for coupled channel [3].

This method, based on the approximation is well reproducing the inelastic

scattering cross sections, however not for the rearrangement collisions. Hence, other approximations has to be attributed for solving the coupled channel equation for reactions.

2.3 Born Approximation Method

Let consider a particle is scattered by a central force. Hence the Schrödinger equation for this can be expressed as,

$$\left[\nabla^2 + k^2\right] |\chi(\overrightarrow{R})\rangle = U(\overrightarrow{R})\, |\chi(\overrightarrow{R})\rangle \tag{2.26}$$

When the scattering potential is switched off,ie. $V = 0$, the Schrödinger equation will be the equation for a free particle as,

$$\left[\nabla^2 + k^2\right] |\chi_0 \overrightarrow{R}\rangle = 0 \tag{2.27}$$

The solution of the free particle equation is the plane wave, $\chi_0 \overrightarrow{R} \approx exp(i\overrightarrow{k}\,\overrightarrow{R})$. In the presence of the scattering potential V, a scattered wave will be introduced in addition with the incident plane wave. Hence considering the general solution of the Schrödinger equation, with the scattering potential,

$$\chi(\overrightarrow{k}, \overrightarrow{R}) = e^{i\overrightarrow{k}.\overrightarrow{R}} - \frac{1}{4\pi}\int \frac{e^{i\overrightarrow{k}.|\overrightarrow{R}-\overrightarrow{R'}|}}{|\overrightarrow{R}-\overrightarrow{R'}|} U(\overrightarrow{R'})\chi(\overrightarrow{k}, \overrightarrow{R'})\overrightarrow{dR} \tag{2.28}$$

Considering the asymptotic solution for the simplification, at $R >> R'$ [4],

$$\chi(\overrightarrow{k}, \overrightarrow{R}) \rightarrow e^{i\overrightarrow{k}.\overrightarrow{R}} - \frac{e^{i\overrightarrow{k}.\overrightarrow{R}}}{4\pi R}\int e^{-i\overrightarrow{k'}.\overrightarrow{R'}} U(\overrightarrow{R'})\chi(\overrightarrow{k}, \overrightarrow{R'})\overrightarrow{dR'} \tag{2.29}$$

Comparing with the form of general wave function, the scattering amplitude can be attributed as,

$$f(\theta, \phi) = -\frac{1}{4\pi}\int e^{-i\overrightarrow{k'}\overrightarrow{R'}} U(\overrightarrow{R'})\chi(\overrightarrow{k}, \overrightarrow{R'})d\overrightarrow{R'} \tag{2.30}$$

Further considering the potential V is very weak, the $\chi(\overrightarrow{k}, \overrightarrow{R'})$ can be considered as a plane wave. Hence the scattering amplitude can be approximated to,

$$f_{BA}(\theta, \phi) = -\frac{1}{4\pi} \int e^{-i\overrightarrow{k'}\overrightarrow{R'}} U(\overrightarrow{R'}) e^{-i\overrightarrow{k}\overrightarrow{R'}} d\overrightarrow{R'} \tag{2.31}$$

This approximation is renowned as the Born Approximation.

The Born approximation is not always be valid. In practical cases, all the potentials having an elastic as well as an nonelastic part. Hence the potential can be split into an elastic and nonelastic part, as the total potential $U = U_1 + U_2$. Since the solution for U_1 is well known, the scattering amplitude can be expressed as,

$$f_{DWBA}(\theta, \phi) = f_1(\theta, \phi) - \frac{1}{4\pi} \int \langle \chi_1^{(-)}(\overrightarrow{k'}, \overrightarrow{R'}) | \, U_2(\overrightarrow{R'}) \, | \chi_1^{(+)}(\overrightarrow{k'}, \overrightarrow{R'}) \rangle \, d\overrightarrow{R'} \tag{2.32}$$

This approximation is valid for the both inelastic and rearrangement collisions. As U_1 is chosen as the potential for the elastic scattering potential, the $f_1(\theta, \phi)$ will be emerged as the elastic scattering amplitude. The U_2 is representing the nonelastic interaction in this respect. The validity of of DWBA is directly depending on the elastic scattering. In this respect the elastic scattering is taken as the primary process and other events can be considered as a perturbation.Hence the reaction $X(a, b)Y$ can be expressed for the transmission amplitude as.

$$f_{DWBA}(\theta, \phi) = -\frac{1}{4\pi} \int \langle \chi_\beta^{(-)}(\overrightarrow{k_\beta}, \overrightarrow{R_\beta}) | \, U_2^{\alpha,\beta} \, | \chi_\alpha^{(+)}(\overrightarrow{k_\alpha}, \overrightarrow{R_\alpha}) \rangle \, d\overrightarrow{R_\alpha} d\overrightarrow{R_\beta} \tag{2.33}$$

The wave function, χ_α is describing the elastic scattering of $a + X$ in the entrance channel, with the optical potential defined by U_α. χ_β is representing the exit channel wave function produced by the elastic scattering of $b + Y$ in optical potential U_β. Here U_β is producing the non-elastic transition. Hence the parameterization of U_β is depending upon the reaction channel (the exit channel mainly) and the model chosen to describe the mechanism.

Let expand the formulation based on the angular momentum, produced by

the oscillatory energy gained by the n_c particles in the transfered cluster. By considering the angular momentum, l, carried by each particles in the cluster, it can be expressed as $\sum_{i=0}^{n_c} 2(n_i-1)+l_i = 2(N-1)+l$ as the available levels. Hence the differential cross section with accounting all partial waves can be attributed as,

$$\left(\frac{d\sigma}{d\Omega}\right)_{DWBA} = \frac{\mu_\alpha \mu_\beta}{2\pi\hbar^2}\frac{K_\beta}{K_\alpha}\frac{1}{(2J_a+1)(2J_A+1)}\sum |f_{DWBA}(\theta,\phi)|^2 \tag{2.34}$$

The solution to the Equation 2.31 require an integration over six dimensional space, over R_α and R_β. However, for practical purposes an approximation has been taken that the ejectile particle is emitting from the same point, were the projectile is got absorbed. This is renowned as the zero range approximation. This limits the integral in the model space into two dimensional. However, this is valid only if the momentum carried by the transfered particle is very less to give a recoil momentum to the residue. The finite range approximation is more accurate to solve the Equation 2.31, as it keeps the six dimensional integration. However, the integral limit has to be chosen to a finite interval for the solution.

As the number of nodes available for the reaction is unknown, the DWBA calculated cross sections differ from the experimental cross sections. For a well defined states, the ratio between theoretical and experimental cross sections are defined as the spectroscopic factor. The spectroscopic factor reviles the structural information of the particular level. So the relation between experimental and theoretical cross sections is expressed as,

$$\left(\frac{d\sigma}{d\Omega}\right)_{exp} = (C^2S)_1(C^2S)_2\left(\frac{d\sigma}{d\Omega}\right)_{DWBA} \tag{2.35}$$

Here, the $(C^2S)_1$ and $(C^2S)_2$ are the factors corresponding to the overlap between initial and final bound state wave functions of the projectile and target. And this $(C^2S)_1(C^2S)_2$ is taken as the spectroscopic factor.

2.4 Continuum Discretized Coupled Channel

Since a weakly bounded projectile or target is experiencing a nuclear field or a Coulomb field, the weakly bound nuclei breaks into clusters. The relative movement of the broken clusters produces new unbound excited states, having energy E_{rel} and spin,$J = \frac{\sqrt{2\mu E_{rel}}}{\hbar} + \sum_i s_i$, Where μ is the reduced mass for the broken mass system, S_i is the spin of the ith fragment. $\frac{\sqrt{2\mu E_{rel}}}{\hbar}$ represents the angular momentum gained by the relative motion for the fragments with relative energy E_{rel}. These states are continuum in nature, infinite and unnormalizable, in comparison with the bound states, which are discrete, finite and normalizable. These states are also couples to the reaction, like the bound states. However, this cannot be treated as a perturbation, because of the multistep phenomena.

A non-perturbative approach, treating breakup to the all orders, including the effect of nuclear and Coulomb is used to account the breakup, renowned as the Continuum Discretized Coupled Channel (CDCC) method. In this approach, the unbound continuum states are being represented as the discretized continuum, such that the wave functions are normalizable. This is established by replacing the continuum with a finite set of square integrable discrete states in coupled channel calculations. There one of the most used method for the continuum discretization is the bin method, where the discrete states are constructed from the scattering states, based on the angular momentum of the state, gained by the relative motion of the fragment.

Considering a breakup reaction, $a + A \rightarrow b + c + A$, where projectile a is breaking into b and c by the influence of the A. Let us conceder the final state in the Jacobi co-ordinates, as illustrated in Figure 2.1. Here $\overrightarrow{r}$ connects the center of masses of the breakup fragments b and c. $\overrightarrow{R}$ is the vector connecting the center of mass of the target and the center of mass of the breakup fragments. Hence, based on this, the three body Hamiltonian can be expressed as,

$$H_{3body} = \hat{T}_r + \hat{T}_R + V_{cb} + V_{cA} + V_{bA} \tag{2.36}$$

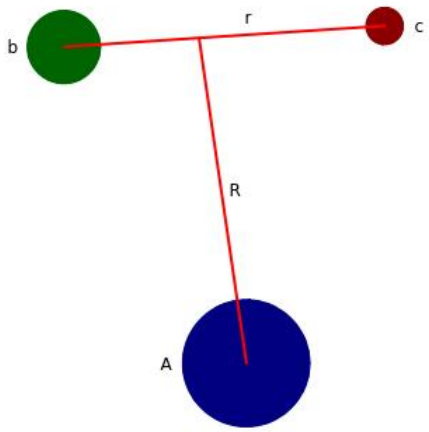

Figure 2.1: The Jacobi Coordinate representation of the breakup fragment interaction with target

Where, $\hat{T_r}$ and $\hat{T_R}$ are the kinetic energy operators corresponding to the relative movement of the fragment, and the center of mass for the fragments in the projectile and target with respect to the target center of mass,in Jacobi Coordinates. The V_{cb} represents the binding potential between fragment c and b, which describes different scattering states. Since the projectile is unboned by the breakup, the interaction potential necessitates the real part of the interaction potential. V_{cA} and V_{bA} are the interaction potential of the individual fragments with the target, containing the real and imaginary parts.

Based on the Jacobi coordinate approach for the 3-body interaction, the 3 body wave function can be represented as the superposition of the bound state wave function and the scattering wave function from the continuum states as,

$$\Psi_{\overrightarrow{K_0}}(\overrightarrow{R}, \overrightarrow{r}) = \phi_0(\overrightarrow{r})\chi_0(\overrightarrow{R}) + \int \phi_{\overrightarrow{k}}(\overrightarrow{r})\chi_{\overrightarrow{K}}(\overrightarrow{R})d\overrightarrow{k} \tag{2.37}$$

Here, $\overrightarrow{k}$ is representing the the momentum between the fragments, generated through the internal relative motion among them. $\overrightarrow{K}$ is the momentum between the projectile and target. The $\overrightarrow{k}$ is connected to $\overrightarrow{K}$ by the energy conservation.

The three body wave function stated in Equation 2.35, it contains an integral over the angular momentum variable upto infinity.Hence, solving the Schr$\ddot{o}$inger

equation for this wave function is not possible as in its own form. Hence it require the continuum wave function to be discretized int a finite set of square integrable basis. In this method, the two adjacent bins will be averaged, and the radial wave functions, for the continuum states $\tilde{U_p}(\overrightarrow{r})$, will be represented as superposition of the scattering eigenstates within the bin defined by the momentum $[k_{p-1}, k_p]$, as

$$\tilde{U_p}(\overrightarrow{r}) = \sqrt{\frac{2}{\pi N_p}} \int_{k_p-1}^{k_p} \omega_p(k) u_k(r) dk \tag{2.38}$$

The $\omega_p(k)$ represents the weight function and N_p is the normalization constant. This transforms the $\tilde{U_p}(\overrightarrow{r})$ into an orthonormal set of wave functions. Hence the total wave function can be represented as the superposition of the wave function from each bin as,

$$\Psi(\overrightarrow{R}, \overrightarrow{r}) \sum_{p=0}^{N} \tilde{\phi_p}(\overrightarrow{r}) \chi_p(\overrightarrow{R}) \tag{2.39}$$

Here, $p = 0$ represents the bound state of the system, before breakup. $p \geq 1$ represents the scattering states above the breakup threshold. By substituting this wave function in the coupled channel formalism, and solve the Schrödinger equation, by the partial wave decomposition and with proper boundary conditions, will result the S-Matrix elements. Here, the assumption has been taken that as the unbound scattering states are being populated, they are completely resulting into the breakup. Hence the exclusive cross sections for the breakup can be obtained.

Bibliography

[1] Herman Feshbach, Arthur Kerman, and Steven Koonin. The statistical theory of multi-step compound and direct reactions. *Annals of Physics*, 125(2):429–476, 1980.

[2] TARO TAMURA. Analyses of the scattering of nuclear particles by collective

nuclei in terms of the coupled-channel calculation. *Rev. Mod. Phys.*, 37:679–708, Oct 1965.

[3] S. T. Butler. On angular distributions from (d, p) and (d, n) nuclear reactions. *Phys. Rev.*, 80:1095–1096, Dec 1950.

[4] M. H. Macfarlane and J. B. French. Stripping reactions and the structure of light and intermediate nuclei. *Rev. Mod. Phys.*, 32:567–691, Jul 1960.

Chapter 3

Impact of ^{7}Be breakup on ^{7}Li(p,n) Reaction

3.1 Introduction

^{7}Li(p,n)^{7}Be is one of the popular charge exchange reaction used for producing quasi monoenergetic neutrons. The reaction having a threshold of 1.8 MeV, and above this the reaction cross section is increasing continuously. Further, Corresponding to the 429 keV resonance of ^{7}Be, there exist a sharp resonance in the ^{7}Li(p,n)^{7}Be excitation function. The experimental cross section for ^{7}Li(p,n)^{7}Be reaction is illustrated in Fig. 3.1. Above the 5 MeV of proton energy, the excitation function shows a rapid fall, but the neutron yield is not varied much. Further, there is not any enhancement or resonance structures observed in the excitation function corresponding to $7/2^-, 5/2^-$ and $3/2^-$ states of ^{7}Be. This sudden falling behavior of the excitation function is anticipated due to the breakup coupling of residual ^{7}Be. However, there is not any measurements available to validate the coupling of ^{7}Be breakup states to the exit channel wave function.

Due to lower breakup threshold of ^{7}Be (Q value for ^{7}Be$\rightarrow \alpha+^3$He is 1.58 MeV), the residual breakup initiates continuum states in the exit channel ^{7}Li(p,n)^{7}Be and coupled to the exit channel neutron wave function. Further the resonant

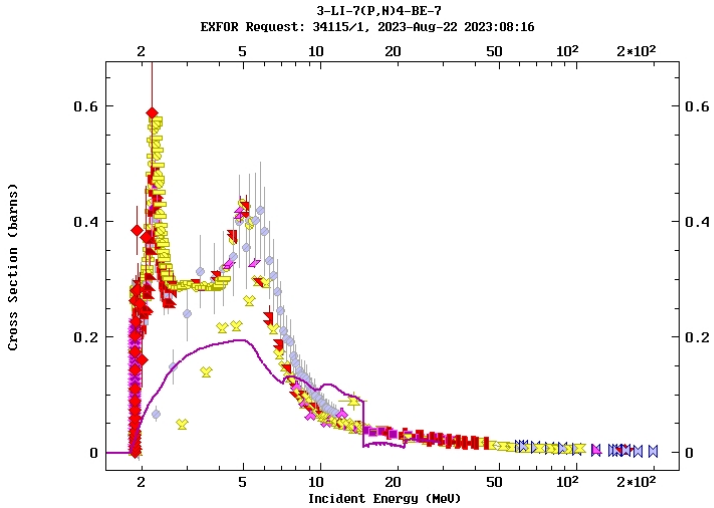

Figure 3.1: The experimental excitation function for ^{7}Li(p,n)^{7}Be reaction with TENDL-2019 evaluations

states above breakup threshold also coupled to the neutron wave function and leads to the breakups through resonances. The result of these couplings will be evident in the ejectile neutron spectrum from ^{7}Li(p,n)^{7}Be. Since, once the breakup states are populated, the state results to the decay of ^{7}Be, so that the residual cross sections will be falling down.

These breakup couplings will be evident in the population of ^{7}Be and the ejectile neutron spectrum. Hence the measurement of exit channel neutron spectrum will be a good observable for observing the couplings. According to the nuclear reaction systematics discussed in chapter 2, the formed neutron(ejectile) and (^{7}Be)residue, in the final state will be subjected to the interaction by the scattering potential defined for $n-^7$Be combination. During this interaction in the final unbound state, the neutron wave function couples to the $\langle^7\text{Be}|\,|\alpha +^3 \text{He}\rangle$ states. Above 3.22 MeV of proton incident energy, (1.64 MeV Threshold for ^{7}Li(p,n) and 1.58 MeV breakup threshold for ^{7}Be to ^{3}He and α) the neutron spectrum behaves as a continuum from 0 to (E$_p$−3.22 MeV). Further the $7/2^-, 5/2^-$and$3/2^-$states are also couples to the exit channel neutron wave function, produces discrete neutron colonies. Besides this, neutron colonies corresponding to the population of ground and $1/2^-$ states below the breakup threshold will also be formed.

Only a few measurements of ^{7}Li(p,n) neutron spectrum above 5 MeV existing in literatures, in the domain which the neutron continuum distribution prominently affects the neutron spectrum. This measurements were performed by McNaughton et. al.[1] and Majerle et. al[2], with a $2mg/cm^2$ thick ^{nat}Li target in the neutron time of flight mode, using the pulsed protons from cyclotron. However these works are limited by the weak timing from cyclotron and the thick target effects. There are some important works by S. G. Mashnik et. al.[3], Meadows and Smith [4] and Drosg et. al.[5], to theoretically model the neutron spectrum from ^{7}Li(p,n) reaction, by taking neutron spectrum measured by McNaughton et al. as a reference. However, these evaluations are limited due to the lack of knowledge on the breakup of ^{7}Be residue. Due to the lack of enough experimental data on $^7\mathrm{Li}(p,n)^7\mathrm{Be}^* \rightarrow n + {}^3\mathrm{He} + \alpha$, the neutron spectrum is not well reproduced by evaluations.

Based on the understanding on the coupled channel mechanism, the continuum neutron distribution in the ^{7}Li(p,n), above the three body breakup threshold, is considered to have emerged because of the coupling of continuum levels of ^{7}Be to the outgoing neutron wave function. These continuum levels are originated by the breakup of ^{7}Be followed by the relative motion of $\alpha-$ ^{3}He internal structures, above the breakup threshold of 1.58 MeV. This internal motion is based on the interaction potential between ^{3}He+α. Moreover, other than continuum states, the $5/2^-$, $7/2^-$ resonant states of ^{7}Be also contribute into the breakup, as they are overlapped with the breakup levels. However, these states behaves like a Gaussian peaks in the neutron continuum. This implies that the neutron spectrum has to be determined by accounting the coupling of continuum and discrete states of ^{7}Be to the ^{7}Li(p,n)^{7}Be. For that the experimental measurement of the breakup continuum states and $5/2^-$, $7/2^-$ resonant states are required. In order to describe these couplings, the population of each state has to be explored.

The continuum and resonant breakups of ^{7}Be have been measured by D Chattopatyay et al. and theoretically reproduced through CDCC-CRC calculations [6]. A detailed theoretical exploration on the breakup of ^{7}Be, based on CDCC

calculations, is performed by Summers and Nunes [7] and Keeley et al.[8]. M. Mazzocco et al. experimentally studied the reaction dynamics of ^{7}Be in the field of ^{208}Pb and interpreted with FRESCO-CDCC calculations[9]. Kolata et al. has given a detailed review on the breakup of ^{7}Be based on recent measurements and theoretical studies [10]. Similarly, there important measurements from n_TOF collaboration on ^{7}Be(n,p) and ^{7}Be(n,α) channels, which show a similar coupling of ^{3}He $-\ \alpha$ breakup in the entrance channel [11, 12]. A review on the breakup of ^{7}Li+p has discussed by Pakou et al[13]. However, in these works mentioned above, the entrance or exit conditions are different from the requirements of the present problem. These reactions doesn't contain any breakup couplings. Therefore, these measured cross sections cannot be directly adapted for explaining breakup couplings in ^{7}Li(p,n) reaction.

The measurement of $\alpha-^{3}$He breakup cross sections from the continuum (resonant and non-resonant) states of ^{7}Be requires a coincidence detection of ^{3}He and α, where the sum of break up threshold and relative energy between ^{3}He and α defines the excitation energy of ^{7}Be. However, due to the energy loss and energy and angular straggling of ^{3}He and α in the target, the event reconstruction and tracking excitation energies will be difficult. Such a problem has been emerged in a recent experiment using 1.2 mg/cm^{2} Li target. Due to the issues of straggling and energy loss in the target as well as thicker ΔE detectors, the coincidence events were failed to reconstruct[14]. Hence, the present experiment has been carefully planned and performed, with a specially prepared thin ^{nat}Li target of 20μg/cm^{2}. It made the coincidence detection of ^{3}He and α and reconstruction of the excitation energy of ^{7}Be, achievable due to a minimal energy and angular straggling. The double differential cross sections for ^{7}Li(p,n)^{7}Be$^{*} \rightarrow n+^{3}$He$+\alpha$ are measured and extended to the determination of neutron spectrum. The details are presented in the following sections.

3.2 Materials and Methods

3.2.1 Target Preparation

Two set of targets has been prepared for the experiment, having thicknesses of $20\mu g/cm^2$ and $1.5\mu g/cm^2$ of ^{nat}Li. The target preparations were performed at the Target Laboratory, BARC-TIFR Pelletron Linac Facility, Mumbai. Since the Li is highly reactive and oxidizing, the sample has been handled carefully, with the support of mineral oil. The Li sample has been weighed initially, and placed in between the Teflon plates. This has been passed through the rolling machine for multiple times, until reaching the desired thickness of $1.5\mu g/cm^2$. After rolling, the sample has been measured and cut into desired dimensions. The target preparation procedures has been done in a controlled environment to prevent the oxidization. After obtaining the target into the desired dimensions, it has been moved to the mineral oil to avoid further air contact.

20μg/cm^2 ^{nat}Li target has been prepared through the thermal evaporation method. The target design has been finalized based on obtaining the typical statistics of ^{3}He-α coincidences, a minimum energy loss and straggling to the ^{3}He-α and considering the practical limitations due to the target oxidation. Based on this the target design is chosen as 20μg/cm^2 ^{nat}Li sandwiched between $5\mu g/cm^2$ carbon backing and $5\mu g/cm^2$ Al capping. For this $5\mu g/cm^2$ carbon foil is made by glow discharge sputtering of methane gas on a sopped steel plate. The thickness has been obtained by controlling the sputtering current, gas pressure and sputtering time. The sputtered target has been chopped into the desired thickness, according to the target holder and floated in watter. The floated foils has been mounted on the target holder. The carbon foil mounded target holders has been shifted into a vacuum evaporation setup, having two independent boats made up of molybdenum and tantalum foils. Li sample, suspended in mineral oil has been loaded into the tantalum boat and aluminum in the molybdenum boat. The chamber has been vacuumed to 10×10^{-6}mbar, and during the rough vacuum stage, the mineral oil has been sucked by the rough vacuum pump itself.

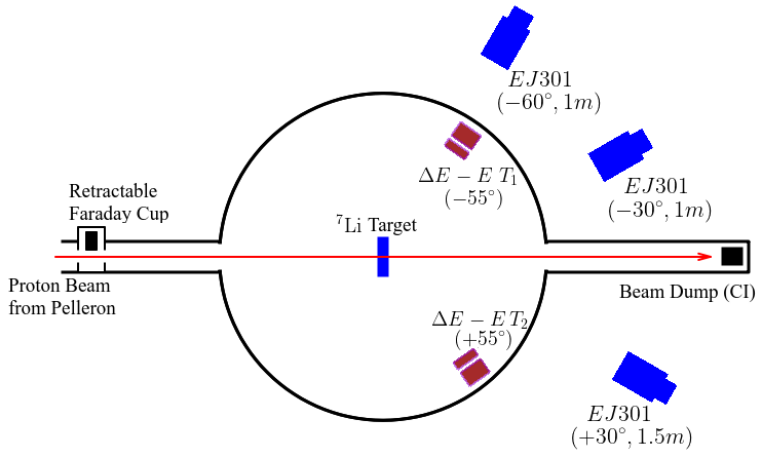

Figure 3.2: Experimental Setup

The Li has been evaporated at first, and the thickness has been monitored by the quartz crystal setup. After obtaining the desired Li thickness of $20\mu g/cm^2$, the Al evaporation has been started. This is performed at a lower rate to obtain the $5\mu g/cm^2$ of the Al capping.

3.2.2 Experimental Setup

The experiment was performed at BARC-TIFR Pelletron-Linac facility, Mumbai, India, using proton beam of 21 MeV. The specially fabricated 20μg/cm^2 ^{nat}Li target with 5μg/cm^2 Al backing and 5μg/cm^2 carbon capping has been used for the experiment. The schematic of the experiment is illustrated in Fig. 3.2.

Two silicon detector telescopes having 25μm and 1500μm ΔE-E pairs, were mounted at $+55°$ and $-55°$ with a distance of 7.5 cm from the target, to record the ejectile particles. This setup produces an angular uncertainty of 0.76°. The ΔE thickness has been chosen as $25\mu m$ to achieve sufficient energy deposition in ΔE detector, to produce electronic signal above the noise level. This thickness also helps to prevent the stopping of ^{3}He and α in the ΔE itself. Three EJ301 liquid organic scintillators with 12.7 cm diameter and 5 cm thick, are configured for measuring neutrons. Two EJ301 detectors are positioned at $-30°$ and $-60°$ at a distance of 1 meter from the target. The third detector was positioned at $+30°$, 1.5 meter from the target for achieving a better time of flight resolution.

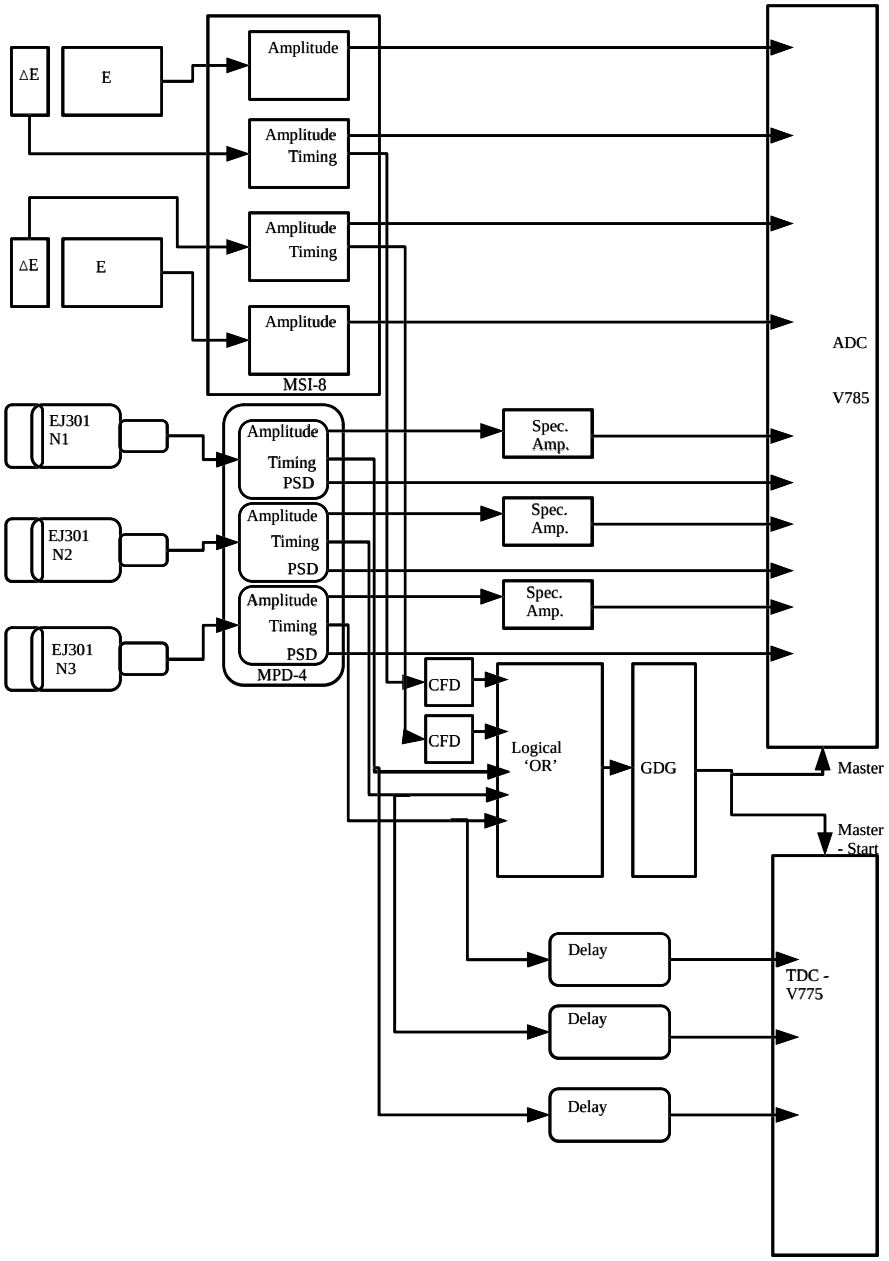

Figure 3.3: Schematics of the Electronics Setup

The silicon detector signals were preamplified using a MESSYTEC MSI-8 preamplifier, having built-in pulse shaping for the energy output. The shaped energy outputs were acquired through CAEN V785 ADC based on VME configuration. The anode (first dynode) output of the EJ301 neutron detector has been connected to Mesytec MPD-4 module for $n - \gamma$ discrimination. The discriminator outputs (PSD), Energy outputs and time trigger has been generated by MPD-4 module. The energy and PSD parameters were accured through the CAEN V775 ADC. Further the neutron detectors were configured in time of flight (TOF) with start from the master. The neutron detector timing signals were generated from the timing output of the MPD-4. The amplitude signals of MPD-4 is further amplified by a linear amplifier, and scaled into the sensitive voltage range of CAEN V785 ADC. The schematic of instrumentation setup is given in Fig. 3.3.

The MASTER trigger for data acquisition is taken as the logical 'OR' of ΔE detectors and time trigger of neutron detectors obtained from MPD-4 module. A time of flight has been generated as MASTER start and Neutron trigger as stop. For this the neutron detector signals were delayed to a 50nS, to correct the weak timing generated from silicon detectors, (around 12nS). CAEN V775 VME TDC was used to generate the time of flight.

A proper CFD has been selected for all the silicon detectors and neutron detectors. The silicon detector telescopes were calibrated using ^{229}Th α source. Neutron detector thresholds were set using ^{137}Cs sources. The TDCs were calibrated using ORTEC-462 time calibrator module.

The proton beam has been monitored using a Faraday cup configuration at the beam dump. The Beam dump has been configured at 3 meter away from target, and shielded with wax followed by the lead blocks to shield neutrons and γs from the dump, as they triggers the neutron detectors. Since the dump is at a longer distance and unsuppressed, the beam loss on the path from target to the dump will be significant. Hence an another, retractable Faraday cup has been configured, immediately before the target. The ratio between the both Faraday

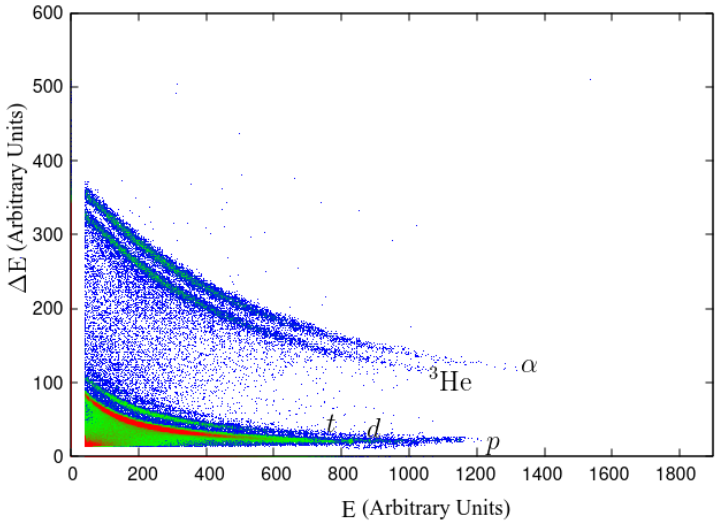

Figure 3.4: $\Delta E - E$ correlation spectra measured by -55° telescope

cup readouts has been chosen for scaling the current readout. The dump has been connected to a digital current integrator. The digital current integrator output was connected to a gate and delay generator (GDG) and multiple copies of the current integrator trigger has been generated. One of the copy has been connected to a VME based scaler and acquired with run. The other copy has been connected to a rate meter, to monitor the beam current stability. An asymmetric slit has been opened for maintaining the beam profile on the target, and the slit currents also monitored to ensure and maintain the optics parameters of the beam.

3.3 Data Analysis

3.3.1 Event Reconstruction and Data Analysis

The data acquisition has been performed with the triggers generated from 'OR'ed signals of ΔE detectors and neutron detectors, which are stabilized by the CFD thresholds. E-ΔE correlation of the recorded events in telescope 1 is illustrated in Fig. 3.4. The α bands gated with ^{3}He events resolves the α particle events in coincidence with ^{3}He. This contains some of the α particles produced from the reaction ^{6}Li(p,α)^{3}He, along with $^3\mathrm{He} - \alpha$ coincidences from $^7\mathrm{Li}(p,n)^7\mathrm{Be}^* \rightarrow$

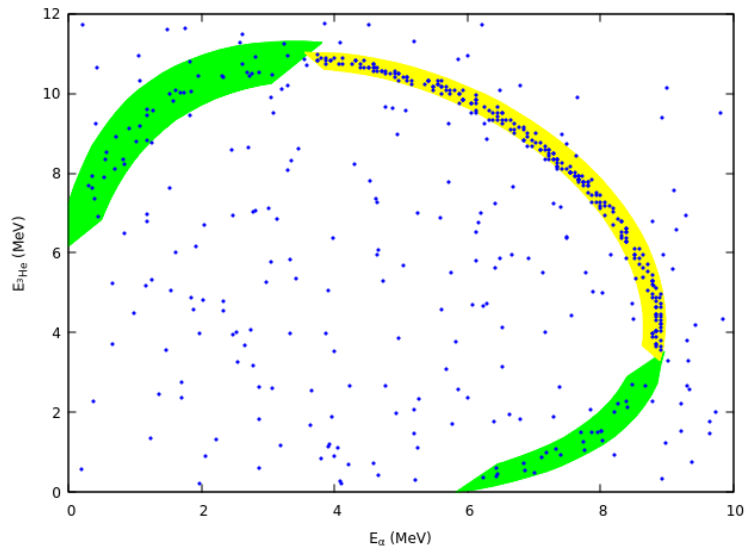

Figure 3.5: The ^{3}He-α Coincidences with K_{nn} window based on 3 body kinematics

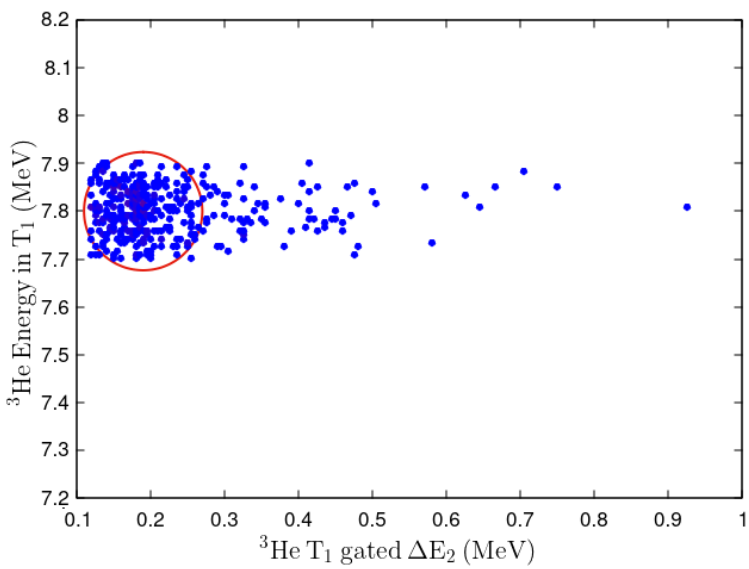

Figure 3.6: An example energy correlation plot of the Energy measured in -55° versus energy of resolved ^{3}He in +55°, for the coincidence events, used for reconstruction of αs below the discrimination threshold. Red circle indicates the constant radius (Δ) window about kinematically defined query point

$n + {}^3\text{He} + \alpha$. In addition, the random α will also be possible due to the limited solid angles and higher master rates. Isolation of the events corresponding to ^{7}Li(p,n)^{7}Be* $\rightarrow$ n+^{3}He+α reaction have been performed by introducing fixed radius nearest neighborhood approach $FR - K_{nn}$[15, 16]. $FR - K_{nn}$ approach has been applied based on the kinematics of the reaction. The ^{7}Li(p,n)^{7}Be* $\rightarrow$ n+^{3}He+α reaction is following a three-body kinematics, hence the kinematically allowed energies($E_{^3He}$ & E_α) corresponding to detector angles for the 21 MeV beam energy was taken as the quarry point for $FR - K_{nn}$. The quarry point has been estimated using

$$\frac{1}{m_3}(E_1(m_1+m_2)+E_2(m_2+m_3)-2(m_p m_1 E_p E_1)^{\frac{1}{2}}\cos(\theta_1) \\ -2(m_p m_2 E_a E_2)^{\frac{1}{2}}\cos(\theta_2)+2(m_1 m_2 E_1 E_2)^{\frac{1}{2}}\cos(\theta_{1.2}) = Q_3 + E_p(1-\frac{m_p}{m_3}) \quad (3.1)$$

Where $\cos(\theta_{1.2}) = \cos(\theta_1)\cos(\theta_2) + \sin(\theta_1)\sin(\theta_2).cos(\phi_1 - \phi_2)$. The constant radius for the event identification is then considered as a window centered at quarry point, and is taken as,

$$\Delta = \sqrt{\sigma_{T1}^2 + \sigma_{T2}^2} \quad (3.2)$$

where σ_{T1} and σ_{T2} are the energy resolution of the respective telescope. This accepts ^{3}He$-\alpha$ coincidence events having both $E_{^3He}$ & E_α that are inside the window. This makes the isolation of ^{7}Li(p,n)${}^7Be^*$ $\rightarrow$ n+^{3}He+α events by removing ^{6}Li(p,α)^{3}He and other random coincidences, as ^{6}Li(p,α)^{3}He is having a Q Value of +4.019 MeV, is different from 3.2 MeV. These, energy and particle identified events are addressed as the 'true events'. The other events such as, p+^{27}Al$\rightarrow$^{3}He + α + ^{21}Ne and p+^{12}C$\rightarrow$^{6}Li+^{3}He+α from aluminium and carbon present in the target, are not contributing to the present measurement as the thresholds for these channels are 22.6 MeV and 26 MeV respectively. The ^{6}Li(p,α)^{3}He events are two order lesser due to low cross section and lower percentage of ^{6}Li present in the target. Hence they are not subjected to the random coincidences in the K$_{nn}$ window. The acquired events with event selection window is illustrated in Fig. 3.5.

Further, there are events with E_α below the particle discrimination threshold of the telescope with coincident ^{3}He being above the particle discrimination threshold of the telescope, or vice versa. Such events are predicted by the three body kinematics calculation. The events below the particle discrimination threshold has been anticipated as they are completely stopped in the ΔE detectors itself. These events were reconstructed by adapting the nearest neighborhood approach. Thin gates were defined in the region of resolved ^{3}He/^{4}He band, for the energies, the kinematics predicts the possibility of counter particle appears below the particle discrimination threshold. A correlation plot between energies in telescope 1 verses telescope 2, under the defined thin gate has been generated. The quarry point has been defined with the three body kinematics. The fixed radius has been taken as,

$$\Delta = \sqrt{{\sigma_{tel}}^2 + {\Delta_{gate}}^2 + {\sigma_{\Delta E}}^2 + E_{strag}} \tag{3.3}$$

where σ_{tel} is the energy resolution of the telescope which identified the particle. Δ_{gate} is the energy width of the gate applied on the particle band and $\sigma_{\Delta E}$ is the energy resolution of the ΔE detector which detects the counter particle. Further E_{strag} is the energy straggling of the particles, having low energy, inside the target. E_{strag} is calculated using SRIM calculation for the particular target geometry, for the energy ranges. However the E_{strag} found to be less compared to the ΔE resolution, due to the typical target configuration employed. The circular gate defined by the center as query point and radius Δ together forms a event selection criteria for counter-particles. These events have been projected towards the ΔE energy. The centroid of the projected ΔE distribution is taken as the average energy of the coincidence particle event below the particle discrimination threshold. Such events are being addressed as reconstructed events. A typical $E_{^3\mathrm{He}} - \Delta\mathrm{E}$ correlation with event selection gate is illustrated in Fig. 3.6.

The energy state of ^{7}Be has been reconstructed by adding ^{3}He and α energies in each coincidence events. The events were converted into the locally averaged histogram values of $E_{^3\mathrm{He}} + E_\alpha$. Each bin in the histogram represents the breakup

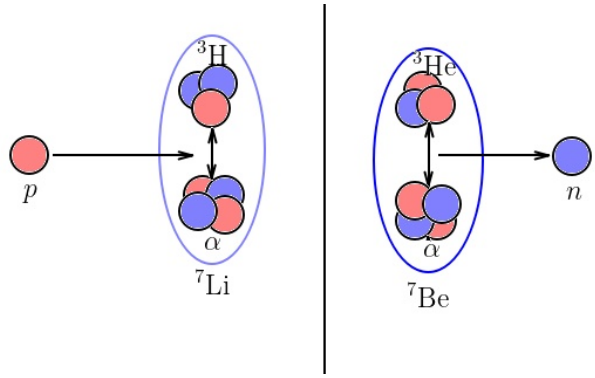

Figure 3.7: Representation of the coupling of neutron wave function to the ^{3}He - α breakup continuum

events of the corresponding energy bin, limited to the laboratory folding angle between ^{3}He and $\alpha = 110°$. The cross sections were calculated using the equation,

$$\frac{d\sigma}{dEd\Omega} = \frac{Y_{(E_{^3He}+E_\alpha)}}{n\Phi} \tag{3.4}$$

where $Y(E_{^3He} + E_\alpha)$ is the counts obtained in each total energy bin, n is the number of ^{7}Li targets per cm^2 and Φ is the proton flux. The doubly differentiated cross sections for the laboratory folding angle between ^{3}He $-\alpha = 110°$.

3.3.2 FRESCO Calculations

Continuum Discretized Coupled Channel (CDCC) calculations using FRESCO [17] has been performed for exploring the physics by reproducing the measured double differential cross sections. The neutron energy distribution in ^{7}Li(p,n)^{7}Be* $\rightarrow n+^3$He $+ \alpha$ is considered as arising due to the coupling of ejectile neutron wave function to the continuum states of ^{7}Be. By obtaining the population cross sections corresponding to the each discretized bin of continuum states, convoluted with the three body kinematics resulting the ^{3}He+α energy distribution at the desired folding angle.

The ^{7}Li(p,n)^{7}Be* $\rightarrow n+^3$He $+ \alpha$ problem has been divided into entrance and exit channel mass partitions with effective coupling between them. The illustration of the mass partition and concept of continuum coupling to the mass partition is given in Fig. 3.7. Entrance channel of the reaction is considered as p+^{7}Li, where the ^{7}Li is treated as α core + t as valance for accounting the

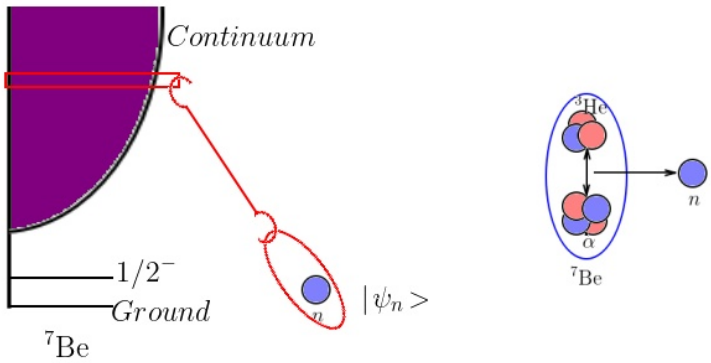

Figure 3.8: Representation of the coupling of neutron wave function to the ^{3}He - α breakup continuum

Table 3.1: Optical Model Potential Parameters for $p+^7$ Li, taken from [18, 19, 20, 21, 22]

Potential	V_0 (MeV)	r_0(fm)	a_0(fm)	V_{sur}(MeV)	r_{sur}(fm)	a_{sur}(fm)
Real	-50.666	1.092	0.677			
Absorptive	-1.993	1.092	0.677	-8.364	1.3121	1.3121
Coulomb		1.895				
Spin-Orbit (Real)	5.286	0.847	0.59			
Spin-Orbit (Absor.)	-0.101	0.847	0.59			

inelastic breakup coupling in the entrance channel. The ^{7}Li states are defined as the CRC states in the entrance channel. $^7\text{Li} \rightarrow \alpha + t$ is attributed by treating α as a core + t as valance in mass partition. The spectroscopy factor for the levels are taken from Kohan & Korath. The effective potential (considering the breakup coupling) for $^7\text{Li} + p$ is taken from [18, 19, 20, 21, 22]. The potential parameters used for $p+^7$Li is given in Table 3.1. The exit channel mass partition as ^{7}Be+n is defined for the lower energies, below breakup threshold. ^{7}Be as α + ^{3}He cluster structure has been considered, for the excitations above 1.59 MeV. Fig. 3.8 illustrates the continuum coupling to the ejectile neutron wave function.

The ^{7}Be states, above $\alpha-^3$He breakup threshold (1.59 MeV), is generated by the discretization of $\alpha-^3$He breakup continuum. The discretization is employed on $\alpha-^3$He relative momentum in the Jacobi Coordinates. The relative angular momentum has been estimated by the relative motion of $\alpha-^3$He fragments with

Table 3.2: Optical Model Potential Parameters for $n +^7$ Be, taken from model by Koning & Delaroche

Potential	V_0 (MeV)	r_0(fm)	a_0(fm)	V_{sur}(MeV)	r_{sur}(fm)	a_{sur}(fm)
Real	-53.211	1.092	0.677			
Absorptive	-0.993	1.092	0.677	-8.9	1.312	0.543
Coulomb		1.09				
Spin-Orbit (Real)	5.286	0.847	0.59			
Spin-Orbit (Absor.)	-0.053	0.847	0.59			

Table 3.3: Optical Model Potential Parameters for ^{3}He $+^4$ He, taken from model by Koning & Delaroche

Potential	V_0 (MeV)	r_0(fm)	a_0(fm)	V_{sur}(MeV)	r_{sur}(fm)	a_{sur}(fm)
Real	-134.893	1.092	0.72			
Absorptive	-26.37	1.271	0.88			
Coulomb		1.18				
Spin-Orbit (Real)	2.5	1.09	0.72			
Spin-Orbit (Absor.)	0.00	1.09	0.72			

Table 3.4: Optical Model Potential Parameters for $n +^4$ He

Potential	V_0 (MeV)	r_0(fm)	a_0(fm)	V_{sur}(MeV)	r_{sur}(fm)	a_{sur}(fm)
Real	-50.67	1.048	0.667			
Absorptive	-0.931	1.048	0.677	-7.787	1.312	0.544
Coulomb		1.048				
Spin-Orbit (Real)	5.452	0.778	0.59			
Spin-Orbit (Absor.)	-0.053	0.778	0.59			

Table 3.5: Optical Model Potential Parameters for $n +^3$ He

Potential	V_0 (MeV)	r_0(fm)	a_0(fm)	V_{sur}(MeV)	r_{sur}(fm)	a_{sur}(fm)
Real	-56.67	1.012	0.667			
Absorptive	-0.937	1.012	0.677	-10.38	1.19	0.544
Coulomb		1.012				
Spin-Orbit (Real)	5.49	0.669	0.59			
Spin-Orbit (Absor.)	-0.053	0.669	0.59			

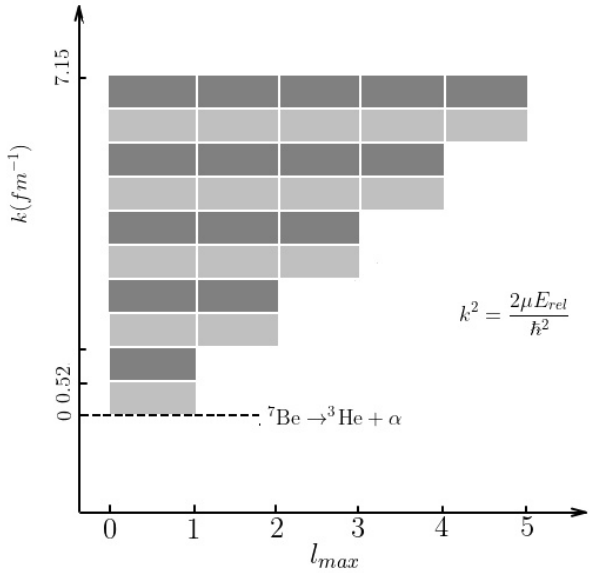

Figure 3.9: Representation of the $^3He - \alpha$ breakup continuum discretized based on the relative angular momentum

a relative energy $E_{rel} = Ecm - 3.2MeV$. Angular momentum ($\hbar$k) up to 7.5fm^{-1} was considered. This range was discretized into a 40 equal bins in an interval of Δk=0.125fm^{-1}. Spin of each bin was obtained as the vector sum of $\alpha-^3$He relative angular momentum and spin of ^{3}He ($1/2^+$). The spin of α is zero itself hence it has no impact. The discretized continuum levels of ^{7}Be is illustrated in Fig. 3.9 Further the resonant states are also added along with discretized continuum states through CRC. Fig. 3.10 illustrates the resonant and continuum levels of ^{7}Be.

The potentials for continuum states and resonant states are defined separately. Interaction of neutrons with the continuum states has been defined with the folding potential. The breakup states were defined with $^3He - \alpha$ interaction potentials, taken from model by Koning & Delaroche. The individual interaction of α+n is defined with the optical potential parameters taken from [23]. The potential parameters corresponding to ^{3}He+n interaction have been obtained by fitting the n$-^3$He elastic scattering angular distribution data reported by M. Drosg [24]. Further the resonant states, $7/2^-$ and $5/2^-$, levels were included as

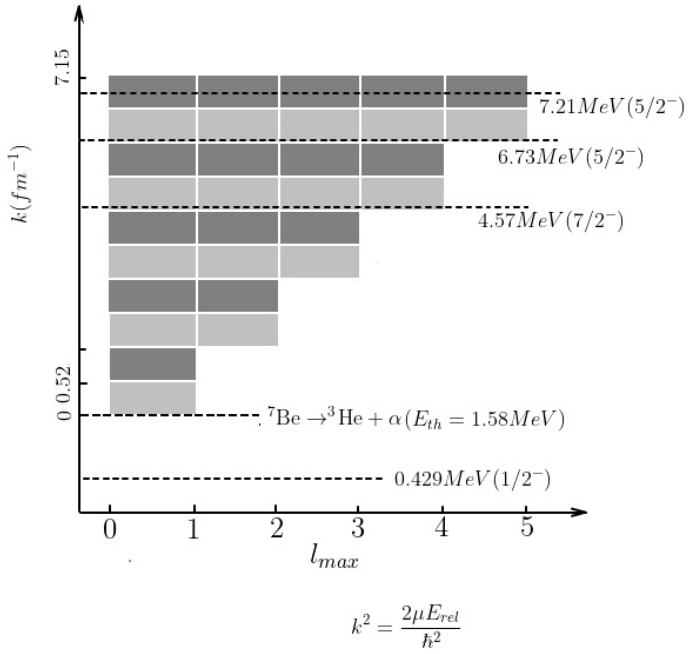

Figure 3.10: Representation of the $^3\mathrm{He} - \alpha$ breakup levels including the resonant states

the CRC states with $^7\mathrm{Be} + n$ potentials effective potentials, taken from Koning & Delaroche.

Spectroscopic Overlaps are defined to consider the overlaps from continuum states produced by α+^{3}He and ^{6}Li+p, above the breakup thresholds of 1.59 and 5.6 MeVs, for the estimation of sequential breakup from the resonant states. The overlaps to the continuum levels is illustrated in Fig. 3.11. While the spectroscopic amplitudes corresponding to continuum and resonant breakups have been adapted from the references [6]. Since the overlaps differ in those cases and the present, a fine optimization has been performed on the spectroscopy Amplitudes. The double differential cross sections for the ^{7}Li(p,n)^{7}Be* $\rightarrow^3$He + α reaction channel were obtained using CDCC-CRC calculations, corresponding to each excitation energy bin. These calculations were then cascaded to obtain the corresponding double differentiated cross sections. To ensure compatibility with experimental conditions, the cascaded cross sections were projected into the laboratory frame at a folding angle of 110° using the three body kinematics calculator available in the nuclear reaction video project[25]. The relative energy

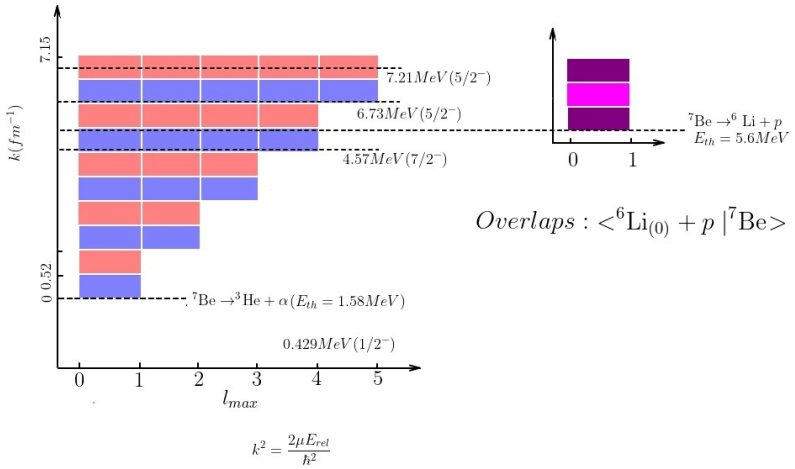

Figure 3.11: Representation of the breakup continuum, resonant states and the spectroscopic overlaps

filter option was utilized during this conversion process.

3.4 Results and Discussion : Events and Double Differential Cross Sections

The energy correlation between ^{3}He and α particles was measured, and it was found to agree with the three-body kinematics predicted for the ^{7}Li$(p,n)^7$Be$^{\rightarrow}n +^3$ He $+ \alpha$ reaction. These measurements were limited to a folding angle of 110° in the laboratory frame with, a smaller solid angle acceptance. However, a reasonable number of events were registered. The resulting ^{3}He-α energy correlation, along with the three-body kinematics, is shown in Fig. 3.12. The retrieved events covers 85% of the kinematic domain of the three body reaction, for the present solid angle acceptance.

The measured double differential cross sections for the continuum states of ^{7}Be are depicted in Fig. 3.13 as the locally averaged histogram values. The experimental cross sections are well reproduced with FRESCO CDCC-CRC calculations for the ^{7}Li$(p,n)^7$Be$^{\rightarrow}n +^3$ He $+ \alpha$ reaction. This demonstrates the physics of neutron continuum formation in this reaction channel. The coupling of breakup levels to the ^{7}Be$+n$ state is responsible for the formation of the con-

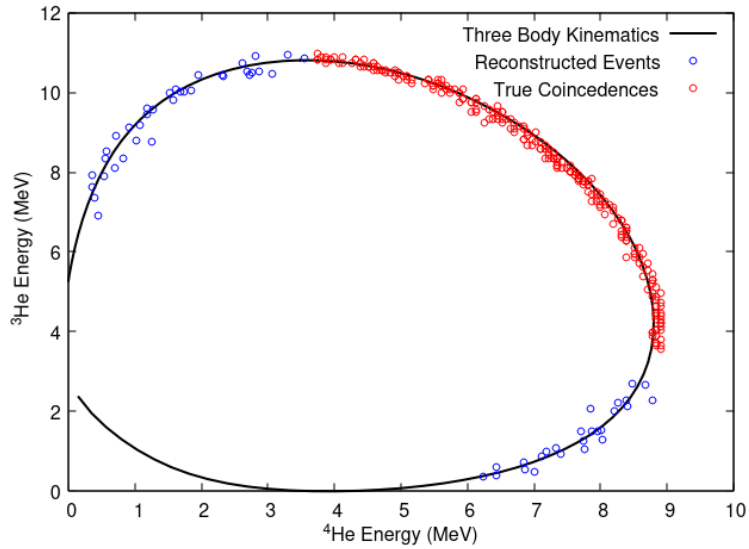

Figure 3.12: The true coincidence and reconstructed events comparison with three body kinematics, projected to the fragments at $+55°$ and $-55°$

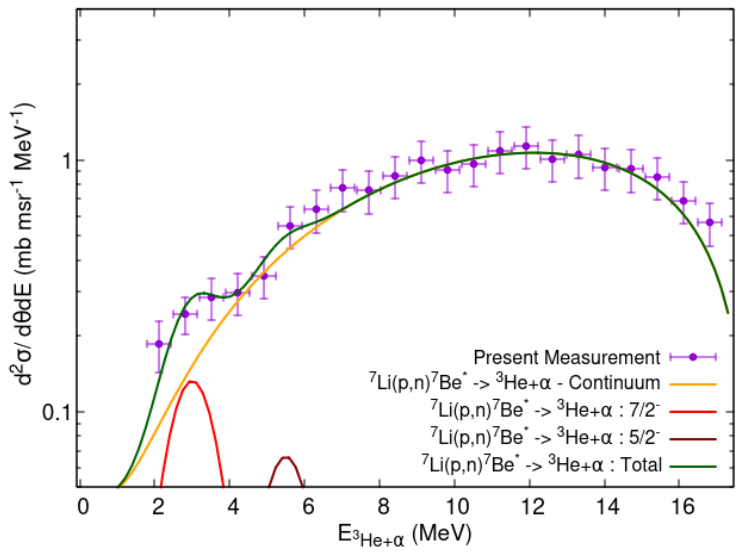

Figure 3.13: The measured double differential cross sections for ^{7}Li(p,n)^{7}Be* $\rightarrow$ n+^{3}He+α, and CDCC-CRC calculated continuum and resonant stare cross sections(for the laboratory folding angle of 110°)

tinuum neutron distribution, as shown by CDCC-CRC analysis. Additionally, there are $7/2^-$ and $5/2^-$ levels above the breakup threshold that contribute as resonant breakups, but their peak contributions are observed with less statistical significance. Nevertheless, these peaks are well-reproduced by CDCC-CRC calculations, which use spectroscopic amplitudes (SA) of 0.26, 1, and 0.57 for the continuum, $7/2^-$, and $5/2^-$ contributions, respectively.

3.4.1 Impact of Couplings in Ejectile Neutron Spectrum

The Monte-Carlo approach was used to generate the full neutron spectrum, incorporating FRESCO calculated cross sections and matching the double differential component with experimental cross sections. To validate the neutron spectrum, ^{3}He event gated neutron bands were identified from the TOF-PSD correlation plots of each neutron detector and projected onto the TOF axis, with the projected histogram converted to the energy spectrum via time calibration. The neutron events corresponding to the ^{7}Li(p,n)$\rightarrow^3$He+α+ n is identified by the fixed radius K_{nn} approach in the ^{3}He energy - neutron energy kinematic correlations. The event selection window for neutrons with acquired events is given in Fig. 3.14. The energy-efficiencies for neutron detectors were simulated using Geant4 up to 16 MeV, as the neutron spectrum extends to this range, and were compared with previously measured efficiencies [26]. The energy-efficiency plot for EJ-301 neutron scintillators is displayed in Fig. 3.15.

To validate the theoretical estimates of neutron spectra based on the measured breakup cross sections for the 21MeV proton energy case, a three-step procedure has been employed. Firstly, the CDCC+CRC calculations using FRESCO was used to obtain the theoretical estimates of breakup and double differential cross sections, which were then matched with the experimentally measured cross sections using events in telescopes. Next, the neutron events in 30° and 60°, coincidence with ^{3}He at 55° has been generated through Monte-Carlo approach based on the FRESCO calculated cross sections. This is compared with the experimental neutron spectra gated with ^{3}He events at 55° for the validation of

the theoretical estimates. Similarly, 0° neutron spectrum has also validated for 20 MeV based on the measurement by McNaughton et al. as the current study didn't measured a 0° neutron spectrum. Instead, have utilized the data reported by McNaughton et al., for a thicker Li target. To account for the thick target effect, FRESCO followed by Monte-Carlo calculations for 20MeV, along with SRIM calculations has been performed.

Neutron spectra corresponding to 30° and 60° neutron events, in coincidence with 55° ^{3}He, have been generated through Monte-Carlo approach based on FRESCO calculated cross sections. This spectra have been compared with the experimentally measured neutron spectra, for the validation of the theoretical estimates based on the measured breakup cross sections. Similarly, another set of FRESCO and Monte-Carlo calculation has been performed for 20 MeV proton energy to reproduce the spectrum reported by McNaughton et al., along with SRIM [27] calculations to account the thick target effect. The n_0 and n_1 component to the neutron spectra have been calculated using FRESCO including the ground ($3/2^-$) and 429 keV ($1/2^-$) states. FRESCO calculated cross sections for ground ($3/2^-$) and 429 keV ($1/2^-$) states were validated with TENDL-2019 evaluated cross sections for ^{7}Li(p,n)^{7}Be[28].

The Monte-Carlo based calculation for 0° neutrons has been performed using CDCC-CRC calculated cross section, with parameters obtained through matching the experimentally measured double differential cross sections. The CRC were considered for accounting the resonant breakup contribution. The estimated 0° neutron spectrum, corresponding to the breakup is presented in Fig. 3.16. This shows the contribution from $7/2^-$(4.57 MeV) and $5/2^-$ (6.73 and 7.21 MeV) levels as Gaussian peaks. Due to the overlaps of the continuum levels to the resonant states, the width of the resonant breakup neutron colonies is large.

Validation of theoretically calculated neutron spectra has been performed with experimentally measured $55° - {}^3$He gated neutron spectrum at 30° and 60°. Theoretical spectra for these angles are generated through Monte-Carlo approach

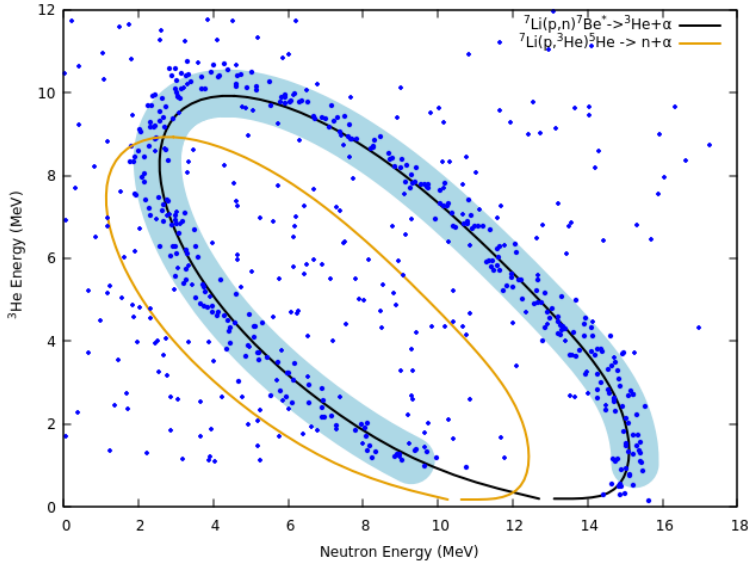

Figure 3.14: Fixed Radius K_{nn} based identification of the neutrons in coincidence with ^{3}He

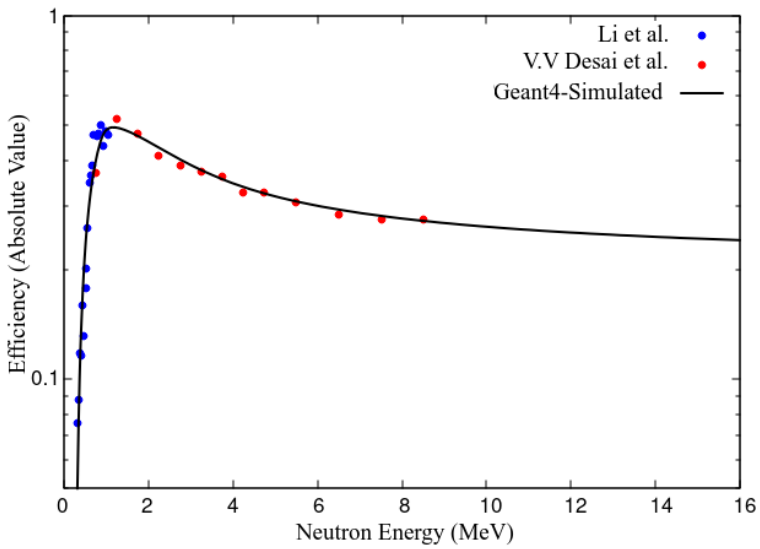

Figure 3.15: Neutron Energy - Efficiency plot for EJ301 Liquid Scintillator

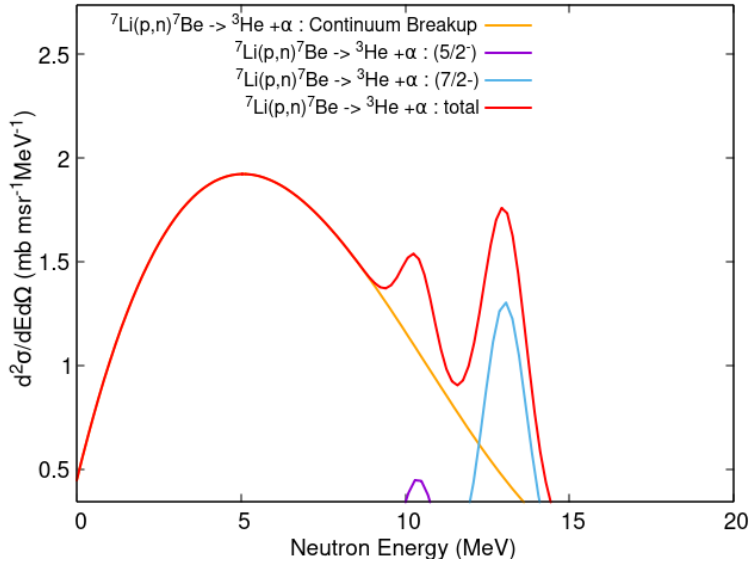

Figure 3.16: The simulated 0° breakup neutron spectrum at 21 MeV, having continuum and resonance contributions

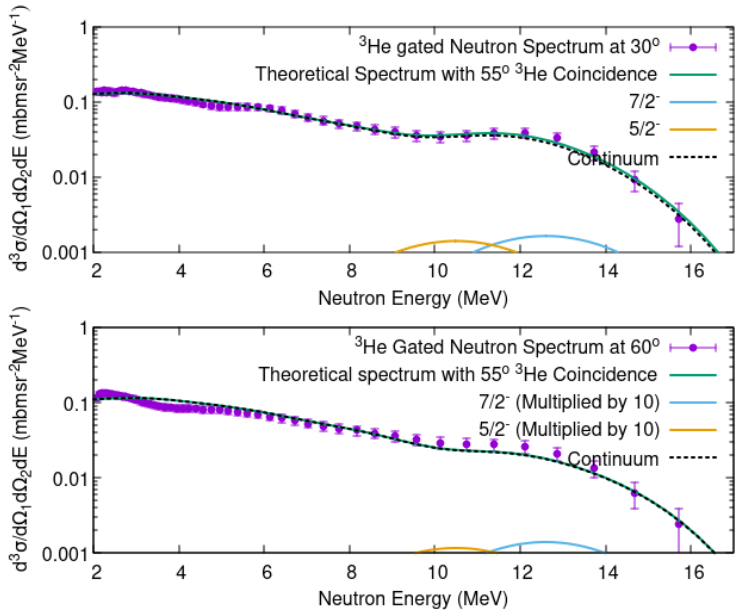

Figure 3.17: The comparison of ^{3}He gated neutron spectra with theoretical spectra

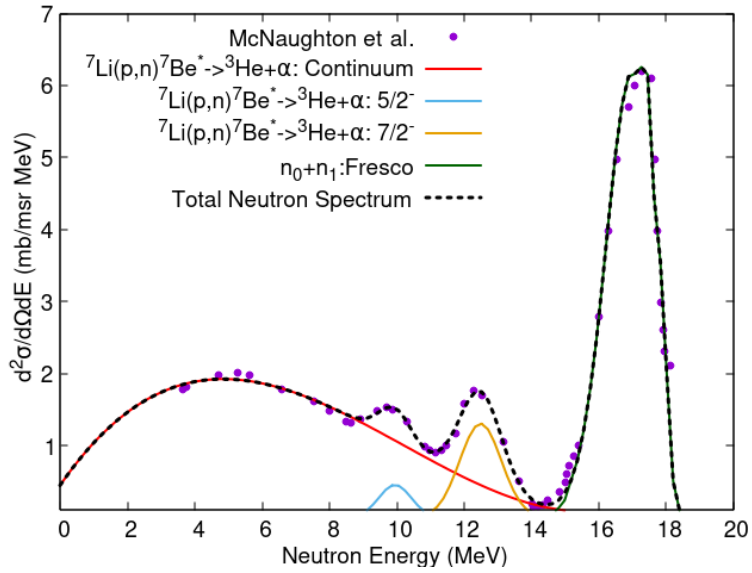

Figure 3.18: Comparison of evaluated neutron spectrum with the spectrum reported by McNaughton et. al. for 20 MeV

over the theoretical cross sections, as described above. The comparison of theoretically evaluated neutron spectrum with $55^\circ - {}^3$He gated neutron spectrum at 30° and 60° is presented in Fig. 3.17. Comparison shows that the theoretically generated neutron spectra are well reproducing the experimental neutron spectrum within the counting statistics of the neutrons per energy bin. However, due to the lesser contribution of the resonant neutrons, with $55^\circ - {}^3$He events, the resonant breakup neutrons from $7/2^-$ and $5/2^-$ states are not well evident in the experimental spectrum.

The comparison of theoretical neutron spectra for 20 MeV of proton energy and the neutron spectra reported by McNaughton et al. is illustrated in Fig. 3.19. This shows the theoretical calculations, with parameters used for reproducing the double differential cross section of ^{7}Li(p,n)^{7}Be$^* \rightarrow n + {}^3$He$+\alpha$ are quite apt for generating the breakup neutron spectrum from p + ^{7}Li system. The n_0 and n_1 neutron colonies are well reproduced by the FRESCO calculations.

Based on the the measurement and analysis of ^{7}Li(p,n)^{7}Be$^* \rightarrow n +^3$ He $+ \alpha$ reaction, reveals the existence of the coupling of resonant and breakup levels of ^{7}Be to the ejectile neutron wave function. The reaction mechanism is considered

as the $p +^7$ Li is populating the ^{7}Be $+ n$ via charge exchange (Meson exchange from proton to neutrons in the bound state) or via two-step DWBA. In the multi-step DWBA, the proton in the initial capture state picks up a neutron from ^{7}Li produces $d +^6$ Li state. From this state, a proton is stripped from deuteron and transfered to ^{6}Li and forms ^{7}Be$+n$ final state. Hence the final cross sections are the sum of cross sections of meson exchange channel and the two-step DWBA transfer channel. The meson exchange channel is not coupled to any resonant states. However the two step DWBA transfer couples to the $^1/2^-$ state of ^{7}Be of the final state, at the second step where the proton stripping from deuteron is being initiated. This coupling adds the resonance at 2.3 MeV in the ^{7}Li(p,n)^{7}Be excitation function.

Once the final state, (^{7}Be $+ n$) is populated through meson exchange or two step DWBA transfer, either to the ground state ($3/2^-$), or to the first excited state ($1/2^-$) at the resonance. From this state, the ejectile neutron wave function couples to the resonant and continuum states, analogous to an inelastic scattering of $n -^7$ Be system. This couplings are well evident in the double differential cross sections of ^{7}Li(p,n)^{7}Be$^* \rightarrow n +^3$ He $+ \alpha$ and exit channel neutron spectrum. The couplings produces individual neutron colonies in the exit channel neutron spectrum. The continuum neutron colony, emerges due to the coupling of continuum levels generated by the α+^{3}He cluster structure to the ^{7}Be+n final state, has been qualitatively measured by the present study. Effect of coupling of α+^{3}He continuum levels makes a neutron distribution from 0 MeV to E_{beam} - Q, where Q is the sum of Q-value for ^{7}Li(p,n) and the breakup threshold of ^{7}Be to α and ^{3}He. Further, at the high energy tail of the breakup continuum, there form two additional peaks, corresponding to the $7/2^-$ and $5/2^-$ resonance levels of ^{7}Be, above the breakup threshold. The overlaps of breakup levels of ^{7}Be produced by ^{3}He $+\alpha$ and ^{6}Li + p structures, above 1.59 and 5.60 MeV, produce broadening of the resonance neutron colonies. However for the practical use, the neutron distribution at the lower energy will be different, due to the presence of satellite neutrons as recommended by Drosg evaluations[5]. The satellite

neutron distributions are formed through multiple scattering of neutrons, which are highly dependent on the experimental setup. However, the present study is concluded without accounting the satellite neutrons, formed at lower energies.

3.5 Summary

The formation of the continuous neutron distribution for ^{7}Li(p,n) reaction at 21 MeV proton energy has been identified as the overlap of continuum levels generated by α+^{3}He clusters of ^{7}Be above breakup threshold. This has been verified by measuring the double differential cross sections for three body breakup at 21 MeV of proton energy. The measured double differential cross sections have been reproduced through FRESCO calculations by adding the coupling of continuum generated by α+^{3}He to the ^{7}Be+n final state. The neutron spectrum has been simulated through Monte-Carlo using FRESCO calculated cross sections. These neutron spectra have been validated using experimentally measured ^{3}He gated spectrum and McNaughton's spectrum reported for 20 MeV.

Bibliography

[1] M.W. McNaughton, N.S.P. King, F.P. Brady, J.L. Romero, and T.S. Subramanian. Measurements of 7li(p,n) and 9be(p,n) cross sections at 15, 20 and 30 mev. *Nuclear Instruments and Methods*, 130(2):555 – 557, 1975.

[2] M. Majerle, P. Bém, J. Novák, E. Šimečková, and M. Štefánik. Au, bi, co and nb cross-section measured by quasimonoenergetic neutrons from p + 7li reaction in the energy range of 18–36 mev. *Nuclear Physics A*, 953:139–157, 2016.

[3] S. G. Mashnik, M. B. Chadwick, P. G. Young, R. E. MacFarlane, and L. S. Waters. ^{7}Li(p,n) nuclear data library for incident proton energies to 150 mev. Technical Report LA-UR-00-1067, Los Alamos National Laboratory, 2000.

[4] J.W Meadows and D.L Smith. Protons from neutron bombardment of nat-

ural lithium. Technical Report ANL-7938, Argone National Laboratory, 1972.

[5] M. Drosg. Sources of variable energy monoenergetic neutrons for fusion-related applications. *Nuclear Science and Engineering*, 106(3):279–295, 1990.

[6] D. Chattopadhyay, S. Santra, A. Pal, A. Kundu, K. Ramachandran, R. Tripathi, T. N. Nag, and S. Kailas. Direct and resonant breakup of radioactive ^{7}Be nuclei produced in the ^{112}Sn(^{6}Li,^{7}Be) reaction. *Phys. Rev. C*, 102:021601, Aug 2020.

[7] N. C. Summers and F. M. Nunes. ^{7}Be breakup on heavy and light targets. *Phys. Rev. C*, 70:011602, Jul 2004.

[8] N. Keeley, K. W. Kemper, and K. Rusek. ^{7}Be versus ^{7}Li : the influence of breakup threshold on the dynamic polarization potential. *Phys. Rev. C*, 66:044605, Oct 2002.

[9] Mazzocco M. et al. Elastic scattering for the ^{8}B and ^{7}Be +^{208} Pb systems at near-coulomb barrier energies. *Phys. Rev. C*, 100:024602, Aug 2019.

[10] Kolata J. J., Guimarães V., and Aguilera E. F. Elastic scattering, fusion, and breakup of light exotic nuclei. *The European Physical Journal A*, 52, 2016.

[11] L. M. Damone et al. ^{7}Be$(n,p)^{7}$Li reaction and the cosmological lithium problem: Measurement of the cross section in a wide energy range at n_tof at cern.

[12] M. Barbagallo et al. ^{7}Be$(n,\alpha)^{4}$He reaction and the cosmological lithium problem: Measurement of the cross section in a wide energy range at n_tof at cern.

[13] A Pakou., O. Sgouros., V. Soukeras, and F Cappuzzello. Global descriptions and decay rates for continuum excitation of weakly bound nuclei. *Eur. Phys. J. A*, 57(1):25, 2021.

[14] S.V Suryanarayana and E.T. Mirgulae et al. data received from s.v suryanarayana, e.t. mirgulae et., al, this data has been reanalysed by our group recently. Private communications,.

[15] R. Gregor Weiß, Benjamin Ries, Shuzhe Wang, and Sereina Riniker. Volume-scaled common nearest neighbor clustering algorithm with free-energy hierarchy. *arXiv, 2009.08757,2020.*

[16] ATLAS Collaboration. Observation of a new particle in the search for the standard model higgs boson with the atlas detector at the lhc. *Physics Letters B*, 716(1):1–29, 2012.

[17] Ian J. Thompson. Coupled reaction channels calculations in nuclear physics. *Computer Physics Reports*, 7(4):167 – 212, 1988.

[18] A. et al Pakou. Probing the cluster structure of ^{7}Li via elastic scattering on protons and deuterons in inverse kinematics.

[19] George Freier, Eugene Lampi, W. Sleator, and J. H. Williams. Angular distribution of 1- to 3.5-mev protons scattered by he^{4}. *Phys. Rev.*, 75:1345–1347, May 1949.

[20] Philip D. Miller and G. C. Phillips. Scattering of protons from helium and level parameters in li^{5}. *Phys. Rev.*, 112:2043–2047, Dec 1958.

[21] J. E. Brolley, T. M. Putnam, L. Rosen, and L. Stewart. Hydrogen-helium isotope elastic scattering processes at intermediate energies. *Phys. Rev.*, 117:1307–1316, Mar 1960.

[22] R. Kankowsky, J.C. Fritz, K. Kilian, A. Neufert, and D. Fick. Elastic scattering of polarized protons on tritons between 4 and 12 mev. *Nuclear Physics A*, 263(1):29 – 46, 1976.

[23] G.R. Satchler, L.W. Owen, A.J. Elwyn, G.L. Morgan, and R.L. Walter. An optical model for the scattering of nucleons from 4he at energies below 20 mev. *Nuclear Physics A*, 112(1):1 – 31, 1968.

[24] M. Drosg, R. Avalos Ortiz, and P. W. Lisowski. Neutron interactions with 3he revisited-i: Elastic scattering around and beyond 10 mev. *Nuclear Science and Engineering*, 172(1):87–101, 2012.

[25] V. Zagrebaev et al. Nuclear reaction video project, 3-body kinematics of nuclear reactions.

[26] V. V. Desai, B. K. Nayak, A. Saxena, S. V. Suryanarayana, and R. Capote. Prompt fission neutron spectra in fast-neutron-induced fission of ^{238}U. *Phys. Rev. C*, 92:014609, Jul 2015.

[27] James F. Ziegler. Srim-2003. *Nuclear Instruments and Methods in Physics Research Section B: Beam Interactions with Materials and Atoms*, 219-220:1027 – 1036, 2004. Proceedings of the Sixteenth International Conference on Ion Beam Analysis.

[28] A.J. Koning, D. Rochman, J.-Ch. Sublet, N. Dzysiuk, M. Fleming, and S. van der Marck. Tendl: Complete nuclear data library for innovative nuclear science and technology. *Nuclear Data Sheets*, 155:1 – 55, 2019. Special Issue on Nuclear Reaction Data.

Chapter 4

Resonant and Breakup Couplings in Direct Capture Reactions

4.1 Introduction

The nuclear reactions are producing the exit channel with wave functions in the form of ejectile and residue in the final state of the nuclear reaction. The residue cross sections are driven by the potentials, couplings and overlaps corresponding to the initial and final states. For the ^{7}Li(p, n) charge exchange reaction, the coupling of ejectile neutron wave function to the continuum and resonant states of the residual ^{7}Be is identified. This problem is treated as a two step, where the charge exchange or two step DWBA coherently populates the ^{7}Be+n final state, and from this step the ejectile neutron wave function couples to the states of ^{7}Be. This mode of the population demands the formation of the residue+ ejectile final state defined with the nuclear potential.

For the neutron capture reactions such as ^{7}Li(n,γ), ^{6}Li(n,γ) etc., the exit channel is having residual nucleus and photon only, which is not capable to produce any kind of nuclear interactions other than electromagnetic couplings. However, the neutron capture reactions also exhibit coupling behavior. This mechanism has been anticipated as a result of the direct capture mechanism, with

the electromagnetic coupling between initial capture state and the final bound state. Considering the residues having breakup threshold lesser than the neutron capture Q-Value, there will be a branching to the breakup states, by the coupling of the breakup states to the initial capture state. This leads to the breakup of residue in the direct or resonant mode. There ^{6}Li(n,γ), ^{7}Li(n,γ) are the reactions convenient to explore about these couplings. In the neutron capture, the $^7\mathrm{Li}+\gamma$ and $^8\mathrm{Li}+\gamma$ final states are being formed corresponding to ^{6}Li(n,γ) and ^{7}Li(n,γ) reactions respectively. Considering the ^{6}Li(n,γ)^{7}Li reaction, the final state is being populated above the $^7\mathrm{Li} \rightarrow \alpha + t$ breakup threshold. However, in ^{7}Li(n,γ), the ^{8}Li is being populated below any breakup thresholds. Hence, the comparison of the excitation functions will produce the information on the impact of breakup coupling in direct capture reactions in the resonant energy ranges.

The ^{6}Li(n,γ) reaction remains not well explored due to its small cross section as well as the lesser natural abundance of ^{6}Li. The ^{6}Li(n,γ)^{7}Li exhibits considerably small cross sections in the order of several μbs, due to the predominance of $\alpha + t$ breakup mode. Thus the ^{6}Li(n,α)^{3}H channel is being prominent. This breakup mode having a threshold of 2.47 MeV, dominates as the Q-value for the neutron capture of ^{6}Li is as high as 7.25 MeV. Due to this higher Q-value, breakup levels populate more than the single particle levels. This suppresses the radiative neutron capture process in ^{6}Li. However, the direct reaction component involving the single particle levels contributes significantly to the radiative neutron capture through Direct Capture (DC) mechanism [1, 2]. The Fig. 4.1 illustrates the mechanism of direct capture in ^{6}Li(n,γ).

There is only a single measurement on energy dependent cross section of ^{6}Li(n,γ) existing in the literature, by Ohsaki et al., for the neutron energy range of 20 to 80 keV[3]. The other measurements available as exfor entries [4], by R. B Firestone et al. [5], Chang Su Park et al. [6] and G.A Batholomew et al. [7] are the Maxwellian averaged cross sections for thermal reactor neutron spectrum. Further, there are evaluations existing for ^{6}Li(n,γ) in ENDF/B-VIII.0 [8], JEEF [9] and JENDL[10] basic evaluated nuclear data libraries. They are the de-

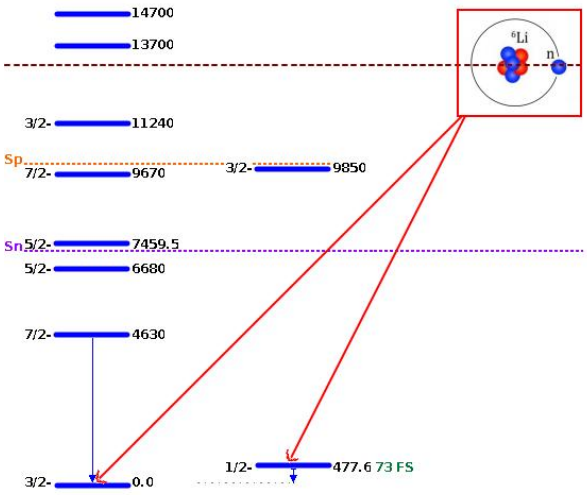

Figure 4.1: Direct Neutron Capture mechanism in ^{6}Li(n,γ) reaction

rived data sets estimated by fitting the R-Matrix formalism on ^{6}Li(n,t)^{4}He cross sections[8]. Due to the limitations with the ^{6}Li target and lower cross sections, the direct measurement of ^{6}Li(n,γ) is potentially challenging. Hence a novel experimental methodology has been implemented by utilizing the properties of the Direct Capture formalism for the measurement of ^{6}Li(n,γ). The measurement of ^{6}Li(n,γ) cross sections has been attempted through this method, by populating the initial neutron capture states by inelastic scattering of protons on ^{7}Li. The γ transitions from the ^{7}Li initial state to bound states of ^{7}Li are measured by generating $p - \gamma$ coincidences. The capture cross sections were determined through the approach of Direct Capture mechanism, reformulated for the experimental implementation. The current experiment is having resemblances with the established Oslo method[11, 12]. In this study, only a single large volume $LaBr_3$ scintillator was used instead of γ calorimeter. This measurement has been successful because all the γ events from the initial neutron capture states are well resolvable and γ multiplicity is near to unity.

There are a few measurements on ^{7}Li(n,γ) cross-sections, which give the radiative neutron capture of ^{7}Li in the range of few microbarns(μb), for the astrophysical energies of interest. One of the important measurements is by J.C. Black-

mon. et al., [13] reported the neutron capture cross-sections from 1.78 eV to 1.9 keV, measured through time of flight tagged neutrons. Imhof et al.[14] measured cross-sections in the range of 50 keV to 1 MeV with the quasi-monoenergetic neutrons using ^{7}Li(p,n) as the neutron source. These experiments report ^{7}Li(n,γ) cross-sections in the order of μb. The excitation function in this range is rapidly falling with energy. Since the cross-sections are low enough, the measurement in keV neutron energy is potentially challenging to build enough statistics. There was an attempt by R. Izsak et al. to estimate the ^{7}Li(n,γ) cross-section through Coulomb dissociation of ^{8}Li [15]. However, it couldn't measure resonances in the ^{7}Li(n,γ) excitation function. Hence to attempt the energy region covering the resonance in ^{7}Li(n,γ), a neutron time of light technique was employed.

The comparison of ^{6}Li(n,γ) and ^{7}Li(n,γ) excitation functions give the information on the coupling of the residual states in the capture reactions on the basis of the hypothesis that the resonant states above breakup threshold will not decay through the electromagnetic transition route, if their decay widths are very large. Based on this it is anticipated to observe the resonant enhancement in ^{7}Li(n,γ) corresponding to 3^{+} and 1^{+} states of ^{8}Li and the resonant contributions will be absent corresponding to the $5/2^{-}$, $7/2^{-}$ and $3/2^{-}$ levels. And the CRC and CDCC-CRC theoretical calculations, based on couplings and overlaps, reveals the nature of breakup couplings and its influence on the radiative capture.

4.2 Materials and Methods

4.2.1 Measurement of ^{6}Li(n,γ) Cross Sections

Methodology

The direct capture model (DC) is well established for explaining the radiative captures at lower energies, and neutron capture reactions for light elements, where the compound nuclear level density models are insufficient to explain the radiative capture[2]. The DC accounts for the capture cross section as the sum of direct capture to the discrete states and the single particle continuum states.

The Direct Capture formalism is expressed in its own form based on Ref. [1] and Ref. [2],

$$\sigma^{DC}(E) = \sum_{f=0}^{f_{max}} S_f \sigma_f^{dis}(E) + \langle S \rangle \int_{E_0}^{E_n} \rho(E_f, J_f, \pi_f) \sigma_f^{con}(E_f) dE_f \tag{4.1}$$

The first part in Eq. 1, $\sum_{f=0}^{f_{max}} S_f \sigma_f^{dis}(E_f)$ corresponds to the direct capture to the discrete resonant states defined as f. S_f is the spectroscopic amplitude corresponding to each resonant state. Second part, $\langle S \rangle \int_{E_0}^{E_n} \rho(E_f, J_f, \pi_f) \sigma_f^{con}(E_f) dE_f$ corresponds the capture to the single particle continuum states. The $\langle S \rangle$ is the average spectroscopic amplitude of the continuum states distributed from the continuum formation threshold E_0 to the neutron separation energy E_n. $\rho(E_f, J_f, \pi_f)$ is the single particle level densities corresponding to each E_f, which are also a function of the spin and parity of the state. The $\sigma_f^{con}(E_f)$ stands for the capture corresponding to the each of f states in the continuum having energy E, which is assumed to be discretized in an interval dE_f. The $\sigma_f^{con}(E_f)$ can be expressed, based on the electric and magnetic modes of transition, as

$$\begin{aligned} \sigma_f^{con}(E_f) =& \frac{2J_f + 1}{Ek(2J_A + 1)(2J_n + 1)} \\ & \times \sum_{I_f, J_i, l_i, I_i} \left[C_1 k_\gamma^3 (|M_{E1}|^2 + |M_{M1}|^2) + C_2 k_\gamma^5 |M_{E2}|^2 \right] \end{aligned} \tag{4.2}$$

Here J_f is the spin of the final state after capture followed by the electromagnetic transition, J_A is the spin of the target nuclei and J_n is the spin of neutron. E and k are respectively energy and wave number of neutrons corresponding to J_i. C_1 and C_2 are the normalization constants corresponding to dipole and quadrupole transitions. M_{E1}, M_{M1} are the electric and magnetic dipole matrix elements and M_{E2} is the matrix element corresponding to electric quadrupole transition. k_γ stands for the wave number of the emitted photon.

The neutron capture in ^{6}Li populates initial capture state with an excitation energy of 7.25 MeV + E$_n(\frac{A}{A+1})$. This energy is well above the $^7\text{Li} \rightarrow \alpha + t$ breakup threshold of 2.47 MeV. However, the transition from J_i to the $\alpha + t$

breakup continuum levels will not contribute to the radiative capture process. The population of breakup states results to the continuum breakup of ^{7}Li. Hence, the $3/2^-$ and $1/2^-$ states corresponding to ground and 477 keV are the only J_f states involving the radiative capture. The present formulation assumes that the $3/2^-$ and $1/2^-$ states are also a part of the single particle continuum states. However, for these states, the $\rho(E_f, J_f, \pi_f)$ term generates the definite shape of the resonance. This assumption is taken for modifying Eqn. 4.1 to a single integral ranging from 0 to E_n. Hence the reformulated form can be expressed as,

$$\begin{aligned}\sigma^{DC}(E) = \frac{(2J_f+1)}{Ek(2J_A+1)(2J_n+1)} \int_0^{E_n} \rho(E_f, J_f, \pi_f) \\ \times \sum C_1 k_\gamma^3 (|M_{E1}|^2 + |M_{M1}|^2) + C_2 k_\gamma^5 |M_{E2}|^2 dE_f\end{aligned} \tag{4.3}$$

In the following part of the thesis, $\frac{(2J_f+1)}{Ek(2J_A+1)(2J_n+1)}$ is expressed as g_j, the spin factor, and $\int_{E_x}^{E_{max}} \rho(E_f, J_f, \pi_f)$
$\times \sum C_1 k_\gamma^3 (|M_{E1}|^2 + |M_{M1}|^2) + C_2 k_\gamma^5 |M_{E2}|^2 dE_f$ as $\Gamma(E_x)$, gamma strength term.

The gamma rays produced from each excitation energy, equivalent to the excitation energy of the neutron capture, having a capture γ distribution depend on the transitions to J_f states. The integral of this distribution is considered as $\Gamma(E_x)$, which has been measured in the current experiment. The events populating resonant and direct breakup levels, during the collective excitation, are not producing any gamma rays. Thus the γ spectra produced in inelastic excitation of ^{7}Li are purely from the transition of the J_i states to the bound states. Thus in the current study, $\Gamma(E_x)$ is measured for the equivalent neutron energies using inelastic scattering of protons on Li target. The g_i has been calculated theoretically for obtaining the cross sections.

The initial capture state of ^{6}Li(n,γ) reaction has been populated using ^{7}Li$(p, p'\gamma)$ reaction. This populates ^{6}Li+n states in the continuum region, with the spin states analogous to the $l = 0$ interaction for neutrons. The γs produced from the inelastic state is being utilized to measure the $\Gamma(E_x)$.

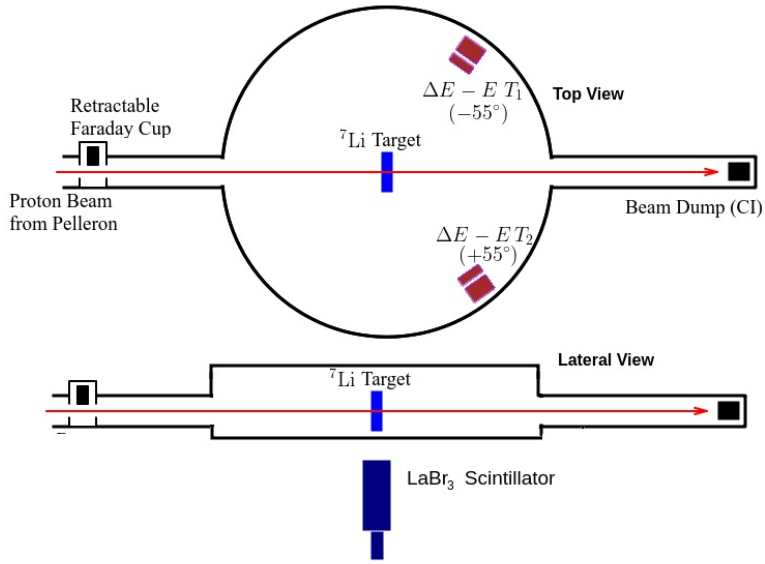

Figure 4.2: Illustration of experimental setup in top and lateral views

Experimental Details

The experiment is performed using 16 MeV proton beam from BARC-TIFR Pelletron facility, Mumbai, India. A ^{nat}Li target of 1.4 mg/cm^2 was used for the experiment. The experimental setup has been illustrated in Fig. 4.2. Two silicon detector telescopes having 25μm and 1500μm ΔE-E pairs, were mounted at $+55°$ $-55°$ at a distance of 7.5cm from the target to record the inelastically scattered protons. A 3$''$ diameter and 7$''$ length LaBr$_3$ scintillator, coupled to a fast photomultiplier tube, was placed at 90°, at the bottom side of the target. This was used for measuring the γ spectra. The distance between the target and LaBr$_3$ detector was 12 cm. The LaBr$_3$ is calibrated using 1.21 MeV, 1.15 MeV and 936 MeV γs from the inelastic scattering of protons on ^{197}Au target.

The inelastically scattered protons were identified from the E-ΔE correlation plot by proper gating. The γ events in the LaBr$_3$ scintillator, with the elastically scattered protons are identified. The events were converted to the excitation energy of ^{7}Li from the energy of elastically scattered protons, using two body kinematics. A correlation matrix between γ energy (E$_\gamma$) and excitation energy of ^{7}Li (E$_x$) was constructed. This matrix was unfolded to original γ matrix using

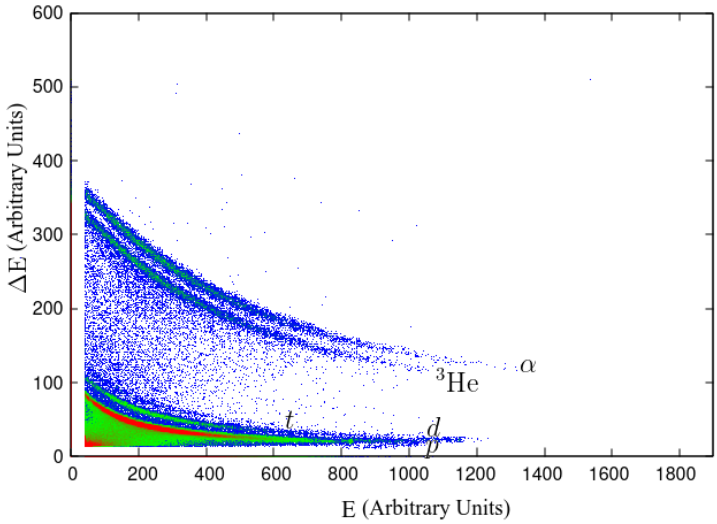

Figure 4.3: The typical $E - \Delta E$ Correlation plot recorded in the telescope

response matrix for the current $LaBr_3$ detector. The unfolding procedure was done using in-house developed machine learning assisted unfolding algorithm by preserving the excitation energy information of the events[16]. The obtained E-ΔE correlation plot is presented in Fig. 4.3. The measured correlation, simulated response matrix for the detector and unfolded E_γ-E_x matrix are shown in Fig. 4.4 and Fig. 4.5.

The unfolded γ matrix has been appropriately gated for the excitation energy and projected to the γ spectrum. The unfolded matrix is shown in Fig. 4.6 and the projection of the gated region is illustrated in Fig. 4.7. The spectrum holds three colonies of gammas, evident in all excitation energies. Discrete γ colonies are corresponding to the electromagnetic transitions from J_i state with energy E_x to the $3/2^-(g.s), 1/2^-(477keV)$ states below $\alpha + t$ breakup threshold. The continuum γ colony is identified as emerging due to the coupling of $7/2^-, 5/2^-$ and $3/2^-$ resonant levels, above neutron separation threshold of ^{7}Li, to the electromagnetic transitions to the $3/2^-(g.s)$ or $1/2^-(477keV)$ states. These states are also overlapped by the $\alpha + t$ breakup continuum, results a higher decay width. The inelastic scattering populates the collective levels than the single particle levels in nuclei. In the case of ^{7}Li, there are $\alpha + t$ breakup continuum present in

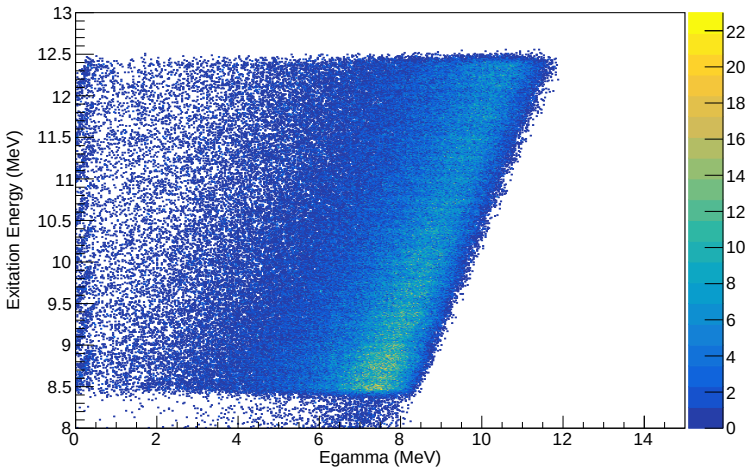

Figure 4.4: The obtained E_γ-E_x correlation

the region of the collective levels. The population of the breakup levels seldom contributes to the γ production, as they end up with the breakup (the inelastic breakups). Hence the γ events observed in coincidence with the inelastically scattered protons can be assured as originated by the transition from initial capture state to the bound states.

The total counts in the γ colonies are retrieved and normalized with the inelastically scattered protons corresponding to the each excitation energy bin. The normalized γ yield is corrected for the solid angle between the $LaBr_3$ scintillator and the target. The attenuation in the bottom lid of the scattering chamber is also accounted based on Geant4 simulation [17]. The intrinsic efficiency of the detector has already been applied through the response matrix during the unfolding process. This corrected normalized yield is the measure of $\Gamma(E_x)$ in the Direct Capture Formalism. The spin factor, g_i, is calculated using the direct capture calculation module incorporated in Talys-1.95. This provides an accurate estimation of the wave number, k. Optical potential for n+^{6}Li is taken from S. Chiba et al [18] for the calculation of the spin factor. The $^6Li(n,\gamma)$ cross sections were then deduced as $g_i\Gamma(E_\gamma)$.

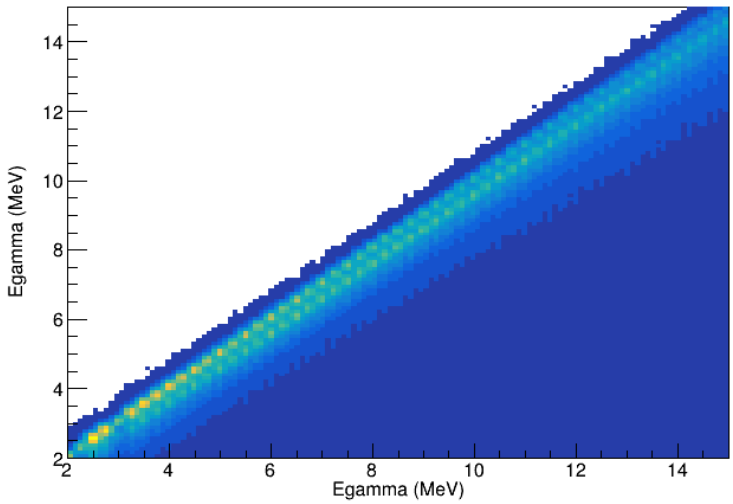

Figure 4.5: Geant4 simulated response matrix for $LaBr_3$ scintillation detector

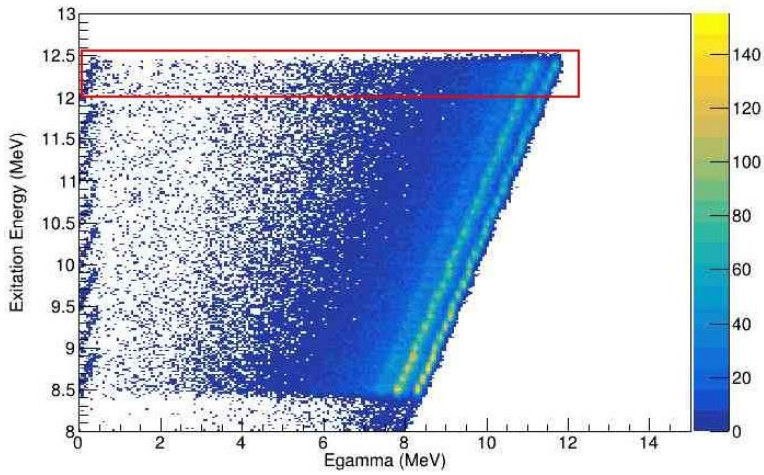

Figure 4.6: The unfolded E_γ-E_x correlation matrix with the gate defined for 12.375 MeV excitation

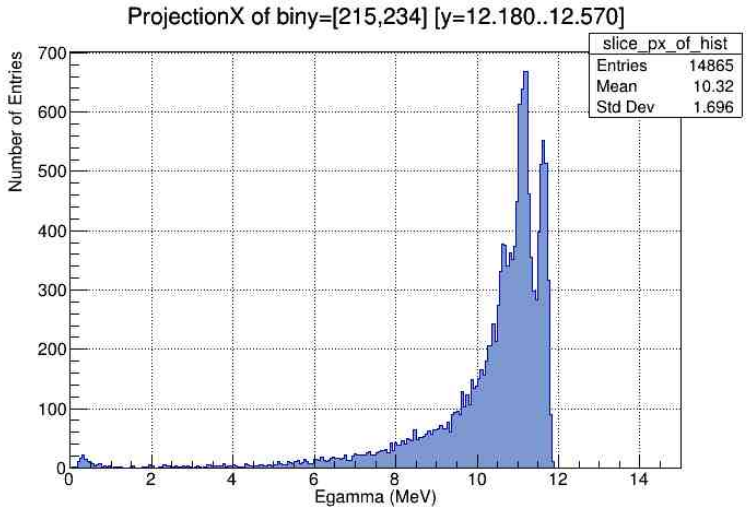

Figure 4.7: Projection of the gate defined for 12.375 MeV excitation showing the γ spectrum from the 12.375 MeV initial capture state

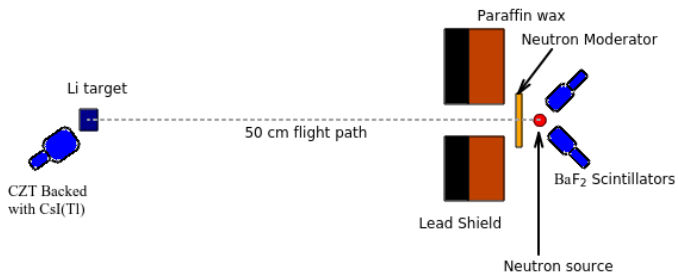

Figure 4.8: Schematic of the Neutron Time of Flight setup

4.2.2 Measurement of ^{7}Li(n,γ)

Experimental Setup

The $^{7}\mathrm{Li}(n,\gamma)^{8}Li$ cross-section measurement was performed with TOF tagged neutrons. Neutrons from a 10 Ci sealed Am-Be source were utilized for the measurement. The source emits $\approx 2\times 10^{7}$ neutrons/sec in the 4π geometry. They are moderated by a 1cm thick paraffin wax to increase the population of neutrons in the 1 keV to 1 MeV region. The neutrons were tagged by detecting 4.4 MeV γs corresponding to the excitation of ^{12}C in the $^{9}\mathrm{Be}(\alpha,n)^{12}\mathrm{C}$ reaction, with two 3-inch thick BaF_2 scintillator coupled to a fast PMT. This covers 40% of the solid angle of the Am-Be source.

A 1×1×1 inch Cadmium Zinc Telluride (CZT) detector was kept in 60°, at a distance of 5 cm, to the collimated neutron path for recording the neutron capture γ rays. A time of flight was generated between the BaF_2 signal and the timing signal of CZT. Four sides of CZT were backed with 1×1×1 inch CsI(Tl) scintillators with PIN readout. CsI crystals detect the Compton scattered photons leaving from CZT. These CsI(Tl) signals were add-backed to the CZT energy output to increase the photo-peak efficiency. However, the time output has been selected from CZT alone. The typical experimental setup is illustrated in Fig. 4.8.

The intrinsic efficiency of the CZT detector, backed with CsI, has been generated with the standard ^{133}Ba, ^{137}Cs,^{60}Co and ^{22}Na sources. The geometry dependent detector efficiencies have been estimated from the Geant4 simulation[17] of the detector and sample geometry, with accounting for the attenuation corrections for the sample. The time to amplitude converter (TAC) has been calibrated using a standard time calibrator.

Target Design

Since the lithium is prone to oxidation on exposure to air, air-tightly sealed in the aluminium container under argon environment was used. A 100 grams of

natural lithium, in the geometry of $10\times10\times2$ cm^3, was used for the experiment. This geometry and sample quantity has provided an event rate of $3-4$ events per hour per energy bin. The boric acid target of the same geometry was used as the boron target for the normalization reaction.

Data Analysis

The measurement was performed uninterrupted for a duration of 744 hours (31 days). The background was estimated through a run for 24 hours without the target. The ToF-E$_\gamma$ correlations gated with 4.4 MeV γ from the Am-Be source were generated, and the γ bands corresponding to ^{8}Li excitation levels were identified. The measured ToF-E$_\gamma$ correlation is plotted in Fig. 4.9. These bands were banana gated and projected to the TOF axis. The projected histograms were re-binned into a lower ADC resolution to achieve sufficient statistics. This is further converted into energy, based on the time calibration. The counts in each energy bin have been converted to yields by accounting for the detector efficiencies and γ branching ratios. This is further normalized to the 4.4 MeV γ counts in the BaF$_2$ detector.

$^{10}B(n,\alpha)^7Li^*$ has been used as the monitor reaction for cross section normalization. 25 grams of boron granules, sealed in the same geometry mentioned above was placed. The 477 keV γ band was projected to the energy axis and normalized by 4.4 MeV γ events as mentioned above. The ^{7}Li(n,γ) cross sections were estimated as,

$$\sigma_{^7\mathrm{Li}(n,\gamma)}(E) = \frac{Y_{^7\mathrm{Li}}(E)}{Y_{^{10}\mathrm{B}}(E)}\sigma_{^{10}\mathrm{B}(n,\alpha)}(E) \tag{4.4}$$

where, $Y_{^7Li}(E)$ is the yield of neutron capture γ from ^{7}Li(n,γ) reaction per energy bin, normalized with 4.4 MeV γ from Am-Be source. Similarly $Y_{^{10}B}(E)$ is the yield for 477 keV γs from ^{10}B$(n,\alpha)^7$Li* per energy bin normalized to 4.4 MeV γs. $\sigma_{^{10}\mathrm{B}(n,\alpha)}(E)$ is the reaction cross-section for ^{10}B$(n,\alpha)^7$Li*. The monitor, ^{10}B$(n,\alpha)^7$Li* reaction cross sections were chosen from IRDFF-II evaluations[19].

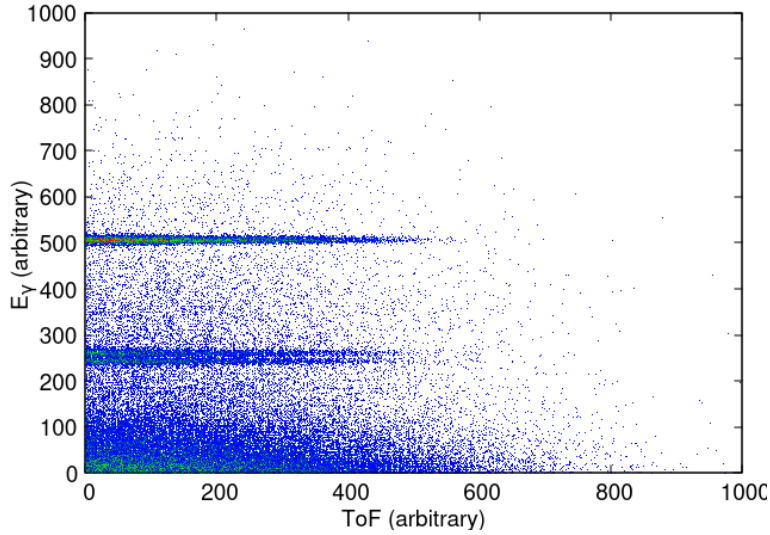

Figure 4.9: The correlation plot between neutron Time of flight and E_γ recorded in the CZT detector

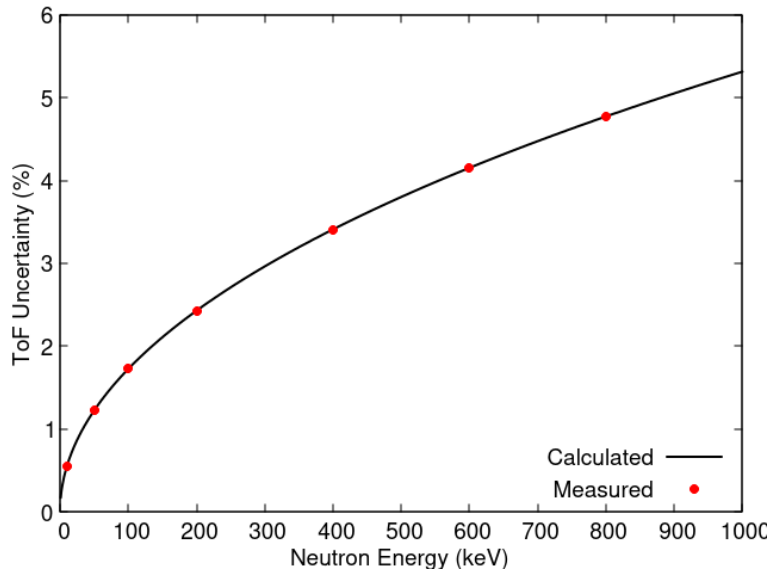

Figure 4.10: Resolution Function for current Time of Flight setup

The uncertainties corresponding to each bin has been estimated through propagating the partial uncertainties in counts, efficiency and monitor data. Energy binning is performed considering the bin width be more than the time of flight uncertainty. The measured cross-sections were compared with the previous measurements and theoretical estimates.

Resolution Function

Resolution function for the current time of flight setup has been estimated by determining the time uncertainties produced by the start detector (ΔT_{D1}), the stop detector (ΔT_{D2}) and by the time to amplitude converter (ΔT_{TAC}). This has been estimated by utilizing the 511 keV γ pairs produced through pair annihilation from ^{22}Na source and CZT was placed at the target position. For this purpose, the neutron source was replaced by the ^{22}Na source. One of the 511 keV γ detected in the BaF_2 starts the TAC and the other photon corresponds to the same pair, detected in CZT, stops the TAC. The FWHM of the TOF peak defines the time uncertainty. To get the uncertainties in neutron flight time range, an electronic delay is added to the stop signal. The time uncertainties corresponding to different neutron energies were measured by varying the electronic delay. This is further converted to energy uncertainty by accounting the TOF conditions. The estimated response function is illustrated in Fig. 4.10.

4.3 Theoretical Calculations

Theoretical calculations are performed to reproduce the direct capture cross sections of ^{6}Li(n,γ) and ^{7}Li(n,γ). A coupled channel method has been adopted for the calculation. n+^{6}Li is taken as the entrance channel mass partition and ^{7}Li+γ partition in the exit channel. The n+^{6}Li potentials by Chiba et al.[18] was used for the calculations. The calculations were performed using FRESCO coupled channel code [20]. The problem is defined as to calculate the direct radiative transitions from J_i to $3/2^-$ (g) and $1/2^-$ (477 keV) levels. The levels above neutron separation energy is considered as coupled to the $3/2^-$ and $1/2^-$ levels. Further, the overlap of $\alpha + t$ on the resonant states above the breakup

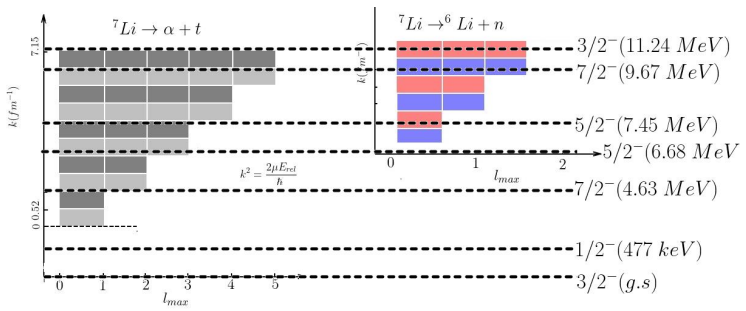

Figure 4.11: Resonant and Continuum Discretized levels of ^{7}Li

threshold has been considered. The breakup continuum is discretized with $\alpha + t$ relative energy bin of 0.5 MeV, and the spin is calculated as the sum of spin of t and the relative angular momentum of the bin. The CDCC bins and CRC states of ^{7}Li is illustrated in Fig. 4.11. Theoretical spectroscopic factor for ^{6}Li+n from the shell model calculations by Cohen and Kurath have been used for the resonant states[21]. An optimized average spectroscopic factor of 0.75 was used for $\alpha + t$. The FRESCO calculation has been limited to E_1 and M_1 mode of γ transitions and higher multipolarities have been neglected. A separate Monte-Carlo calculation, based on the FRESCO calculated cross sections, has been performed to reproduce the experimentally measured γ spectra.

Similar calculations has been performed for ^{7}Li(n,γ), with ^{7}Li+n as the entrance channel mass partition and ^{8}Li+γ in the exit channel. There is no breakup mode is present in the ^{8}Li residue like ^{7}Li. Hence the calculation has been fulfilled with CRC states. Hence the ground state (2^+), 980 keV (1^+), 2.25 MeV (3^+) and 3.2 MeV (1^+) states are being considered as CRC states. The coupling from ^{7}Li+n to these states are being defined with spectroscopy factors 0.75, 0.8 and 0.8 corresponding to these states. The calculation is performed for the energy range of 1 keV to 1 MeV.

Along with the FRESCO calculations, statistical Direct Capture calculations were performed using Talys-1.95 nuclear reaction code [22]. This is to account for the compound nuclear, pre-equilibrium and the continuum component of the direct capture mechanism. The Microscopic level densities (temperature depen-

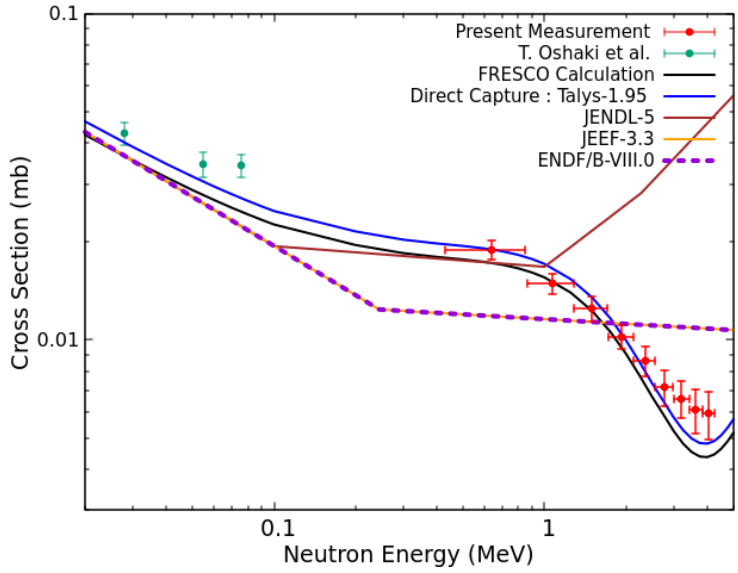

Figure 4.12: Measured ^{6}Li(n,γ) cross sections compared with Direct Capture Model Calculations in FRESCO, Talys-1.95, and the evaluations by ENDF/B-VIII.0, JEEF-3.3 and JENDL-5 libraries

dent HFB, Gogny force) from Hilaire's combinatorial tables were used for the calculations of compound nuclear contribution as well as the continuum component of direct capture[23]. The predictions by Talys calculations were also compared with experimental results.

4.4 Results and Discussion

4.4.1 ^{6}Li(n,γ)

The measured cross sections for ^{6}Li(n,γ) are illustrated as locally averaged histogram values in Fig. 4.12, along with the measurement by T. Oshaki et al., for comparison. Theoretical calculations using FRESCO and Talys-1.95 are also presented in Fig 4.12. Present measurement of cross sections for ^{6}Li(n,γ) is limited to the Direct Capture, and the compound nuclear contributions. Due to the limitations in the methodology, preequilibrium contribution is not addressed in the experiment. Measured cross sections are in the μb range and cover, for the first time, energies of 0.6 to 4 MeV as compared to measurements of Oshaki et al. which are in the range of 30 to 70 keV energy region.

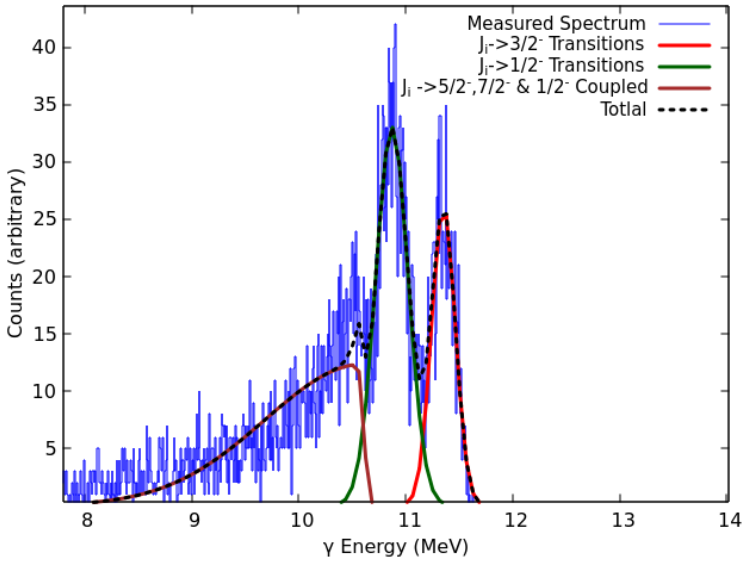

Figure 4.13: Measured γ spectrum at 11.5 MeV excitation energy along with the calculated spectrum

The FRESCO calculated discrete component of the Direct Capture is illustrated as the black solid line in Fig.4.12. The calculations reproduce the experimental cross sections within the error bars, for the spectroscopic factors by Kohan and Kurath. This indicates that the major contribution of the ^{6}Li(n,γ) is from the discrete component of the direct neutron capture. Further, there exists a strong coupling of $5/2^-$, $7/2^-$ and $3/2^-$ levels, which lies above the neutron separation threshold of ^{7}Li, on $J_i \rightarrow 3/2^-$ and $\mathrm{J}_i \rightarrow 1/2^-$ transitions. These resonant states are overlapping with the $\alpha + t$ breakup continuum and indicates a larger energy width. This coupling effect is emerged as the low energy tail along with γ colonies, corresponding to $J_i \rightarrow 3/2^-$ and $\mathrm{J}_i \rightarrow 1/2^-$ transitions, in the experimental γ spectrum. The experimental γ spectrum has been well reproduced using the Monte-Carlo simulation based on the FRESCO calculation and is presented in Fig. 4.13. This assures the validity of couplings considered for the calculation of discrete components of the direct capture in ^{6}Li(n,γ) reaction.

Talys-1.95 calculated continuum component of Direct Capture, Hauser-Feshback + Pre-equilibrium components are much lesser compared to the discrete component of the direct capture. Talys calculated discrete component of Direct

Capture in ^{6}Li(n,γ) is also well in agreement with the experimental cross sections and FRESCO calculations. The inhibition of the compound nuclear component in ^{6}Li(n,γ) reaction is due to the lesser number of levels available in the ^{7}Li compound nucleus. Further the strong coupling of $\alpha + t$ breakup is also reducing the capture cross section significantly. The contributions of E1, M1 and E2 mode of γ transitions to the total direct capture are presented in Fig. 4.15. Compared to the E1 mode of transition, the M1 and E2 transition yields are much lower and not contributing significantly to the total radiative capture. The sum of Direct Capture, Hauser-Feshback and Pre-equilibrium is well reproducing the experimental cross sections for ^{6}Li(n,γ). The Direct Capture, Hauser-Feshback and Pre-equilibrium components of neutron capture along with experimental cross sections are illustrated in Fig. 4.14.

Excitation functions available with ENDF/B-VIII.0, JEEF-3.2 and JENDL-5 are compared with the experimental cross sections and theoretical predictions. The comparison is presented in Fig 4.12. ENDF/B-VIII.0 and JEEF-3.2 cross sections are identical and not reproducing the theoretical or experimental cross sections above 0.1 MeV. At lower energies, below 0.1 MeV, all the evaluations are matching with the discrete component of the direct capture. But at energies above 0.1 MeV, there is a huge discrepancy between ENDF/B-VIII.0,JEEF-3.2 and JENDL-5. The JENDL-5 is highly over predicts the experimental data. Further, the shape of the excitation function differ significantly from the measured and calculated curves. ^{6}Li(n,γ) evaluated data in ENDF/B are obtained by fitting the R-Matrix on the ^{6}Li(n,α), the breakup channel. Hence it is anticipated as this fitting may be inappropriate for accurate parametrization of the direct capture.

4.4.2 ^{7}Li(n,γ)

Cross-section data for ^{7}Li(n,γ)^{8}Li, measured in the current study, are illustrated in the form of locally averaged histogram values in Fig. 4.16. The present measurement provides a clear identification of the non-resonant continuum for

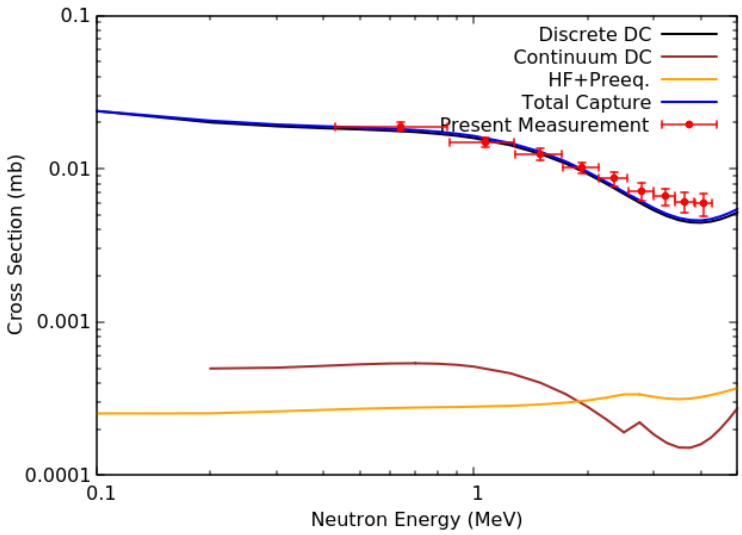

Figure 4.14: Discrete and Continuum components of direct capture and the Hauser-Feshbach- + pre-equilibrium component (HF+Preeq) with the the total cross section compared with the experimental data

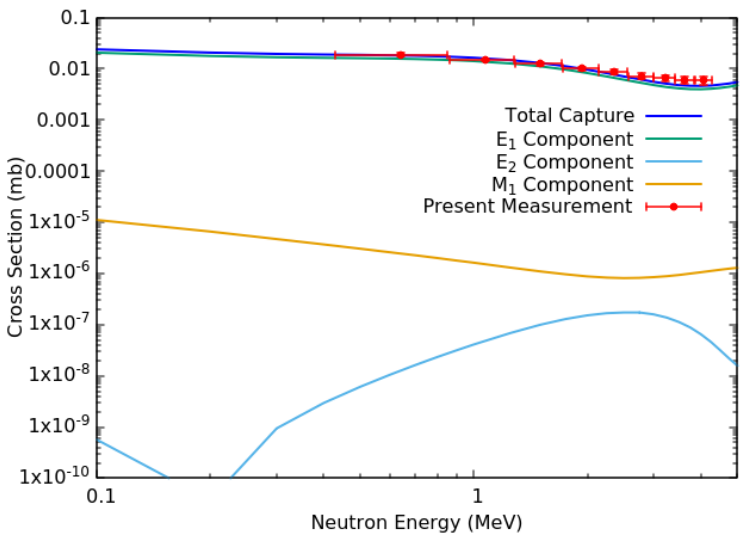

Figure 4.15: Contribution of E_1, E_2 and M_1 modes of electromagnetic transition to the total capture cross section.

the range of 10 to 1000 keV. The contribution corresponding to 3^+ resonance state of ^{8}Li at 2.255 MeV excitation energy is also clearly identified. The continuum and resonant cross-sections are in the range of microbarns(μb). Even though the cross-sections are small, the measurement is fulfilled with a statistical uncertainty of around 3%. For comparison, previous measurements by Imhof et al., Iszak et al., are also included in Fig 4.16. Comparisons show that all the data sets are in good agreement in the non-resonant region, with the measurement by Imhof et al., is showing comparatively higher statistical uncertainty. Additionally, the measurement by Imhof et al. is showing a higher resonance width compared to the present study. The centroid shift by few tens of keVs and asymmetry exhibited by the resonance contribution in the measurement by Imhof et al. is anticipated mainly due to the higher width of the quasi monoenergetic neutrons and lesser counting statistics. The excitation function measured by Iszak et al. is limited to the non-resonant component due to the limitation of the Coulomb dissociation technique employed.

Theoretical analysis with potential model calculations for ^{7}Li(n,γ)^{8}Li is shown in Fig. 4.17 along with present measurement, measurement by Imhof et al.[14], and by Iszak et al.[15]. The potential model predictions are also limited to the non-resonant continuum region of the excitation function. The calculations by different approaches reproduce the experimental data with 10% accuracy. Among these, the potential model approach by P. Descouvemont, incorporated in Nuclear Reaction Video Project (NRV), shows an under-prediction by an average of 10% from the experimental data, for a calculation with a spectroscopic amplitude of 0.95. It is illustrated as the orange curve in Fig. 4.17. The model calculation by Rupak and Higha[24], shown as the blue curve, is very well reproducing the current experimental results as well as the measurement by Iszak et al. above 3^+ resonance, the data are in agreement with Imhof et al., and deviate as the energy comes below the resonance. The model calculation by Wang et al.[25], illustrated as green line, is well reproducing the experimental data below the 3^+ resonance. This is underestimating for energies above the resonance peak. Sim-

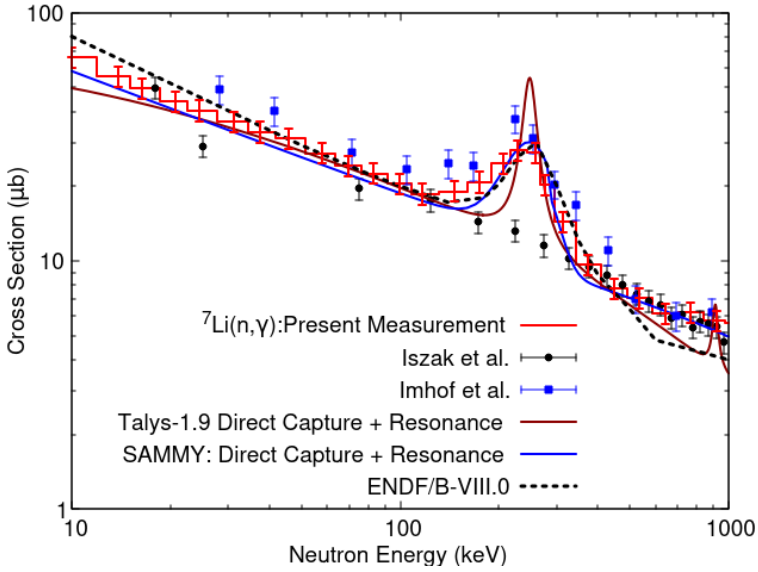

Figure 4.16: The $^{7}\mathrm{Li}(n,\gamma)^{8}Li$ cross sections compared with Talys-1.9 Direct Capture Model code predictions with resonances from default Talys library, R-Matrix fitting provided by SAMMY and the ENDF/B-VIII.0 Predictions .

ilarly, the calculation by Huang et al. [26] is well reproducing the measurement by Imhof et al. It is illustrated as a brown curve in Fig. 4.17

The experimental cross-sections along with the statistical model, ENDF/B-VIII.0 predictions and SAMMY R-matrix fit are presented in Fig. 4.16. The statistical model calculation with the direct capture model in Talys-1.9, modified with single-particle level densities, is well reproducing the non-resonant continuum of the experimental data with a spectroscopic amplitude of 0.675. However, the resonance contribution at 3^{+} state is not well reproduced with the default resonance parametrisation in Talys-1.9. The resonance width is underestimated. This is presented as a brown curve. The SAMMY R-matrix fit with continuum part of excitation function through direct capture approach and resonance region through Reich-Moore resonance parametrisation is well reproducing the experimental cross-sections. It is illustrated as a blue curve in Fig. 4.16. Additionally, for the sake of comparison, the ENDF/B-VIII.0[8] evaluations for $^{7}\mathrm{Li}(\mathrm{n},\gamma)^{8}\mathrm{Li}$ excitation function are also included as the black dashed curve. It is also reproducing the resonant and continuum regions of the experimental cross sections. The present measurement generates cross-sections as locally averaged histogram

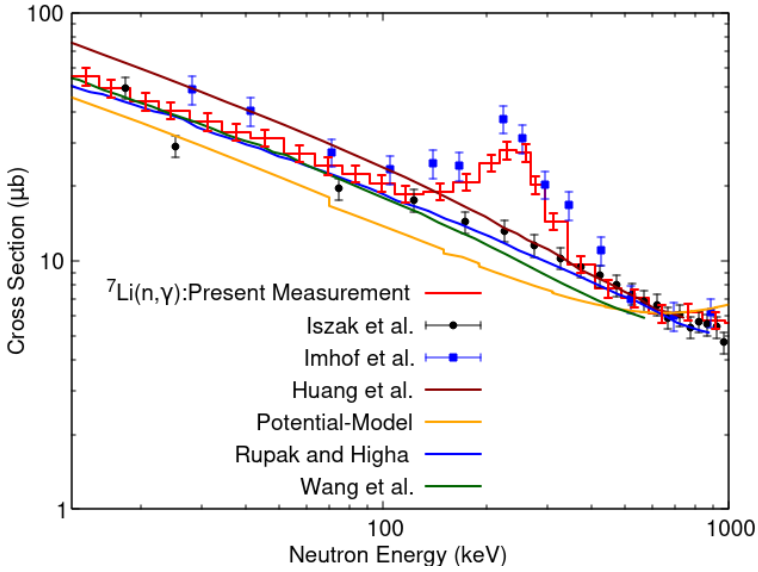

Figure 4.17: The ^{7}Li$(n,\gamma)^{8}Li$ cross sections compared with potential model calculations

values. The energy resolution of the present measurement is much lesser than in the dedicated high resolution neutron time of flight facilities such as CERN n_ToF, GELINA etc. However, the current measurement provides a resolution better than the measurements with quasi-monoenergetic neutrons.

Compared to the Direct Capture model (Potential Model), the Modified Direct Capture model is more accurately reproducing the experimental cross-sections, even when the potentials used are kept the same. This may be due to the formation of the n+^{7}Li continuum and the single-particle levels approach not being able to account for the levels. The Modified Direct Capture Model uses the single-particle level densities, which will be more closer to the n+^{7}Li continuum (through statistical approach). Hence the Modified Direct Capture Model is better reproducing the experimental cross-sections than the conventional Direct Capture approach [27].

^{6}Li(n,γ) cross sections are evident in the range of few μb due to the strong coupling of ^{6}Li(n,α). It is identified with CDCC-CRC calculation that the n+^{6}Li wave function in the initial capture state is coupling to the $\alpha + t$ breakup states and results in the alpha emission. Hence the ^{6}Li(n,α) cross sections are high,

in several barns, compared to the ^{6}Li(n,γ) in μb range. The ^{6}Li(n,γ) excitation function not showing any prominent resonance effects corresponding to $5/2^-, 7/2^-$ and $3/2^-$ levels, due to the strong spectroscopic overlap between these resonant states and $\alpha + t$ breakup continuum. However these effect is evident in the ejectile γ spectrum of neutron capture. And the spectrum has been theoretically reproduced through FRESCO calculations with the couplings and overlaps. Based on CDCC-CRC analysis, it is cleared that the radiative transitions are branching to the resonant states, however it is not contributing to the radiative capture due to the overlap of breakup states. Thus the populated excited state is leading to the breakup of the residue. These effects are identified in the γ spectrum measured.

Considering ^{7}Li(n,γ), the resonance contribution corresponding to the 3^+ state (2.25 MeV) is well prominent, centered at 223 keV, in (n, γ) excitation function. This is due to the coupling of 3^+ state of ^{8}Li to the ^{7}Li+n initial capture state. Due to the prominence of the unbounded neutron continuum overlaps to this state, shows an higher width for the resonance. The excitation function with labeling the resonant states are illustrated in Fig. 4.18.

From the CDCC-CRC analysis of the ^{6}Li(n,γ) and ^{7}Li(n,γ) reactions, is identified that the both channels are undergoing same reaction mechanism of direct capture. And the couplings from initial capture state to the final state are similar, is through the electromagnetic. The difference existing is only in the range of final state, where in ^{6}Li(n,γ)^{7}Li, the residual breakup states are overlapped with CRC states as ^{7}Li(n,γ)^{8}Li is free from those couplings. Hence the excitation functions can be compared to explore the impact of residual breakup couplings. The comparison shows an enhancement of the ^{7}Li(n,γ) cross sections corresponding to the 3^+ (2.25 MeV) state. This mainly contributing through E_1 transitions. In ^{6}Li(n,γ), the states other than the 477keV bound state of ^{7}Li ($1/2^-$), the higher states, $5/2^-, 7/2^-$ and $3/2^-$ are also couples to the initial capture state. However a fall in the excitation function, corresponding to theses states, has been observed in the case of ^{6}Li(n,γ). Due to the strong overlap of $\alpha+t$ breakup states

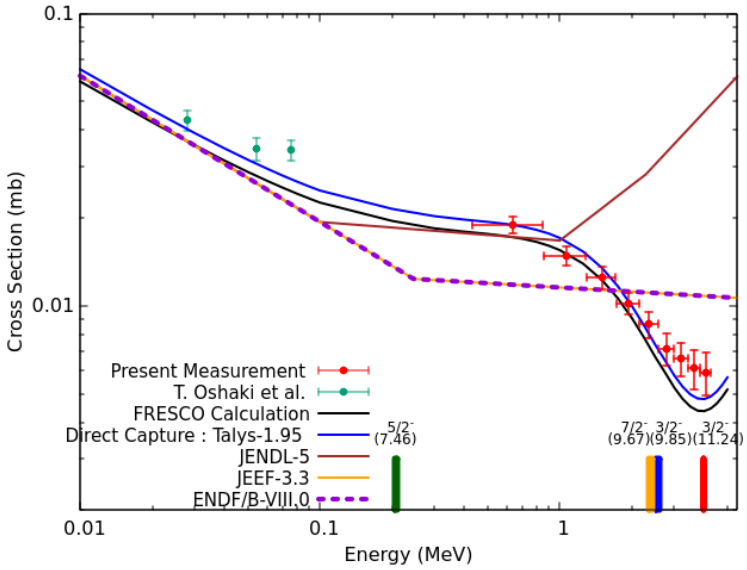

Figure 4.18: ^{6}Li(n,γ) Excitation function with marking for energies corresponding resonant state of ^{7}Li

on $5/2^-, 7/2^-$ and $3/2^-$, the population of these states lead to the breakup and thereby the residue are not populated.

The overlap of breakup continuum is limited to the resonant $5/2^-, 7/2^-$ and $3/2^-$ levels. The radiative capture mode is unaffected by the breakup continuum as there is no direct transitions from initial capture state to breakup states. However, the overlap of the breakup continuum on the resonant states produces higher energy uncertainty. This makes the γ spectrum by the direct capture to $5/2^-, 7/2^-$ and $3/2^-$ states broader compared to the γs corresponding to the direct capture to ground ($3/2^-$) and 477 keV excitation $1/2^-$ states.

4.5 Summary

The ^{6}Li(n,γ) cross sections have been deduced by measuring the γ transition probability experimentally and by accounting for the spin factor by theoretical calculation. The initial neutron capture states have been populated through the inelastic scattering of protons in ^{7}Li. The method is analogous to the established Oslo method used to measure the neutron capture. However, this current measurement is fulfilled with a single $LaBr_3$ scintillator, than the total absorption

spectrometers (γ calorimeters). This is because of the average multiplicity of the γ events from J_i states covered in this study, are near to unity and the primary γ events were well resolved. The accessibility of this method to the direct capture mechanism is assured by comparing the measured γ spectrum to the calculated γ spectrum. This shows that the major mechanism involved in ^{6}Li(n,γ) is the discrete component of Direct Capture with E1 mode of transition. Continuum component of Direct Capture and HF+Prequilibrium are significantly smaller compared to the discrete component. E2 and M1 components are significantly lesser compared to the E1 mode of transition. The calculations indicate there exist a significant coupling of the $5/2^-, 7/2^-$ and $3/2^-$ levels, above neutron separation threshold of ^{7}Li, to the $J_i \rightarrow 3/2^-$ and $J_i \rightarrow 1/2^-$ transitions in ^{6}Li(n,γ) reaction.

The ^{7}Li(n,γ) cross sections were measured with ^{241}Am-^{9}Be based neutron time of flight setup. These cross sections were reproduced with potential model calculations as well as the direct capture model calculations. The coupling of 1^+ state of ^{8}Li to the direct capture has been identified in the FRESCO calculation. On comparison between the excitation functions of ^{6}Li(n,γ) and ^{7}Li(n,γ), the direct transitions are allowed from the ^{6}Li+n initial capture state to the ground and $^1/2^-$ state at 477 keV. Along with this the other unbound resonant states also couples to this resulting a resonant breakup of the ^{7}Li residue. ^{7}Li(n,γ), the 1^+ state is coupling to the excitation function resulting a resonant enhancement, as the 1^+ resonant state in ^{8}Li is a bounded one. Where as the coupling of the $5/2^-, 7/2^-$ and $3/2^-$ levels produces a dip in the excitation function of ^{7}Li(n,γ). Summarizing, it can be concluded from the analysis that the direct capture is the electromagnetic coupling between initial capture state and the final resonant states of the residue, and the coupling of individual resonant states are responsible for the formation of the resonant states. If the residual states are bounded, the resonant coupling enhances the residual population and the unbound resonances (which are overlapped with breakups) results to the reduction (destruction) in the residue population.

Bibliography

[1] Yi Xu and Stephane Goriely. Systematic study of direct neutron capture. *Phys. Rev. C*, 86:045801, Oct 2012.

[2] Y. Xu, S. Goriely, A. J. Koning, and S. Hilaire. Systematic study of neutron capture including the compound, pre-equilibrium, and direct mechanisms. *Phys. Rev. C*, 90:024604, Aug 2014.

[3] Toshiro Ohsaki, Kenji Takaoka, Yasuki Nagai, Hideo Kitazawa, and Masayuki Igashira. First measurement of neutron capture cross section of 6li at stellar energy. *AIP Conference Proceedings*, 529(1):678–680, 2000.

[4] N. Otuka, E. Dupont, V. Semkova, B. Pritychenko, A.I. Blokhin, M. Aikawa, S. Babykina, M. Bossant, G. Chen, S. Dunaeva, R.A. Forrest, T. Fukahori, N. Furutachi, S. Ganesan, Z. Ge, O.O. Gritzay, M. Herman, S. Hlavač, K. Katō, B. Lalremruata, Y.O. Lee, A. Makinaga, K. Matsumoto, M. Mikhaylyukova, G. Pikulina, V.G. Pronyaev, A. Saxena, O. Schwerer, S.P. Simakov, N. Soppera, R. Suzuki, S. Takács, X. Tao, S. Taova, F. Tárkányi, V.V. Varlamov, J. Wang, S.C. Yang, V. Zerkin, and Y. Zhuang. Towards a more complete and accurate experimental nuclear reaction data library (exfor): International collaboration between nuclear reaction data centres (nrdc). *Nuclear Data Sheets*, 120:272–276, 2014.

[5] R. B. Firestone and Zs. Revay. Thermal neutron radiative cross sections for ^{6,7}Li, ^{9}Be, ^{10,11}B, ^{12,13}C, and ^{14,15}N. *Phys. Rev. C*, 93:054306, May 2016.

[6] Chang Su Park, Gwang Min Sun, and H.D. Choi. Determination of thermal neutron radiative capture cross section of 6li. *Nuclear Instruments and Methods in Physics Research Section B: Beam Interactions with Materials and Atoms*, 245(2):367–370, 2006.

[7] G. A. Bartholomew and P. J. Campion. Neutron capture gamma rays from

lithium, boron, and nitrogen. *Canadian Journal of Physics*, 35(12):1347–1360, 1957.

[8] D.A. Brown and et al. Endf/b-viii.0: The 8th major release of the nuclear reaction data library with cielo-project cross sections, new standards and thermal scattering data. *Nuclear Data Sheets*, 148:1–142, 2018. Special Issue on Nuclear Reaction Data.

[9] A. J. M. Plompen, O. Cabellos, C. De Saint Jean, M. Fleming, A. Algora, M. Angelone, P. Archier, E. Bauge, O. Bersillon, A. Blokhin, F. Cantargi, A. Chebboubi, C. Diez, H. Duarte, E. Dupont, J. Dyrda, B. Erasmus, L. Fiorito, U. Fischer, D. Flammini, D. Foligno, M. R. Gilbert, J. R. Granada, W. Haeck, F.-J. Hambsch, P. Helgesson, S. Hilaire, I. Hill, M. Hursin, R. Ichou, R. Jacqmin, B. Jansky, C. Jouanne, M. A. Kellett, D. H. Kim, H. I. Kim, I. Kodeli, A. J. Koning, A. Yu. Konobeyev, S. Kopecky, B. Kos, A. Krása, L. C. Leal, N. Leclaire, P. Leconte, Y. O. Lee, H. Leeb, O. Litaize, M. Majerle, J. I. Márquez Damián, F. Michel-Sendis, R. W. Mills, B. Morillon, G. Noguère, M. Pecchia, S. Pelloni, P. Pereslavtsev, R. J. Perry, D. Rochman, A. Röhrmoser, P. Romain, P. Romojaro, D. Roubtsov, P. Sauvan, P. Schillebeeckx, K. H. Schmidt, S. Serot, O.and Simakov, I. Sirakov, H. Sjöstrand, A. Stankovskiy, J. C. Sublet, P. Tamagno, A. Trkov, S. van der Marck, F. Álvarez Velarde, R. Villari, T. C. Ware, K. Yokoyama, and G. Žerovnik. The joint evaluated fission and fusion nuclear data library, jeff-3.3. *The European Physical Journal A*, 56(181), 2020.

[10] Keiichi SHIBATA, Osamu IWAMOTO, Tsuneo NAKAGAWA, Nobuyuki IWAMOTO, Akira ICHIHARA, Satoshi KUNIEDA, Satoshi CHIBA, Kazuyoshi FURUTAKA, Naohiko OTUKA, Takaaki OHSAWA, Toru MURATA, Hiroyuki MATSUNOBU, Atsushi ZUKERAN, So KAMADA, and Jun ichi KATAKURA. Jendl-4.0: A new library for nuclear science and engineering. *Journal of Nuclear Science and Technology*, 48(1):1–30, 2011.

[11] M Guttormsen, T.S Tveter, L Bergholt, F Ingebretsen, and J Rekstad. The unfolding of continuum γ-ray spectra. *Nuclear Instruments and Methods in Physics Research Section A: Accelerators, Spectrometers, Detectors and Associated Equipment*, 374(3):371–376, 1996.

[12] A Schiller, L Bergholt, M Guttormsen, E Melby, J Rekstad, and S Siem. Extraction of level density and γ strength function from primary γ spectra. *Nuclear Instruments and Methods in Physics Research Section A: Accelerators, Spectrometers, Detectors and Associated Equipment*, 447(3):498–511, 2000.

[13] J. C. Blackmon, A. E. Champagne, J. K. Dickens, J. A. Harvey, M. A. Hofstee, S. Kopecky, D. C. Larson, D. C. Powell, S. Raman, and M. S. Smith. Measurement of ^{7}Li(n,γ_0)^{8}li cross sections at e_n=1.5–1340 ev. *Phys. Rev. C*, 54:383–388, Jul 1996.

[14] W. L. Imhof, R. G. Johnson, F. J. Vaughn, and M. Walt. Cross sections for the li$^7(n,\gamma)$li^8 reaction. *Phys. Rev.*, 114:1037–1039, May 1959.

[15] R. Izsák et al. Determining the ^{7}li(n,γ) cross section via coulomb dissociation of ^{8}li. *Phys. Rev. C*, 88:065808, Dec 2013.

[16] CV Midhun, M.M Musthafa, Antony Joseph, Jagadeesan K.C, and S. Ganesan. Extraction of neutron pulses from coincidence summed events via machine learning - like algorithm. *Proceedings of the DAE International Symp. on Nucl. Phys.*, 63:1134–1135, 2018.

[17] S. Agostinelli. Geant4—a simulation toolkit. *Nuclear Instruments and Methods in Physics Research Section A: Accelerators, Spectrometers, Detectors and Associated Equipment*, 506(3):250–303, 2003.

[18] S. Chiba, K. Togasaki, M. Ibaraki, M. Baba, S. Matsuyama, N. Hirakawa, K. Shibata, O. Iwamoto, A. J. Koning, G. M. Hale, and M. B. Chadwick.

Measurement and theoretical analysis of neutron elastic scattering and inelastic reactions leading to a three-body final state for ^{6}Li at 10 to 20 mev. *Phys. Rev. C*, 58:2205–2216, Oct 1998.

[19] A. Trkov, P.J. Griffin, S.P. Simakov, L.R. Greenwood, K.I. Zolotarev, R. Capote, D.L. Aldama, V. Chechev, C. Destouches, A.C. Kahler, C. Konno, M. Koštál, M. Majerle, E. Malambu, M. Ohta, V.G. Pronyaev, V. Radulović, S. Sato, M. Schulc, E. Šimečková, I. Vavtar, J. Wagemans, M. White, and H. Yashima. Irdff-ii: A new neutron metrology library. *Nuclear Data Sheets*, 163:1–108, 2020.

[20] Ian J. Thompson. Coupled reaction channels calculations in nuclear physics. *Computer Physics Reports*, 7(4):167–212, 1988.

[21] S. Cohen and D. Kurath. Spectroscopic factors for the 1p shell. *Nuclear Physics A*, 101(1):1–16, 1967.

[22] A. Koning, S. Hilaire, and M. Duijvestijn. Talys-1.95, a nuclear reaction program. *NRG-1755 ZG Petten, The Netherlands*, 2019.

[23] S. Hilaire, M. Girod, S. Goriely, and A. J. Koning. Temperature-dependent combinatorial level densities with the d1m gogny force. *Phys. Rev. C*, 86:064317, Dec 2012.

[24] Gautam Rupak and Renato Higa. Model-independent calculation of radiative neutron capture on lithium-7. *Phys. Rev. Lett.*, 106:222501, May 2011.

[25] Chengbin Wang, Ousmane I. Cissé, and Daniel Baye. Parametrization of low-energy cross sections for nonresonant neutron capture. *Phys. Rev. C*, 80:034611, Sep 2009.

[26] J.T. Huang, C.A. Bertulani, and V. Guimarães. Radiative capture of nucleons at astrophysical energies with single-particle states. *Atomic Data and Nuclear Data Tables*, 96(6):824–847, 2010.

[27] Radiative capture within potential model, nuclear reaction video project. http://nrv.jinr.ru/nrv/webnrv/r_capture.

Chapter 5

Conclusion and Future Outlook

5.1 Introduction

Nuclear reactions are considered as interactions between projectile and target wave functions within the entrance channel, driven by the potential for the corresponding combination. In the exit channel, the projectile and residue exhibit similar behavior driven by the potential for ejectile-residue mass partitions. As the projectile interacts with the target, it becomes captured, forming an initial capture state based on the impact parameter and relative energy. Depending on the interaction potential, this initial capture state separates into the original target + ejectile wave functions (mass partitions), a phenomenon known as elastic scattering. The undecayed flux in the initial capture state couples to the final state through spin transfer, electromagnetic forces, single-particle excitation couplings, transfer couplings, and more. The produced residue + ejectile mass partitions further interact with the corresponding potential for mass partitions, decaying into residue and ejectile wave functions. Moving to the final state, inelastic couplings with resonant states or the breakup continuum are initiated, leading to further modifications of the wave function.

Based on this concept, direct reactions have been addressed by dividing the reaction stages into entrance and exit channels. In the entrance channel, the projectile and target combination are treated as scattering states. Furthermore,

in the exit channel, the scattering states of reaction residue + ejectile are considered. Adequate couplings between entrance and exit channel states have been taken into account. For multiple residue states, coherent couplings have been established from the initial capture state in the entrance channel to each state in the exit channel in order to derive the cross sections.

5.2 The ^{7}Li(p,n) reactions

The ^{7}Li(p,n) reaction represents a unique kind of reaction where ejectile neutrons are produced via charge exchange or double step transfers. This leads to the generation of quasi-monoenergetic neutrons, although this behavior diminishes when coupling to the ^{7}Be states becomes prominent. Beyond the $^7\mathrm{Be} \rightarrow ^3\mathrm{He} + \alpha$ breakup threshold, a continuum state arises from the relative motion of the ^{3}He and α fragments, resulting in couplings that induce further modifications in the ejectile neutron wave function. This issue arises because the breakup states are sequentially formed in the exit channel. After populating the ^{7}Be+n mass partitions, neutron interaction with the ^{7}Be leads to the formation of breakup states in the final state.

The population cross sections of the breakup continuum have been measured using the $^7\mathrm{Li}(p,n)^7\mathrm{Be}* \rightarrow n + ^3\mathrm{He} + \alpha$ reaction at 21 MeV. This was achieved by coincidentally detecting ^{3}He and alpha fragments. Events were isolated using a kinematic filter gate created through a deep learning method assisted by nearest neighborhood clustering. Each continuum energy bin was examined by measuring ^{3}He and alpha fragments in coincidence and aligning their total energy with the breakup energy. To achieve this, a specially designed target with a thickness of 20 μg/cm^2 was employed to minimize energy loss and fragment straggling within the target.

The measured cross section from each breakup state was reproduced by treating the breakup continuum as multiple discrete scattering states in the exit channel. The population of the breakup continuum was assumed to occur through spin transfer coupling of the ejectile neutron wave function to the ^{7}Be's breakup

states. The breakup continuum was discretized based on angular momentum, with spin of each state derived by propagating the angular momentum of the state and the spin of the fragment. Breakup states were defined using the 3He-alpha potential. The interactions of individual fragments with neutrons were defined with n$-^3$He and n-alpha potentials. Resonance states were considered as CRC states, overlapped with the $^3\mathrm{He} - \alpha$ continuum. Experimental cross sections were successfully replicated using CDCC-CRC calculations. This analysis effectively reproduced the breakup cross sections. To understand the coupling's origin, the spectroscopy factors for $n -^3$ He, $n - \alpha$, and the CDCC-CRC states were systematically varied. While changes in the spectroscopy factors for $n -^3$He and $n - \alpha$ had minimal impact on the cross sections, variations in the CDCC-CRC state coupling showed significant effects. This suggests that as the proton approaches the ^{7}Li target, it forms an initial capture state driven by the effective potential between the proton and ^{7}Li. From this point, the $^7\mathrm{Be} + n$ final state is populated through charge exchange or multi-step transfer channels. This final state can either be the ground state or any CRC state of ^{7}Be. The neutron wave function couples to the CDCC states through a spin transfer-type interaction from this final state. This interaction populates the continuum states in the exit channel. This description is validated by reproducing both the continuum and resonant components of the breakup cross sections, along with the ejectile neutron spectrum. It illustrates the resonant states are being directly populated through the coupling from initial capture state to the final state and the populatin of the breakup continuum is through the interaction of ejectile neutron wave function to the ^{7}Be residue.

5.3 Impact of breakup coupling in radiative capture

Radiative captures in light elements can also be approached in a similar manner. In this scenario, a neutron approaches the residue, leading to an initial capture state bound by the potential corresponding to the system. The decay of this

initial scattering state is referred to as elastic scattering, while the undecayed flux that electromagnetically couples to the final state is known as radiative capture. The final state can be likened to the scattering state of residual nuclei with photons, driven by the pseudo electromagnetic potential for photons.

Since light nuclei possess only single-particle resonant states, electromagnetic couplings will populate these discrete states, referred to as direct capture. The primary question at hand pertains to the overlap of the breakup continuum with the resonant states. It remains unclear whether the initial capture state can be directly coupled to the breakup states of the residue. To address this issue, two radiative capture reactions have been considered: one involving the presence of residual breakup, and the other free from residual breakup.

Cross sections for the $^{7}\mathrm{Li}(n,\gamma)^{8}\mathrm{Li}$ reaction are measured within the neutron energy range of 10 keV to 1 MeV. These measurements utilize time-of-flight tagged neutrons generated from an Am-Be source. To establish a baseline, the $^{10}\mathrm{B}(n,\alpha)^{7}\mathrm{Li}*$ reaction is employed as a normalizing reference. Within this study, both the non-resonant and 3^{+} resonant contributions to the excitation function are identified. The non-resonant continuum and the resonant component are both replicated through Direct Capture calculations. Additionally, the 3^{+} resonant state is accurately reproduced through electromagnetic coupling and the overlap of $n +^{7}$ Li, based on spectroscopy factors for the 1p shells.

The reaction $^{6}\mathrm{Li}(n,\gamma)$ is a typical example where the capture Q-value exceeds the threshold for residual breakup ($^{7}\mathrm{Li} \rightarrow \alpha + t$). The ^{7}Li residue is composed of unbound resonant states, including $7/2^{-}, 5/2^{-}$ and $3/2^{-}$ states, due to the overlap of the $^{7}\mathrm{Li} \rightarrow \alpha + t$ breakup continuum. It is expected that coupling involving spin transfer populates the breakup continuum. However, electromagnetic coupling either to the ground state or to the resonant states leads to radiative capture. Furthermore, the populated resonances induce a spin transfer interaction with the breakup continuum states, resulting in the breakup of the residue. In the case of $^{7}\mathrm{Li}(n,\gamma)$, where the population of the ^{8}Li residue occurs, this process is independent of these types of breakups. Instead, the residue is populated

through electromagnetic couplings. Therefore, comparing the excitation functions of ^{6}Li(n,γ) and 7Li(n,γ) reveals valuable information about the coupling of resonant states and the impact of overlap with the breakup continuum in light elements.

The cross sections for the ^{6}Li$(n,\gamma)^7$Li reaction, covering the neutron energy range of 0.6 to 4 MeV, were determined through the direct capture formalism. This approach involved experimental measurement of the γ transition probability, with consideration of the spin factor handled through theoretical calculations. To gauge the electromagnetic transition probabilities from 7Li*, mirroring the initial neutron capture states of ^{6}Li+n, the J^π states of ^{7}Li were populated via the ^{7}Li$(p,p')^7$Li$*$ reaction. The excitation function was then replicated using FRESCO calculations, incorporating electromagnetic coupling from the initial capture state to the final resonant states. The discretized $^7\text{Li} \rightarrow \alpha + t$ breakup continuum was defined and accounted for as overlaps onto the resonant states. Despite the calculation effectively reproducing the experimental cross sections, no resonant enhancements were observed. However, electromagnetic couplings from the initial capture states to the unbound resonant states were noted in the capture γ spectrum. Notably, corresponding enhancements in the excitation function were not observed. This suggests that capture into the unbound states leads to a breakup without triggering a subsequent gamma cascade.

The comparison between the excitation functions of the ^{6}Li(n,γ) and 7Li(n,γ) reactions provides valuable insights into the underlying dynamics. It becomes evident that direct capture arises from the electromagnetic coupling between the wave function of the initial capture state and the wave function of the resonant state. Notably, no direct branching towards the breakup states is observed within this process. However, a noteworthy phenomenon emerges as unbound resonant states are populated through electromagnetic coupling. These states possess the potential to trigger a breakup mechanism that diverges from the conventional gamma cascade process. This unique pathway involves a spin transfer-type interaction. For this to occur, an essential requirement is that the

breakup continuum must overlap with the resonant states. In situations where no such overlap exists between the breakup states and the resonant states, the system undergoes de-excitation via gamma cascades. This phenomenon contributes significantly to the resonant structure observed within the excitation function. The presence of resonant enhancements in the excitation function can be attributed to the interplay between the electromagnetic coupling, unbound resonant states, and the intricate interplay between the breakup continuum and resonant states. These findings deepen our understanding of the complex interactions that govern the behavior of nuclear reactions in this energy range.

5.4 Summary

The study delves into the effects of residual breakup couplings within charge exchange reactions and radiative captures. To explore this, exclusive cross sections of ^{7}Be $\rightarrow^3$ He + α reactions were experimentally measured, employing coincidence measurements of ^{3}He and α particles. The experiment meticulously measured cross sections corresponding to each partition of the discretized breakup continuum, which were then compared to CDCC-CRC calculations to achieve theoretical reproduction. Estimation of spectroscopy factors for both continuum and resonant states was executed through replicating the experimental cross sections. The intricate process of ^{7}Be residue breakup was identified as a sequential event. This sequence entails the coupling of the ejected neutron wave function to the ^{7}Be breakup states, inducing a transfer of spin. Consequently, this leads to a modification of the neutron wave function, fostering the formation of a continuum along with resonant contributions. The validity of this scenario was confirmed by successfully replicating the neutron spectrum of the exit channel.

Extending this framework to radiative captures where residual breakup is prominent, the reactions ^{6}Li(n,γ) and ^{7}Li(n,γ) were analyzed. In the case of ^{6}Li(n,γ), the indirect measurement approach was adopted through the implementation of the direct capture formalism, while ^{7}Li(n,γ) was measured utilizing neutron time of flight. Notably, the ^{7}Li(n,γ) excitation function highlighted the

presence of a 3^+ resonant contribution, whereas such contribution remained absent in the ^{6}Li(n,γ) reaction. However, intriguingly, the coupling of unbound resonant states was observed in the prompt gamma spectrum arising from neutron capture in ^{6}Li. The utilization of Direct Capture calculations allowed for the reproduction of the ^{6}Li(n,γ) and ^{7}Li(n,γ) reactions. Through analysis, it became evident that the ^{7}Li residue in the ^{6}Li(n,γ) reaction underwent sequential breakup via a spin transfer-type interaction, leading to the inhibition of resonant contributions within the excitation function.

5.5 Future Outlook

The present investigation unveils the process of continuum neutron colony formation within the ^{7}Li(p,n) reaction, attributed to the sequential breakup of ^{7}Be. This process is initiated by spin transfer couplings between the ejectile and residue wave functions. In this reaction, the final state is populated through both charge exchange and multistep transfer reactions. However, the specific contributions of these channels and the spin states populated by each channel remain unidentified. Gaining this insight is crucial to achieving a comprehensive comprehension of the ^{7}Li(p,n) reaction.

To accomplish this, a comprehensive measurement of double differential cross sections for neutrons across all angles is imperative. This measurement necessitates the utilization of pulsed protons of specific energies and an array of charged particle detectors with particle discrimination thresholds below 500 keV. Additionally, the study requires the execution of inelastic breakup studies of the ^{7}Be+n system through exclusive three-body coincidence measurements. This three-body coincidence setup enables the determination of the relative energy-Q value distribution, enabling the direct measurement of individual resonant states and direct breakup events.

By effectively merging the charge exchange and two-step DWBA channels and accurately reproducing the angular distribution of distinct states, it becomes possible to derive valuable insights about the angular distribution. This compre-

hensive approach enhances the depth of comprehension regarding the intricate processes occurring within the ^{7}Li(p,n) reaction. This illumination extends to the continuum neutron colony formation and the underlying mechanisms governing it. Nevertheless, a notable anomaly arises concerning the spin population in the exit channel via the multistep DWBA transfer channel and the charge exchange channel. The investigation of individual spin populations necessitates the utilization of polarized proton beams, enabling a quantification of the specific spin population within the exit channel. Addressing this requires an array of charged particle detectors and neutron detectors designed for exclusive three-body coincidence events, along with precision pulsing of the proton beam to a definite time structure. The utilization of polarized proton beams with higher energy levels also presents a current technological challenge.

In the context of radiative captures, it is imperative to measure the radiative capture towards the distinct resonant states originating from each entrance channel's J^π states. The precise measurement of spectroscopy factors for each resonant state becomes possible through the consideration of ^{6}Li induced transfer reactions using polarized beams. To delve into the examination of the subtle branching from unbound resonant states of nuclei to the ground state, a γ calorimetry setup is essential. This setup should have the capability to determine both the total γ energy radiated per event and the γ multiplicity.

Measuring the Direct Capture across all isotopes requires comprehensive assessments in both direct neutron time-of-flight modes and indirect modes. Special attention must be given to residues that overlap with the breakup modes. This entails conducting exclusive coincidence measurements involving breakup fragments and the emitted γ particles. These measurements are crucial for gaining enhanced insights into the nature of spin transfer interactions. Additionally, elastic scattering experiments involving combinations of projectiles and targets, as well as ejectiles and residues, are necessary to achieve a deeper grasp of the underlying driving potentials. These investigations aid in deducing effective potentials resulting from the complex interplay of multiple channels. However, the

current challenges stem from limited target availability and the absence of light radioactive beams, which hinder the execution of these endeavors.

Chapter 6

Recommendations

Recent studies related to the topic of this thesis have unveiled a substantial influence of breakup coupling on the systematic behavior of nuclear reactions. These influences are prominently manifested in both the spectrum of ejectile particles and the excitation functions. Remarkably, these effects have been successfully replicated through CDCC-CRC calculations, signifying a departure from the inadequacies of statistical models in explaining such behavior. Consequently, it is strongly recommended to employ CDCC-CRC as the preferred approach for the comprehensive analysis and assessment of reactions involving weakly bound nuclei.

In the context of neutron-induced reactions, particularly those stemming from Li(p,n) sources, there is a critical issue that arises when neutron energies surpass the 5 MeV threshold. At these energy levels, the influence of the breakup neutron continuum becomes highly significant. Therefore, it becomes imperative to address this challenge by either implementing the spectral indexing method or adopting integral benchmarking techniques to rectify the neutron tails in order to ensure accurate and reliable evaluations.

The ^{7}Li(p,n) reaction serves as an exemplary case of strong breakup coupling within nuclear astrophysics, a phenomenon that significantly impacts the formation of ^{7}Be in the intense stellar environments. In the quest to accurately predict the abundances of ^{7}Be in these astrophysical scenarios, it becomes imperative to

not only characterize the cross sections associated with this reaction but also to derive the corresponding astrophysical reaction rates. These cross sections hold a pivotal role in our understanding of the nucleosynthesis processes occurring in stars.

One must also consider the n+^{7}Be interaction, which leads to an inelastic breakup of the ^{7}Be nucleus. Incorporating this interaction is crucial when attempting to account for the destruction mechanisms affecting ^{7}Be in stellar environments. This inclusion is especially pertinent in addressing the enigmatic problem of stellar neutrino missing, which has long perplexed astrophysicists.

To tackle this predicament effectively, it is essential to recognize the ^{7}Li(p,n)^{7}Be reaction as a key contributor, giving rise to the $n + ^3\mathrm{He} + \alpha$ channel. Furthermore, the n+^{7}Be interaction resulting in $n + ^3\mathrm{He} + \alpha$ reactions must be taken into account as well. Both of these channels play pivotal roles in elucidating the mechanisms behind ^{7}Be destruction. Moreover, the $^7\mathrm{Be}(p, \gamma)$ reaction remains another significant aspect of the puzzle, further emphasizing the intricate interplay between nuclear reactions in the stellar environment. By incorporating these reactions and their associated cross sections, we can gain a more comprehensive understanding of the complex processes governing the abundance and destruction of ^{7}Be in stars, ultimately shedding light on the longstanding mystery of stellar neutrino missing.

The ^{6}Li/^{7}Li abundance ratio serves as a robust tool for estimating a star's age, although it remains underutilized primarily due to practical constraints. Nonetheless, it's crucial to acknowledge that the neutron capture processes affecting both ^{6}Li and ^{7}Li can exert substantial influences on their respective abundances. These alterations introduce a significant bias, potentially leading to inaccurate age estimations.

To rectify this bias and ensure more precise age determinations, we must incorporate excitation functions pertaining to the ^{6}Li(n,γ) and ^{7}Li(n,γ) reactions. Additionally, a comprehensive analysis necessitates the consideration of the resonant breakup modes observed in ^{6}Li+n interactions and the influence

of $\beta-$delayed breakups in ^{8}Li. These components should be integrated with the excitation functions when striving to estimate solutions to the cosmological $Li - Be - B$ problem. This problem is a multifaceted challenge encompassing both the context of the Big Bang and various stellar environments.

In the operation of fast reactors and Generation IV reactors, the roles played by isotopes such as ^{6}Li and ^{7}Li are critical, particularly in emergency shutdown procedures. Additionally, these isotopes are instrumental in tritium production, which is essential for fueling fusion reactors. Specifically, the $^6\mathrm{Li}(n, \alpha)$ and $7\mathrm{Li}(n, n'\alpha)$ reactions are key to breeding tritium in the context of fusion reactors.

However, it's important to note that these reactions present significant challenges in terms of uncertainty and precision, primarily stemming from the $^6\mathrm{Li}(n, \gamma)$ and $^7\mathrm{Li}(n, \gamma)$ reactions. This uncertainty arises due to limited data availability and a lack of clarity in the underlying reaction mechanisms. Consequently, addressing these reactions involving weakly bound nuclei or shell-closed nuclei necessitates the application of direct capture approaches.

To tackle these complexities, researchers often employ direct capture methods in conjunction with breakup couplings generated through the use of the Continuum Discretized Coupled Channels (CDCC) framework. These coupled with Coupled Reaction Channels (CRC) states help to refine our understanding of the nuclear reactions involved. In essence, a comprehensive approach that combines direct capture techniques and breakup couplings within the CDCC and CRC frameworks is crucial for accurately modeling and predicting the behavior of these critical reactions in fast and Generation IV reactors, as well as in the context of tritium production for fusion reactors.

Appendix

APPENDIX

Impact of ^{7}Be breakup on the ^{7}Li(p, n) neutron spectrum

C. V. Midhun,[1] M. M. Musthafa,[1,*] S. V. Suryanarayana,[2] T. Santhosh,[2] A. Baishya,[2] P. N. Patil,[3] A. Pal,[2] P. C. Rout,[2] S. Santra,[2] R. Kujur,[2] Antony Joseph,[1] Shaima A.,[1] Hajara. K.,[1] P. T. M. Shan,[1] Satheesh B.,[4] Y. Sawant,[2] B. V. John,[2] E. T. Mirgule,[2] K. C. Jagadeesan,[5] and S. Ganesan[6]

[1]*Department of Physics, University of Calicut, Calicut University, P.O Kerala 673635, India*
[2]*Nuclear Physics Division, Bhabha Atomic Research Centre, Mumbai 400085, India*
[3]*Department of Physics, Karnatak University, Dharwad, Karnataka 580003, India*
[4]*Department of Physics, Mahatma Gandhi Government Arts College, Mahe 673311, India*
[5]*Radiopharmaceuticals Division, Bhabha Atomic Research Centre, Mumbai 400085, India*
[6]*Formarly Raja Ramanna Fellow, Bhabha Atomic Research Centre, Mumbai 400085, India*

(Received 19 July 2021; revised 27 September 2021; accepted 28 October 2021; published 16 November 2021)

The formation of continuum neutron distribution in ^{7}Li(p, n) has been identified as due to the coupling of the ^{7}Be breakup levels to the final state of the reaction. The continuum neutron spectra produced by the ^{7}Li(p, n) reaction has been estimated by measuring the double differential cross sections for continuum and resonant breakup of ^{7}Be, through the ^{7}Li(p, n)^{7}Be* reaction at 21 MeV of proton energy. The breakup contributions from continuum and $5/2^-$, $7/2^-$ states of ^{7}Be have been identified. The measured double differential cross sections have been reproduced through continuum-discretized coupled channel-coupled reaction channel calculations. The cross sections were projected to neutron spectrum using the Monte Carlo approach and validated using experimentally measured ^{3}He gated neutron spectra. ^{7}Li(p, n) neutron spectrum at 20 MeV incident proton energy measured by McNaughton *et al.* [Nucl. Instrum. Methods **130**, 555 (1975)] has been reproduced by adapting estimated model parameters for the reaction.

DOI: 10.1103/PhysRevC.104.054606

I. INTRODUCTION

Neutron induced reaction data, above 10 MeV, are having a renewed interest due to the nuclear data requirements for the design and safe operation of fusion reactors and accelerator driven systems (ADS) [1]. Activation analysis, using quasi-monoenergetic neutrons, is generally utilized for measuring cross sections for such studies. The ^{7}Li(p, n) channel is a promising source of such neutrons due to the quasi-monoenergetic behavior linearly up to 5 MeV. Further, the energy tunability and higher yield of this channel makes the ^{7}Li(p, n) the most used accelerator based neutron source for nuclear astrophysics and nuclear data measurements [2–4]. ^{7}Li(p, n) is also gaining attention as a compact accelerator neutron source (CANS) [3,5] in the fields of technology and medicine [6,7].

As the proton energy increases above 3.22 MeV, [1.64 MeV threshold for ^{7}Li(p, n) and 1.58 MeV breakup threshold for ^{7}Be to ^{3}He and α] the neutron distribution behaves as a continuum from 0 to ($E_p - 3.22$ MeV), including the monoenergetic peaks corresponding to the population of ground and $1/2^-$ states. However, there are several measurements with ^{7}Li(p, n) neutrons, at proton energies above 15 MeV, for exploring the reactions having threshold greater than ($E_p - 5$ MeV). This practice has been continued with the assumption that the neutrons contained in ($E_p - 5$ MeV) to ($E_p - 3.2$ MeV) range is less than 1% of neutrons enclosed by n_0 and n_1 neutron colonies (corresponding to ground and $1/2^-$ states of ^{7}Be, respectively). In some recent works, the extra contribution from the neutron continuum is being accounted for by the tailing correction methods [8,9].

So far there exist only a few measurements of the ^{7}Li(p, n) neutron spectrum above 5 MeV, the domain which the neutron continuum distribution is being prominently contributing to the neutron spectrum. These measurements were performed by McNaughton *et al.* [10] and Majerle *et al.* [11], with a thick ^{nat}Li target in the neutron time of flight mode, using the pulsed protons from cyclotron. There are some important works by Mashnik *et al.* [12], Meadows and Smith [13], and Drosg *et al.* [14], to theoretically model the neutron spectrum from the ^{7}Li(p, n) reaction, by taking neutron spectrum measured by McNaughton *et al.* as a reference. However, due to the lack of enough experimental data on ^{7}Li(p, n)^{7}Be$^* \rightarrow n + {}^3$He $+\alpha$, the neutron spectrum is not well reproduced by these attempts.

In the perspective of theoretical modeling, the neutron continuum distribution in the ^{7}Li(p, n) neutron spectrum, above the three-body breakup threshold, is considered to have emerged because of the coupling of continuum levels of ^{7}Be to the outgoing neutron wave function. These continuum levels are being considered as originated by the relative motion of α-^{3}He internal structures of ^{7}Be above the breakup threshold of 1.58 MeV. Moreover, other than continuum states, the $5/2^-$, $7/2^-$ resonant states of ^{7}Be also contribute to the breakup. This makes the additional peak structures to the

*mmm@uoc.ac.in

 ©2021 American Physical Society

NUCLEAR SCIENCE AND ENGINEERING
© 2019 American Nuclear Society
DOI: https://doi.org/10.1080/00295639.2019.1681210

Spectroscopy of High-Intensity Bremsstrahlung Using Compton Recoiled Electrons

C. V. Midhun,[a] M. M. Musthafa,[a]* Shaima Akbar,[a] Swapna Lilly Cyriac,[b] S. Sajeev,[b] Antony Joseph,[a] K. C. Jagadeesan,[c] S. V Suryanarayana,[d] and S. Ganesan[e]

[a]*University of Calicut, Department of Physics, Malappuram, Kerala, India*
[b]*Kerala Institute of Medical Sciences, Cancer Care and Research Center, Department of Radiation Oncology, Thiruvanandapuram, Kerala, India*
[c]*Bhabha Atomic Research Centre, Radiopharmaceuticals Division, Mumbai, India*
[d]*Bhabha Atomic Research Centre, Nuclear Physics Division, Mumbai, India*
[e]*Bhabha Atomic Research Centre, Raja Ramanna Fellow, Department of Atomic Energy, Mumbai, India*

Received September 20, 2019
Accepted for Publication October 12, 2019

Abstract — *Recoiled Compton electrons of 180 deg have been utilized to measure the energy distribution of high-intensity bremsstrahlung. An optimized detector-collimator configuration was used for detection and spectrum measurement of recoiled electrons. The spectrum has been reconstructed using Compton cross sections retrieved from the ENDF/B.VIII.0 library. The measured spectrum has been further validated using theoretical simulation by the Geant4 code with incorporating ENDF/B-VIII.0–recommended cross sections. The simulated spectrum matches the measured spectrum if the spatial spread and energy spread of the electron beam are accounted for in the simulations.*

Keywords — *Bremsstrahlung spectroscopy, Compton scattering, Geant4, nuclear instrumentation.*

Note — *Some figures may be in color only in the electronic version.*

I. INTRODUCTION

For use in radiation therapy, medical linear accelerators typically accelerate electrons to medium energies, up to 20 MeV. Interestingly, such medical accelerators can also be utilized for small-scale research using photon- and neutron-induced reactions in nuclear and radiation physics subjects. In medical accelerators, the photon beams are produced in thick target bremsstrahlung mode by the accelerated electron beam falling on a built-in high-atomic-numbered target. The availability of this feature is limited to a few of the preconfigured photon energies. Further, other bremsstrahlung energies can be generated with available electron energies by introducing an external target at the end of an electron applicator.[a]

Performing research experiments with photons of interest in nuclear physics requires a precise knowledge of the produced bremsstrahlung spectrum. But, the critical components in the beam path, such as the primary collimator, flattening filter, jaws, multileaf collimator, etc., will modify the bremsstrahlung spectrum from the inherent behavior. In most of the cases, the spectrum is generated using Monte Carlo codes to account for the perturbing effects of these components.[1–3] However, instantaneous changes of the beam current and energy spread will induce severe reverberation leading to a deviation between the final bremsstrahlung spectrum and the estimated "virgin" theoretical spectrum. It may be noted further that particularly when the bremsstrahlung spectrum is generated with an external bremsstrahlung

*E-mail: mmm@uoc.ac.in

[a] An electron applicator is a device used to guide the electron beam into the required field size and is used in medical accelerators.

arXiv:2209.12165v1 [nucl-ex] 25 Sep 2022

An Indirect Measurement of ^{6}Li(n,γ) Cross Sections

Midhun C.V[1],* M.M Musthafa[1],† S.V Suryanarayana[2,3], Gokuldas H[1], Shaima A[1], Hajara. K[1], Antony Joseph[1], T. Santhosh[2], A. Baishya[2], A Pal[2], P.C Rout[2], S Santra[2], P.T.M Shan[1], Satheesh B[4], B. V. John[2], K.C Jagadeesan[5], and S. Ganesan[6]

[1] *Dept. of Physics,University of Calicut, Calicut University P.O Kerala, 673635 India*
[2] *Nuclear Physics Division, Bhabha Atomic Research Centre, Mumbai 400085, India*
[3] *Manipal Centre for Natural Sciences, MAHE, Manipal - 576014, India*
[4] *Dept. of Physics, Mahatma Gandhi Government Arts College, Mahe, 673311, India*
[5] *Radiopharmaceuticals Division, Bhabha Atomic Research Centre, Mumbai 400085, India and*
[6] *Formarly Raja Ramanna Fellow, Bhabha Atomic Research Centre, Mumbai 400085, India*

(Dated: September 27, 2022)

The ^{6}Li(n,γ)^{7}Li cross sections in the neutron energy range of 0.6 to 4 MeV have been measured by the experimental implementation of the direct capture formalism. This was done by measuring the γ transition probability experimentally and accounting for the spin factor by theoretical calculation. The electromagnetic transition probabilities from ^{7}Li* analogous to the initial neutron capture states of ^{6}Li+n were measured by populating the J$_i$ states of ^{7}Li through ^{7}Li$(p,p')^7$Li* reaction. The impact of coupling of resonant states, above neutron separation threshold of ^{7}Li, in the neutron capture, is observed from the capture γ spectrum. The measured cross sections were reproduced through FRESCO and Talys-1.95 Direct Capture Calculations.

Neutron induced reactions on Li isotopes are having a renewed interest due to their involvement in nuclear astrophysics and Gen.IV nuclear reactors[1–3]. Though ^{6}Li(n,γ) reaction is having a significant importance, the reaction remains thus for unexplored. As the abundance ratio of ^{6}Li to ^{7}Li is used as an observable for estimating the time scale of stellar evolution, the reaction is having a major role in the Standard Big Bang Nucleosynthesis (SBBN) network calculations[1, 4, 5]. Further, ^{6}Li(n,t) and ^{6}Li(n,n$\prime$t) reaction contribute to the ^{3}H breading in fusion reactors [6]. In the emergency shut down system of fast neutron reactors, lithium enriched in ^{6}Li is used. In these cases, ^{6}Li(n,γ) reaction also will be initiated due to the high flux neutron environment and remains as the major source of uncertainty in the tritium production[7].

The abundances of ^{6}Li and ^{7}Li are highly influenced by the ^{6}Li(n,γ) reaction rates. In order to avoid the wrong estimations and biasing in the SBBN network calculations, the cross section for this channel has to be accurately measured[1, 4, 5]. However, the ^{6}Li(n,γ) reaction remains not well explored due to its small cross section as well as the lesser natural abundance of ^{6}Li. The ^{6}Li(n,γ)^{7}Li exhibits considerably small cross sections, in the order of μb, due to the predominance of $\alpha + t$ breakup mode, ^{6}Li(n,α)^{3}H channel being prominent. This breakup mode having a threshold of 2.47 MeV, dominates as the Q-value for the neutron capture of ^{6}Li is as high as 7.25 MeV. Due to this higher Q-value, breakup levels populate more than the single particle levels. This suppresses the radiative neutron capture process in ^{6}Li. However, the direct reaction component involving the single particle levels contributes significantly to the radiative neutron capture through Direct Capture (DC) mechanism [8, 9].

There is only a single measurement on energy dependant cross section of ^{6}Li(n,γ) existing in the literature, by Ohsaki et al., for the neutron energy range of 20 to 80 keV[10]. The other measurements available as exfor entries [11], by R. B Firestone et al. [12], Chang Su Park et al. [13] and G.A Batholomew et al. [14] are the Maxwellian averaged cross sections for thermal reactor neutron spectrum. Further, there are evaluations existing for ^{6}Li(n,γ) in ENDF/B-VIII.0 [15], JEEF [16] and JENDL[17] basic evaluated nuclear data libraries. They are the derived data sets estimated by fitting the R-Matrix formalism on ^{6}Li(n,t)^{4}He cross sections[15]. Due to the limitations with the ^{6}L target and lower cross sections, the direct measurement of ^{6}Li(n,γ) is potentially challenging.

As a solution to this problem, an experimental methodology has been implemented by utilizing the properties of the Direct Capture formalism. The measurement of ^{6}Li(n,γ) cross sections has been attempted through this method, by populating the initial neutron capture states by inelastic scattering of protons on ^{7}Li. The γ transitions from the ^{7}Li initial state to bound states of ^{7}Li are measured by generating $p - \gamma$ coincidences. The capture cross sections were determined through the approach of Direct Capture mechanism, reformulated for the experimental implementation. The current experiment is having resemblances with the established Oslo method[18, 19]. In this study, only a single large volume LaBr$_3$ scintillator was used instead of γ calorimeter. This measurement has been successful because all the γ events from the initial neutron capture states are well resolvable and γ multiplicity is near to unity.

The direct capture model (DC) is well established for explaining the radiative captures at lower energies, and

* midhun.chemana@gmail.com
† mmm@uoc.ac.in